Title

Investigate Materials in Solar Cells and Batteries with Synchrotron Techniques to Mitigate Degradation

Author

Quinn, Xueying Li

Publication Date

2022

Peer reviewed|Thesis/dissertation

UNIVERSITY OF CALIFORNIA SAN DIEGO

Investigate Materials in Solar Cells and Batteries with Synchrotron Techniques to Mitigate Degradation

A Dissertation submitted in partial satisfaction of the requirements
for the degree Doctor of Philosophy

in

Materials Science and Engineering

by

Xueying Li Quinn

Committee in charge:

Professor Shirley Meng, Chair
Professor David Fenning, Co-Chair
Professor Andrew Kummel
Professor Jian Luo
Professor Shyue Ping Ong
Professor Oleg Shpyrko

2022

The Dissertation of Xueying Li Quinn is approved, and it is acceptable in quality and form for publication on microfilm and electronically.

University of California San Diego

2022

DEDICATION

This work is dedicated to my devoted husband, Jules, who through his strong love and positivity has encouraged me to pursue my dreams.

TABLE OF CONTENTS

Contents

LIST OF FIGURES

LIST OF TABLES

ACKNOWLEDGEMENTS

I would like to thank Prof. Meng and Prof. Fenning for guiding me through my research.

Chapter 1, in full, is a reprint of the material as it appears in Residual nanoscale strain in cesium lead bromide perovskite reduces stability and shifts local luminescence in Chemistry of Materials 2019. Li, Xueying; Luo, Yangqi; Holt, Martin V.; Cai, Zhonghou; Fenning, David P. The dissertation author was the primary author of this paper.

Chapter 2, in full, is a reprint of the material as it appears in Europium Addition Reduces Local Structural Disorder and Enhances Photoluminescent Yield in Perovskite CsPbBr3 in Advanced Optical Materials 2021. Quinn, Xueying L.; Kumar Rishi E.; Kodur, Moses; Cakan, Deniz N.; Holt, Martin V.; Cai, Zhonghou; Zhou, Tao; Fenning, David P. The dissertation author was the primary author of this paper.

Chapter 3, in part is currently being prepared for submission for publication of the material. Quinn, Xueying; Yin, Lu; Li, Weikang; Li, Mingqian; Wicker, Connor; Liu, Ruixiao; Dang, Bryant; Ortega, Jeff; Wang, Joseph; Meng, Ying Shirley. The dissertation author was the primary researcher and author of this material.

VITA

2015 Bachelor of Arts in Chemistry, Cornell University

2018 Master of Science in Materials Science and Engineering, University of California San Diego

2022 Doctor of Philosophy in Materials Science and Engineering, University of California San Diego

PUBLICATIONS

(1) Quinn, X. L.; Yin, L.; Li, W.; Li, M.; Wicker, C.; Liu, R.; Dang, B.; Ortega, J.; Wang, J.; and Meng, Y. S. Investigate Silver Dissolution in Primary and Secondary AgO-Zn Batteries. In preparation.

(2) Scharf, J., Yin, L., Redquest, C., Liu, R., Quinn, X. L., Ortega, J., Wei, X., Wang, J., Doux, J.-M., Meng, Y. S., Investigating Degradation Modes in Zn-AgO Aqueous Batteries with In Situ X-Ray Micro Computed Tomography. Adv. Energy Mater. 2021, 11, 2101327.

(3) Quinn, X. L.; Kumar, R.; Kudor, M.; Cakan, D. K.; Cai, Z.; Zhou, T.; Holt, M.; Fenning, D. P. Europium Addition Reduces Local Structural Disorder and Enhances Photoluminescent Yield in Perovskite CsPbBr3. Adv. Opt. Mater., 2002221.

(4) Rigter, S. A.; Quinn, X. L.; Kumar, R.; Fenning, D. P.; Massonnet, P.; Ellis, S. R.; Heeren, R.; Svane, K. L.; Walsh, A.; Garnett, E. C. Passivation Properties and Formation Mechanism of Amorphous Halide Perovskite Thin Films. Adv. Funct. Mater. 2021, 31, 2010330.

(5) Li, X.; Luo, Y.; Holt, M.; Cai, Z.; Fenning, D. P. Residual Nanoscale Strain in Cesium Lead Bromide Reduces Stability and Shifts Local Luminescence. Chem. Mater., 2019, 31 (8), pp 2778–2785

(6) Correa-Baena, J.-P.; Luo, Y.; Brenner, T. M.; Snaider, J.; Sun, S.; Li, X.; et al. Homogenized Halides and Alkali Cation Segregation in Alloyed Organic-Inorganic Perovskites. Science (80-.). 2019, 363 (6427), 627 LP-631.

(7) Li, X.; Luo, Y.; Holt, M. V.; Cai, Z.; and Fenning, D. P. Nanoscale Variations in Halide Perovskite Structure and Stability: Insights Via Nano-Diffraction. 2018 IEEE 7th World Conference on Photovoltaic Energy Conversion (WCPEC)), Waikoloa Village, HI, 2018, pp. 2547-2548.

ABSTRACT OF THE DISSERTATION

Investigate Materials in Solar Cells and Batteries with Synchrotron Techniques to Mitigate Degradation

by

Xueying Li Quinn

Doctor of Philosophy in Materials Science and Engineering

University of California San Diego, 2022

Professor Shirley Meng, Chair
Professor David Fenning, Co-Chair

For energy conversion and storage devices, intrinsic properties of materials determine the devices performances. Here I present works on understanding residual strain and its effect in halide perovskite materials with nanoXRD. In addition, I investigate the silver dissolution phenomenon in Zn-AgO batteries, which is a limiting factor for their shelf life and cycle life. The degradation modes of materials were studied with synchrotron X-ray techniques to provide insights for improving device performances.

CHAPTER 1

INTRODUCTION

The manipulation and control of strain during crystal growth is foundational for advanced optoelectronic materials and heterostructures. The effect of strain on band gap and mobility has been intensely studied and exploited in Si, Ge, and III-Vs,[1–3] while strain engineering is a key enabler of complex oxide perovskite heterostructures.[4,5] In contrast, understanding of strain and control of it during growth of the emergent halide perovskites is still limited. With long carrier diffusion lengths and a tunable band gap as a function of composition,[6,7] the halide perovskites have shown promise for diverse optoelectronic applications including solar cells,[8] light emitting dioides,[9] lasing,[10] and photodetectors.[11] Despite their facile processing and significant strides in optimization of optoelectronic properties, halide perovskites still suffer from poor durability with respect to traditional semiconductors – the major barrier to their commercial application.

Strain arises from the annealing typical in synthesis of halide perovskite thin film[12] and nanoparticles.[13] The commonly-used spin casting and annealing method is a fast crystallization process, which impacts the carrier lifetime and mobility of the perovskite layer.[14] Controlling the fabrication process to improve the crystal quality has been found to effectively improve the perovskite-based device performance. A number of studies have recently shown reduced XRD peak full-width half maximum by varying the substrate,[15,16] halide intermediates[17] and metal doping[18] to give better perovskite solar cell performance. In the recent study of $CH_3NH_3PbI_3$ thin films by Zhao *et al.*, strain created by the thermal mismatch with the substrate during crystallization annealing after spin-casting was found to be detrimental to device stability.[12] Avoiding thermal annealing by using solvent exchange to crystallize the perovskite has been

shown to reduce strain and improve perovskite stability.[19] These recent studies shed new light on the important role of strain and stability in halide perovskite. To better resolve the impact of strain in halide perovskite materials and devices, localization of strains in perovskite thin films is necessary to precisely attribute the effect of strain on stability.

The development of halide perovskites as high-energy photodetectors is also gaining attraction due to their high detectivity.[20–23] Specification of perovskite stability under diverse functional environments including high-energy irradiation and identification of the factors that limit stability is needed for deployment of halide perovskite across optoelectronic applications.

Beyond stability, strain may play a significant role in the optoelectronic properties of halide perovskites. First-principles density functional theory studies have proposed that hydrostatic pressure or biaxial strain can reduce the band gap in halide perovskites.[24–26] Several experimental investigations have studied the effect of hydrostatic pressure on band gap in hybrid ($APbX_3$ with $A=CH_3NH_3^+$ (MA) or $CH(NH_2)_2^+$ (FA) and $X=Br^-$ or I^-)[27–33] and inorganic cesium lead halide perovskite, $CsPbBr_3$.[34] The band gap narrows under <1 GPa hydrostatic compression due to increasing in antibonding overlap of Pb-X; on the contrary, the band gap broadens under high pressure (>1 GPa), which could be due to phase change or amorphization in the high-pressure regime.[29] Hall *et al*. also observed a blue shift of photoluminescence (PL) of $CH_3NH_3PbI_3$ in the presence of humidity, and their first-principles computation shows a simultaneous increase of lattice constant and band gap when intercalating water into the lattice,[35] suggesting that the band gap may be tunable by straining the crystal lattice. Along similar lines, researchers have recently demonstrated an increase in band gap with epitaxial growth of $CsPbBr_3$ on VO_2 nanowires, which results from compressive *in-plane* strains in the $CsPbBr_3$ during expansion of the nanowires.[36] While these studies introduce strains in extreme environments or

characterize the average bulk strain in perovskite films, detection of the strain distribution from common fabrication processes and understanding of the nanoscale effects of strain is needed to provide detailed insight for feedback on synthesis strategies and for designing new mechanically-responsive functionality in these optoelectronic materials.

Here we use Scanning X-ray Diffraction Microscopy (SXDM) to quantify the nanoscale local strain distribution in $CsPbBr_3$ thin film single crystals and relate these local strains to a detrimental effect on stability and a locally-varying PL peak position. Leveraging a out-of-plane strain gradient introduced during cooldown from crystal growth within a given crystal provides the opportunity to study nuanced effects of strain on stability and PL within the same single crystal, avoiding sample-to-sample variations including minor variations in growth or subsequent environmental conditions. We find that nanoscopic regions with higher out-of-plane compressive strains exhibit decreased stability and a redshift in PL peak position and that pronounced mosaicity can arise during growth of perovskite thin film single crystals.

Experimental

Synthesis of $CsPbBr_3$ crystals: $CsPbBr_3$ crystals are grown following a previously-reported method that forms thin film single crystals tens of microns in size[37] while imitating the common spin casting and annealing method. The inorganic precursors CsBr (powder, 99% Sigma Aldrich) and $PbBr_2$ (powder, 98% Sigma Aldrich) are used as purchased. 0.33 M 1:1 $CsBr/PbBr_2$ was dissolved in dimethylsulfoxide. The substrates are sonicated in soap water, IPA and water. The substrates are treated by oxygen plasma before deposition. Using patterned Pt strips on quartz to create a coefficient of thermal expansion (CTE) mismatch, a lateral strain gradient is formed in $CsPbBr_3$ crystals that grow from solution spanning the Pt and quartz

substrate. For the Pt-patterned quartz, 100-nm thick Pt is sputtered onto the quartz. The perovskite precursor solution is spin-cast onto the substrate at 500 rpm for 10 seconds. The substrate is immediately pressed onto the PDMS stamp facing down and annealed at 100 °C for 2 minutes, after which they are cooled on the fume hood bench. The $CsPbBr_3$ crystals under investigation fall across pre-patterned Pt strips on glass, as shown schematically in Figure 1a. The crystal thickness is about 2 μm as shown in Figure S1.

Nanoprobe X-ray Diffraction: Scanning X-ray nano-diffraction microscopy (SXDM) and X-ray fluorescence (XRF) were performed using the Hard X-ray Nanoprobe (HXN) of the Center for Nanoscale Materials (CNM) at sector 26-ID-C of the Advanced Photon Source, Argonne National Laboratory. SXDM uses a focused beam with 220 Bragg diffraction geometry and rasters the X-ray beam across the crystal with the scattering recorded on a pixel-array detector (Medipix) at every point to produce a map of the local out-of-plane strain (Figure 1). A Fresnel zone plate (Xradia Inc., 133-μm diameter gold pattern, 24-nm outer zone, 300-nm thickness) focuses the monochromatic incident X-ray beam (photon energy 9.0 keV, λ=1.378 Å) onto the sample with a ≈50-nm full-width half-maximum lateral beam cross-section in the focal plane with a photon flux of $3x10^8$ photons/sec.[38] The perovskite sample is mapped with a 1.5-μm stepsize while the pixel array detector captures the diffracted intensity at each scan position. A single-element florescence detector is used to locate the crystal over the Pt electrode edge on quartz. To image the scattered intensity from the (220) peak of the orthorhombic $CsPbBr_3$ crystal, the sample is positioned at 220 Bragg diffraction to the X-ray incident beam, and the detector is positioned at 2θ=27.44° (λ=1.3777 Å). A map of 2θ variation is obtained by calculating the centroid of 2θ in each diffraction image. The scattering intensity and position in 2θ is extracted from each image. When lattice plane rotation is present, we eliminated the

rotation error and extracted the magnitude of strain by simulating the diffraction pattern with Patterson function,[39] which separates the shift of the bright diffraction fringe from the movement of the aperture projection in the diffraction image. When there is minimal rotation (no shift of aperture center) detected, the 2θ is converted directly to *d*-spacing. The local strain in the [220] direction is calculated from the *d*-spacing, *d*', extracted from the measured 2θ diffraction at each spot relative to the (220) d-spacing, *d*°, of $CsPbBr_3$ powder produced by scraping crystals from glass slides and grinding (Figure S8), yielding lattice parameters consistent with the literature value of the room-temperature orthorhombic $CsPbBr_3$ phase (ICSD 97851), as in Eq. 1:

$$\varepsilon_{220} = \frac{d'_{220} - d^{o}_{220}}{d^{o}_{220}} \quad (1)$$

The instrument maintains angles between the X-ray beam, sample, and detector with ± 0.001° precision. In addition, the diffraction detector spans a width of 1° 2θ with a pixel resolution of 0.003°. This state-of-the-art control provided by the instrument allows us to observe the out-of-plane strain distribution precisely.

SXDM also provides an opportunity to study the stability and degradation mechanism of perovskite crystals under intense ionizing irradiation, relevant to potential applications in high-energy detection. The 6×10^{17} photons/s-cm^2 synchrotron X-ray irradiation generates energetic core holes and hot electrons that, after a cascading thermalization process, settle at the band edges of the perovskite. The X-ray dose is calculated from the flux $3\text{x}10^8$ photons/sec and beam diameter 240 nm at the (220) Bragg angle to the sample surface.[40] Each hard X-ray photon absorbed in the perovskite generates $>10^3$ band edge carriers, according to the empirical relationship $N_{carriers} = E_{X\text{-}ray}/3E_g$.[41] The radiation hardness and the relationship between strain and

degradation of the perovskite under high-flux ionizing radiation is of interest in the design of perovskite gamma-ray and X-ray detectors.

To analyze any structural degradation in time series measurements of the scattering from single points on the sample, a correlation coefficient of the diffraction pattern at each frame with respect to the initial one was calculated as a representation of structural degradation of perovskite, according to:

$$r = \frac{\sum_m \sum_n (A_{mn} - \bar{A})(B_{mn} - \bar{B})}{\sqrt{(\sum_m \sum_n (A_{mn} - \bar{A})^2)(\sum_m \sum_n (B_{mn} - \bar{B})^2)}} \quad (2)$$

in which A_{mn} is the signal count of one pixel in the 514-by-514 initial diffraction image, and B_{mn} is the signal count of the same pixel of the subsequent diffraction image. $\bar{A}$ and $\bar{B}$ are the average signal counts of the initial diffraction image and the subsequent one respectively. The time when the *r* drops below 0.9 was select for comparison (t_{90}). To assess the effect of the out-of-plane compressive strain while preserving the sample properties, each spot for time series analysis was separated from the last by 4 μm. With a beam FWHM about 50 nm, this spacing is large enough to minimize irradiation-induced damage carryover to the next time-series spot.[40]

Micro-photoluminescence: Photoluminescence mapping was performed at 50x magnification using a Renishaw inVia microscope equipped with a Si CCD array detector. A 514-nm laser source with 1.0 μW power was scanned in 1 μm steps. Luminescence was collected via a 1200 mm^{-1} grating, which with the 514-nm incident laser results in a spectral resolution about 0.1 nm. To better match the same sampling volumes between the normal-incidence PL maps and the nano-diffraction that samples the whole thickness of the 2 μm thick crystal at an oblique angle, an 8-μm horizontal averaging filter was applied to PL maps. Additional experimental details can be found in the supplemental Information.

Results and Discussion

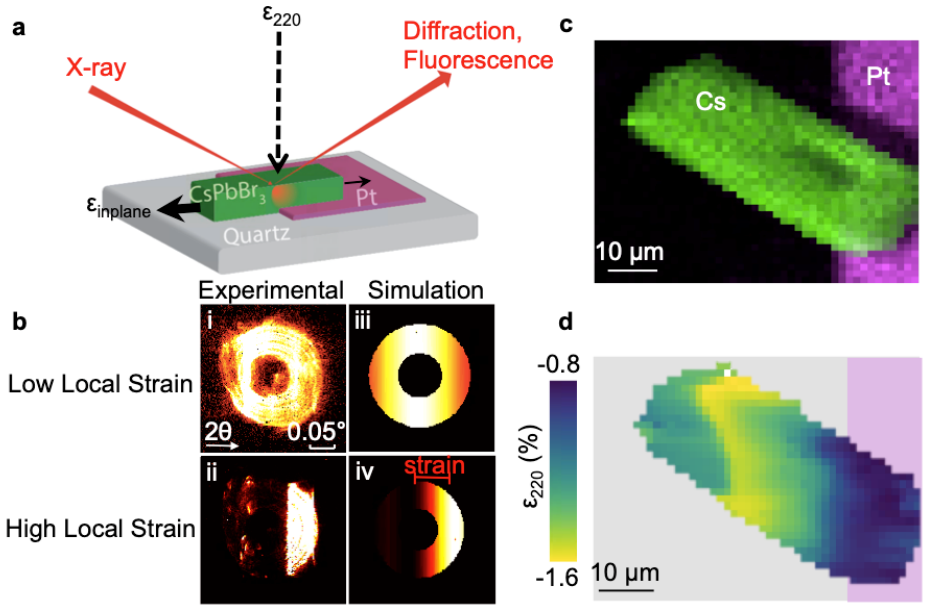

Figure 1.1. (a) Schematic of the nano-diffraction measurement of an out-of-plane strain gradient induced in a perovskite thin film single crystal by the CTE mismatch at the quartz and Pt substrate interfaces beneath it. The Scanning X-ray Diffraction Microscopy (SXDM) quantifies the out-of-plane strain component only, ε_{220}. (b) Experimental diffraction patterns of (i) low local strain and (ii) high local strain regions in crystal. Simulated diffraction patterns of (iii) low-strain and (iv) high-strain regions in crystal. The shift of the bright vertical fringe on the circular aperture is caused by strain. (c) Plan view X-ray fluorescence map of Cs (green) and Pt (purple) counts, indicating the crystal's position across the quartz/Pt edge. (d) Experimental out-of-plane strain map in a $CsPbBr_3$ crystal characterized by SXDM on quartz/Pt substrate.

Local changes in out-of-plane *d*-spacing due to the in-plane biaxial strain are obtained from each diffraction image by the relative position of the diffraction fringe on the bright ring of scattered intensity (Figure 1). The circular ring that appears in the scattering image, an example of which is shown in Figure 1b, results from the projection of the circular aperture of the Fresnel zone plate that focuses the X-ray beam. The zone plate's center beam stop creates the appearance of an annulus in the image. Local lattice strain and any rotation of the diffracting crystal planes can be systematically separated in each diffraction pattern by distinguishing changes in the position of this annulus, related to rotation, from the shift in diffracted intensity *within* the annulus, which indicates lattice strain. This approach to analysis of the scattering pattern gives a

measure of the average lattice strain within the nanoscopic probed volume, not what might be called "microstrain" in the sampling volume that would indicate lattice disorder or defects. For brevity, we thus use the term "strain" below to refer to the average out-of-plane strain (ε_{220}) that we measure in each nanoscopic volume point-by-point in SXDM, resulting from a biaxial in-plane strain developed during the synthesis on a substrate.

Figure 1b shows a diffraction image from a location on the $CsPbBr_3$ exhibiting a local low-strain position of the bright fringe (Figure 1b(i)) compared to a diffraction image where the position of the bright diffraction fringe on the circular-shaped aperture has moved to higher 2θ, indicating a larger compressive strain in the [220] direction (Figure 1b(ii)). To confirm and quantify this shift due to strain, Patterson function simulation of the diffraction pattern is used (Figure 1b(iii, iv)). The low-strain and high-strain diffraction patterns in Figure 1b(i and ii) are calculated to exhibit -1.02% and -1.59% strain respectively. This strain is separated from the movement of the whole circular aperture on the diffraction detector, which can result from the rotation of the lattice planes within the crystal. Given the negligible rotation of the crystal planes evidenced by the stationary zone plate projection in the diffraction images, the 2θ variation is almost exclusively the result of strain in the crystal.

The X-ray fluorescence (XRF) map of the $CsPbBr_3$ crystal spanning the Pt electrode and quartz substrate is shown in Figure 1c, where the Cs corresponds to the perovskite crystal and the Pt signal is from the electrode. If we assume that the growing $CsPbBr_3$ does not freely slip from the substrate interface, the contraction of $CsPbBr_3$ during cooling from crystallization is restricted by the relatively lower CTEs of the Pt and glass substrate. The $CsPbBr_3$ crystal is thus expected to exhibit residual tensile biaxial strain in-plane and a resultant compressive strain out-of-plane, as governed by its Poison's ratio (ν=0.33).[42] Since the crystal is deposited across two

distinct materials (Pt and quartz) with lower CTEs than the perovskite, the CTE difference between Pt and quartz should result in a strain gradient across the Pt edge as shown schematically in Figure 1a. Assuming *no* slip at the substrate-crystal interface, a finite element simulation of the 2-μm thick crystal shows the crystal is compressively strained overall as indicated by a negative total integrated out-of-plane displacement everywhere along the length of the crystal as shown in Figure S2a (see Table S1 for CTEs used in simulation). As a result of the difference in CTEs, the crystal is expected to be more strained on the quartz than Pt (Figure S2a). A simulated cross-section of the out-of-plane component of the strain distribution can be found in Figure S2b.

Scanning X-ray diffraction reveals that the entire crystal has a compressive out-of-plane strain, and the region above the exposed quartz substrate is more compressively strained relative to the area above the Pt, as expected from simulation. The SXDM map of strain in the $CsPbBr_3$ crystal is shown in Figure 1d, captured simultaneously with the X-ray fluorescence (XRF) map shown in Figure 1c. The spatially-resolved, out-of-plane strain measured via nano-X-ray diffraction varies between -0.8% and -1.6%, indicating that the crystal is compressively strained in the out-of-plane direction. In general agreement with the trends from simulation, the magnitude of the strain decays toward the left and right-hand edges of the crystal and is highest nearer the quartz/Pt interface. The average lateral strain gradient across the crystal generated by the two different substrates is about 0.03%/μm. In the center of the crystal, the strain varies smoothly from higher to lower compressive strain from left to right due to the CTE mismatch of the perovskite with the Pt and quartz.

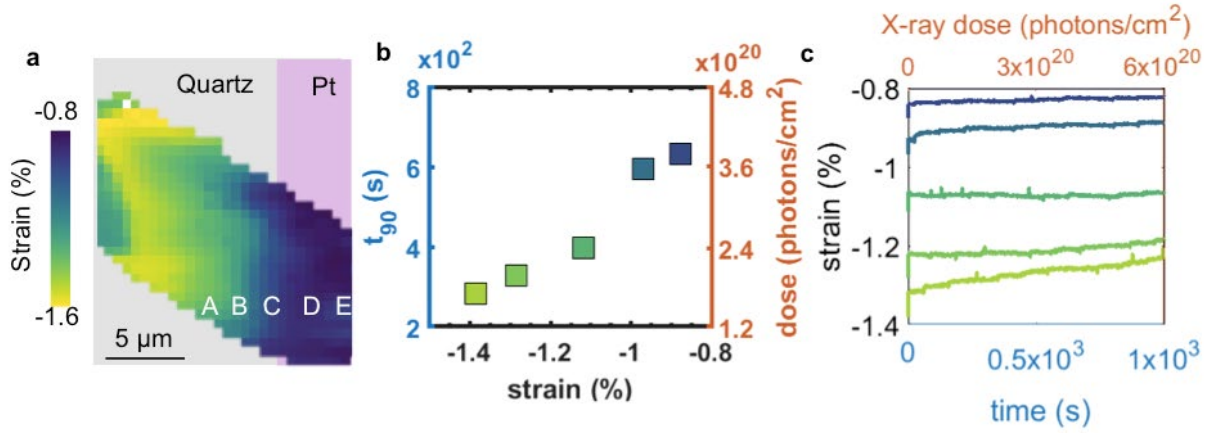

Figure1.2. (a) Five measurement locations along the strain gradient designated A- E were selected for time series analysis of the diffraction pattern. (b) The time over which the two-dimensional correlation coefficient of the diffraction pattern decays to 90% of its initial value (t_{90}) is plotted versus the local strain at locations A-E. (c) At each location A-E, the compressive strain is shown as a function of time and X-ray dose, indicating the relaxation of strain during structural degradation under X-ray irradiation.

To study the effect of strain on stability under X-ray irradiation, time series measurements were taken on different spots along the strain gradient on the crystal shown in Figure 2a and labeled positions A-E. In each time series measurement, the spot was exposed to the high-flux X-ray beam continuously to observe the change in the X-ray scattering over time. The two-dimensional correlation coefficient of the diffraction image relative to the initial image is used as an indicator of degradation. The correlation coefficient as a function of time under x-ray can be found in Figure S3a. Movies that visualize the sequence of diffraction pattern images at each spot are available in the Supplemental Information.

We find that positions with less residual strain exhibit increased structural robustness under X-ray irradiation, as indicated by a longer decay time of the scattered intensity. Figure 2b plots the relationship between strain state and t_{90}, the time when the correlation coefficient of the diffraction pattern drops below 0.9, that is when scattering image has changed more than 10%. Less-strained spots have a longer t_{90}. The degradation decay lifetime appears to vary only due to

the different strain magnitudes, as spots D and E are atop Pt and A-C are atop the quartz but they fall roughly colinearly in Figure 2b. This direct correlation between structural decay time and strain indicates that nanoscale residual strains negatively affect the stability of halide perovskites.

The reduced correlation coefficient during the time series measurement was not caused by crystal tilting or direct temperature effects. First, no crystal plane tilting was observed, which would appear as shift in the zone–plate aperture. Second, the reduction in the correlation coefficient was irreversible, as indicated by repeat measurements at the same locations, indicating the de-correlation was not due to thermal expansion under the X-ray irradiation. In some cases, we also saw that the scattering intensity increased at short times before a long-term reduction (Fig. S3b), indicating that the decay in correlation coefficient cannot be attributed to Debye-Waller effects. Overall, we attribute the reduction in correlation coefficient to the effects of irradiation itself, possibly due to either direct defect generation or carrier-induced degradation.

During the degradation process under X-ray irradiation, the compressive strain is relaxed over time, as shown in Figure 2c. This observation indicates that the generation of structural defects under intense X-ray irradiation simultaneously lowers the diffraction pattern correlation coefficient and relaxes residual strain, consistent with previous observation of strain relaxation during degradation in $CH_3NH_3PbI_3$[12]. SXDM time series studies of hybrid perovskite $CH_3NH_3PbBr_3$ crystals reveal that the hybrid perovskites undergo much more rapid structural degradation compared to $CsPbBr_3$ (Figure S4), as expected given their well-established relatively poorer stability and low enthalpy of formation.[43] The t_{90} of $CH_3NH_3PbBr_3$ corresponds to an X-ray dose of 10^{18} photon/cm^2 at 9 keV at an estimated flux of 3×10^8 photons/s, while the t_{90} of $CsPbBr_3$ corresponds to an X-ray dose of 10^{20} photon/cm^2. These dose limits provide bounds for the design of perovskite-based high energy particle detectors.

The process by which the perovskite crystal degrades is evident from the time-series diffraction patterns (Figure S4b and Supplemental Movies). The time series from $CH_3NH_3PbBr_3$ ($MAPbBr_3$) crystals reveal that the crystal structure collapses on itself locally as degradation proceeds. Upon extending the X-ray dose beyond >10x that required to collect a single high-quality scattering image, the $MAPbBr_3$ (002) *d*-spacing decreases and the angular spread in the χ-direction normal to 2θ increases. The spreading of the reflection in the χ-direction indicates that the crystal planes are bending. Together, the shrinking of the out-of-plane spacing and simultaneous warping of the (001) planes indicates a collapse of the crystal planes inward. This collapse proceeds until scattering fades completely and the local structure of the perovskite is amorphized.

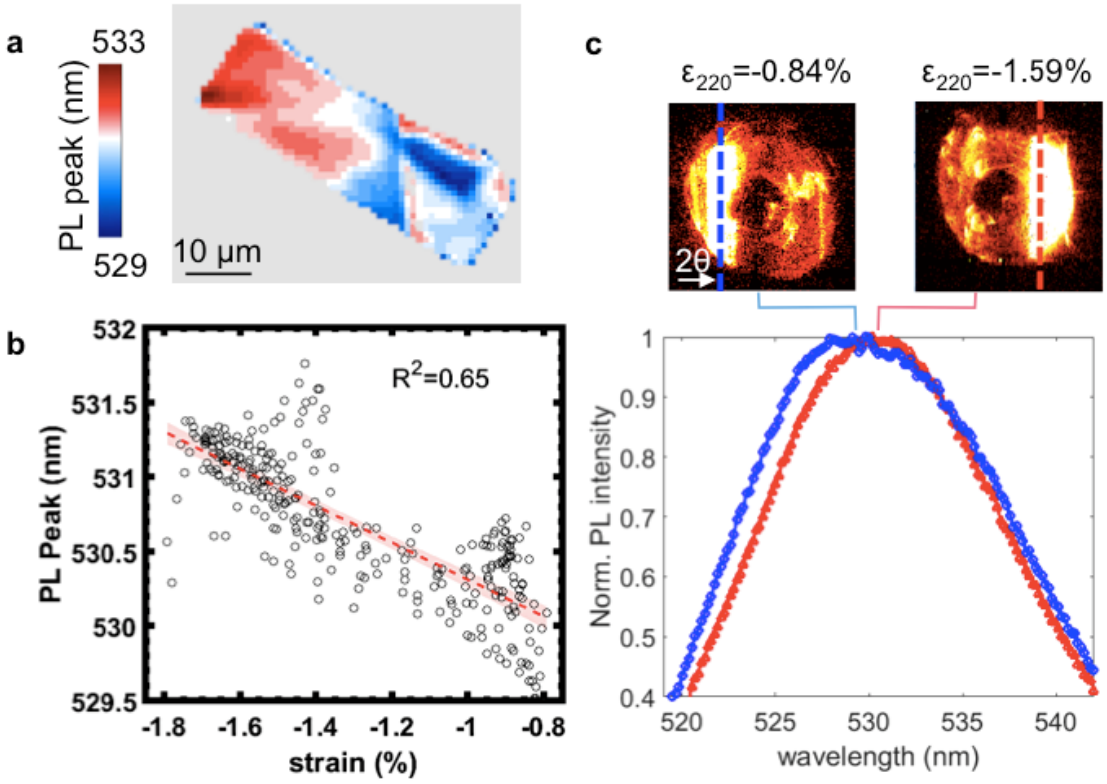

Figure 1.3. (a) Map of the wavelength of peak PL intensity for the same $CsPbBr_3$ crystal measured by SXDM and shown in Figure 1-2. (b) Negative correlation of the local PL peak versus nanoscale strain. The red line indicates the best fit line, and the shaded area is the functional prediction interval on the linear regression. (c) Examples of diffraction images (top) at spots on the crystal with strain -0.84% (blue) and -1.59% (red) and corresponding PL spectra (bottom). The diffraction peak shifts to higher 2θ at the more compressed location as denoted by the dashed line. The spot with larger compressive out-of-plane strain has a red-shifted PL peak.

Micro-photoluminescence (μ-PL) mapping of the $CsPbBr_3$ crystal measured by SXDM reveals a negative correlation between local strain and the peak wavelength of PL emission. The PL peak generally varies from longer to shorter wavelengths moving top left to bottom right along the crystal (Figure 3a), save a clear discontinuity at the Pt/glass interface and some edge effects. By comparison with the strain map from SXDM (Figure 1d), this blue shift of PL left to right across the crystal corresponds with the trend of moving from a region of higher compressive out-of-plane strain on the top left of crystal to lower compressive out-of-plane strain at the bottom right. We make this relationship explicit in the scatter plot in Figure 3b, where a

clear negative correlation is seen between the point-by-point strain and PL peak wavelength in this crystal (R^2=0.65). A single Gaussian was used to extract the PL peak at each point as shown in Figure S5. Figure 3c highlights two spots that exemplify this trend with local strains of -0.84% and -1.59% determined from SXDM, where a red shift at higher compressive strain is seen in their local PL emission. Extrapolating from the dataset, the unstrained crystal is expected to have a PL peak at 529 nm, in agreement with previously reported values.[44] The PL peak position shifts 1.2 +/-0.1 nm per 1% strain, suggesting that perovskites may provide sensitive opto-mechanical sensing.

The red shift concomitant with compressive out-of-plane strain may be due to at least two physical processes. One factor is that the strained $PbBr_6$ octahedra change the Pb-Br anti-bonding overlap and thus results in the red shift.[29] Another factor could be structural defects generated at strained regions leading to the band gap narrowing.[45] These shifts in in PL peak position are not the result of the appearance of secondary phases. The powder XRD only contains peaks from orthorhombic phase of $CsPbBr_3$ (Figure S6a), and each nanoscopic step of the beam across the crystal sample diffracts at the 2θ expected from the [220] peak of o-$CsPbBr_3$. The nano-XRF map shows the Cs:Pb ratio is uniform across the whole crystal area, which excludes the possibility of Cs:Pb stoichiometric variation (Figure S6b). Furthermore, electron backscatter diffraction (EBSD) identifies the crystal as orthorhombic $CsPbBr_3$ everywhere (Figure S7). Thus, the observed PL red shift can only be ascribed to the measured variation in local strain.

However, the correlation between PL peak and strain is weakened here because of several experimental factors. First, the PL and the nano-diffraction are most sensitive to different sampling volumes. The PL is most sensitive to the top 230 nm, the 1/*e* attenuation depth of the

incident 514 nm laser in $CsPbBr_3$,[46] whereas the full thickness 2 μm is probed in X-ray diffraction. Second, the substrate-induced strain is largest in magnitude near the substrate interfaces and relaxes through the crystal thickness in the vertical direction even in the absence of structural defects, as indicated by the simplified mechanical model simulated in Figure S2b. Third, the crystal stamping method used here to produce the thin film single crystal does not yield the structural quality of bulk single crystals. Thus, we expect the fundamental underlying relationship between in PL peak position and strain to be stronger than that reported here.

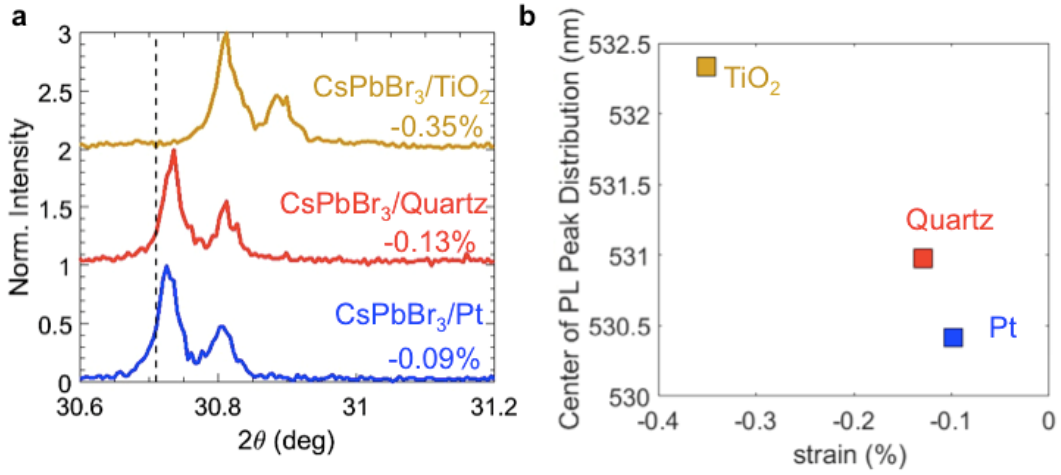

Figure 1.4. (a) Powder XRD patterns of the (220) peak of $CsPbBr_3$ crystals on Pt, quartz and TiO_2 substrates with the corresponding out-of-plain strain values. The dashed line is the literature powder XRD value of 220 peak (ICSD 97851). (b) Center of mass of the PL peak distribution in each crystal versus strain measured by benchtop XRD on Pt, quartz and TiO_2 substrates vs. measured out-of-plane strain.

Based on the clear link between PL peak and residual strain from our nanoscale characterization, we were able to reproduce the trend in benchtop XRD of films of many such microscale single crystals atop various substrates including Pt, quartz and compact TiO_2 (Figure 4). An exemplary SEM image of the crystals on the TiO_2 substrate is shown in Figure S9. With high-angular resolution benchtop XRD and careful sample height alignment, we calculate the average out-of-plane strain according to Eq. 1 for the $CsPbBr_3$ crystals on each substrate. The $CsPbBr_3$ crystals have the largest compressive strain in the out-of-plane direction on TiO_2

followed by quartz and are least strained on Pt. The full XRD patterns (Figure S8) show clearly that the crystals are the orthorhombic Pbnm phase on all three substrates. The corresponding peak wavelength of PL emission decreases as compressive strain decreases from TiO_2 to Quartz to Pt to with values of 532.3, 531.0, and 530.4 nm respectively. The higher compressive strain on quartz than Pt is consistent with the trend of their CTE mismatch with the perovskite, but the commonly-used compact TiO_2 substrate shows higher compressive strain despite having a CTE near Pt. It is possible that the wetting interaction between the perovskite and the nanoparticulate TiO_2 reduces the slip or strain relaxation at the interface between the perovskite crystals and the substrate, resulting in higher strain during crystallization. Despite benchtop thin-film XRD averaging strain many micro-crystals due to its large spot size, a small negative trend of PL peak versus strain is still evident, although the benefit of nanoscale characterization of model materials is clear in elucidating this relationship between strain and the peak wavelength of photoluminescence emission.

The local diffraction intensity does not correlate with local PL intensity, contrary to convention in the physical chemistry of semiconductors that lower crystallographic defect density corresponds to enhanced photoluminescence (Figure S10). This observation may be partially explained by the sensitivity of the PL to the unpassivated top surface while the SXDM probes through the thickness. However, it may also be an indication the self-passivating nature of defective perovskite regions.[47,48] Recent work has observed that amorphous regions at grain boundaries in $MAPbBr_3$ thin films may be passivating and display increased PL lifetime and intensity.[49] Further investigation of the relationship between perovskite crystal quality on the nanoscale and their opto(mechano)electronic properties is warranted.

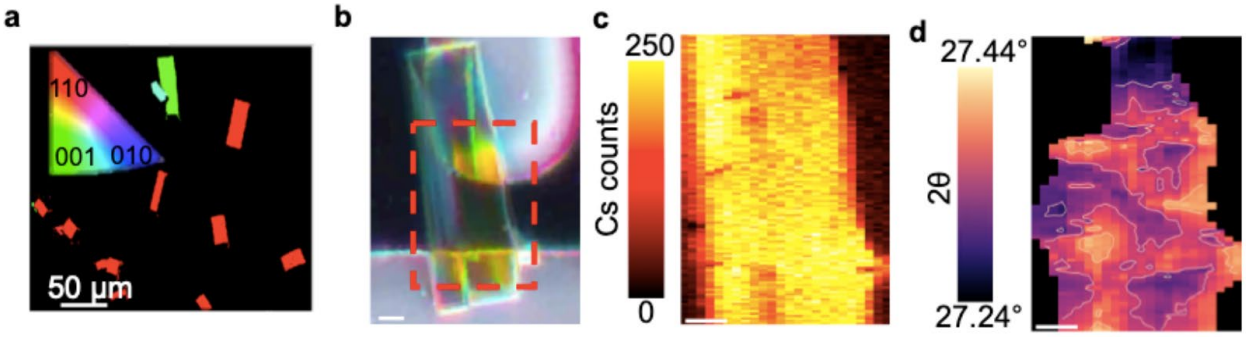

Figure 1.5. (a) As-fabricated $CsPbBr_3$ crystals appear as single-crystals with Pbnm (110) orientation in electron backscatter diffraction measurements. (b) Optical image of a $CsPbBr_3$ single crystal, where the red box indicates the region of SXDM mapping; (c) Plan view X-ray fluorescence map of Cs counts, showing the mapped crystal area. (d) The map of the centroid position of the zone plate aperture as projected onto the detector in 2θ. Scale Bar is 10 µm in (b) , (c) and (d).

Finally, we note that not all of the stamped $CsPbBr_3$ perovskite crystals exhibit a single crystalline domain upon nanoprobe investigation. Although they appear as uniform, single crystals under the more common crystallographic analysis of electron-back scatter diffraction (EBSD) (Figure 5a), the crystal in the optical image of Figure 5b showed significant mosaicity when investigated by SXDM. In Figure 5c, the Cs XRF map shows the extent of the crystal, but only some areas diffract due to mosaicity, as characterized by a map of centroid position of the aperture projection on the detector (Figure 5d). Due to the angular convergence in the focused incident beam, the annulus-shape created by the concentric zone plate and beam stop is projected by the diffracting crystal plane onto the detector within the 2θ bandwidth of diffracted intensity. Although there is no change in *d*-spacing, any crystal tilt causes a rotation of the scattering vector and thus a shift in the position of the aperture projection. Approximately, crystal plane rotation of $\Delta\gamma$ results in $2\Delta\gamma$ change of the aperture projection. This $2\Delta\gamma$ shift was calculated by monitoring the centroid of the aperture on the detector, as shown in Figure S11. The mosaics are diffracting crystalline domains within the larger crystal with slight misorientation. When the misorientation angle is small (<0.2°), the domain diffracts and displays a small shift in 2θ due to the crystal plane rotation (Figure 5d). As noted above, this rotation is straightforwardly separated

from strain in analysis of the diffraction image. In contrast, where the misorientation is large, the diffraction is not detected by the diffraction detector and appears dark in the scattering intensity map (Figure 5d). In this sample, mosaicity dominates the nanoscale structure of the film, rending detailed strain analysis impossible due to the distorted diffraction patterns (Figure S11). The formation of crystal mosaics may be due to the low formation energy of perovskite crystals and the rapid crystallization process.[50,51] Scrutinizing the crystal quality at the nanoscale, we find that mosaicity can easily result during perovskite growth. Mosaicity is also expected to reduce the stability and increase the variation in optoelectronic properties of perovskite films due to the reduction in structural quality. To our knowledge, this is the first report of mosaicity in halide perovskite crystals, though its detrimental impacts on stability have been previously hypothesized.[52] Further understanding of the heterogeneous distribution of strain and mosaic formation is necessary to understand how to reduce crystallographic imperfections in perovskite materials and requires local nanoscale characterization of crystal structure.

Conclusion

In summary, we investigate the effect of nanoscale residual strain on halide perovskite crystal structural stability and photoluminescence using synchrotron nanoprobe X-ray diffraction. Using a strain gradient that develops within $CsPbBr_3$ thin film single crystals due to the thermal expansion mismatch between the perovskite crystal and substrates, we find reduced durability at locations of higher residual strain. By using thin film single crystals, we remove any effect of grain boundaries, demonstrating the intrinsically detrimental effect of such strain on the stability of halide perovskites. Time-series analysis of structural degradation under X-ray irradiation indicates an imploding collapse of the crystal structure and provides quantitative dose limits for perovskite application in high-energy detectors. With micro-photoluminescence

mapping, we correlate the local optoelectronic properties with the measured nanoscale strain. From -0.8 to -1.6% strain, the PL peak is continuously red-shifted from 529 nm to 533 nm. The fine and continuous tuning of PL peak position with strain suggests new potential strain sensing applications for perovskites.

Because we use substrates, solution processing, and growth temperatures ubiquitous in the perovskite literature, we emphasize that re-engineering crystal growth to alleviate strain offers the opportunity to stabilize perovskite materials and devices relative to their current standard. Based on the observation that stability decreases monotonically with nanoscale strain, any localized stress concentrations that form during crystallization or in the application of perovskite films in curved or flexible devices may serve as "weakest links" for incipient degradation. Our observation of mosaicity in halide perovskite crystals at the nanoscale also indicates that crystal quality in even single crystals may affect reports of the bulk properties of halide perovskites. Improved understanding of nanoscale strain distributions formed during the synthesis of perovskite crystals should enable improved large-area crystal quality. Further work is also needed to study how nanoscale strains vary in polycrystalline thin films and across crystal chemistries in the growing family of hybrid and inorganic halide perovskite materials. Deeper understanding of how the strain is distributed at the nanoscale in perovskite materials will allow exploitation of the relationship between structural deformation and shifts in optoelectronically-active energy levels.

Acknowledgements

Chapter 1, in full, is a reprint of the material as it appears in Residual nanoscale strain in cesium lead bromide perovskite reduces stability and shifts local luminescence in Chemistry of

Materials 2019. Li, Xueying; Luo, Yangqi; Holt, Martin V.; Cai, Zhonghou; Fenning, David P. The dissertation author was the primary author of this paper.

The authors thank Joseph M. Palomba for setting up the height alignment in powder XRD measurement, Tyler Harrington and Kevin Kaufmann for EBSD measurement, and Shyue Ping Ong and Manas Holekevi Chandrappa for discussion and calculations. This research was supported by a Hellman Fellowship, UC MRPI, UC Solar and the California Energy Commission EPC-16-050. Use of the Center for Nanoscale Materials and the Advanced Photon Source, both Office of Science user facilities, was supported by the U.S. Department of Energy, Office of Science, Office of Basic Energy Sciences, under Contract No. DE-AC02-06CH11357.

APPENDICES

COMSOL simulation

The Structural Mechanics module in COMSOL was used to simulate the induced strain from cooldown during crystallization of $CsPbBr_3$. In the 2D simulation, a 2-μm thick and 30-μm wide $CsPbBr_3$ crystal sits atop a quartz slide patterned with 100-nm Pt. The crystal is positioned its midline right above the edge of the Pt. A 0.5 μm fillet was included at the corners of the crystal and the Pt edge to reduce unrealistic edge effects in the simulation. The thermal parameters of Pt and quartz from the COMSOL built-in library were used. For $CsPbBr_3$, the thermal parameters from the study by Rakita et al.[1] were used. The $CsPbBr_3$ is considered to crystallize stress free at 100°C. The temperature of the crystal and the substrate is reduced to 20°C, and the $CsPbBr_3$ crystal is compressed at the substrate interface due to its large coefficient of expansion compared with the substrates. A lateral strain gradient in the $CsPbBr_3$ crystal forms from the Pt side to the quartz side induced by the difference in coefficients of thermal expansion of the substrate materials.

Electron Backscatter Diffraction

To identify the crystal phase, electron backscatter diffraction (EBSD) is measured on the crystal using an FEI Apero scanning electron microscopy and Oxford symmetry detector at 20 kV. The crystal structures of orthorhombic $CsPbBr_3$ ICSD # 97851, tetragonal $CsPbBr_3$ ICSD # 109295 and cubic $CsPbBr_3$ ICSD # 29073 were used to match the crystal phase.

Atomic Force Microscopy

The AFM image was obtained using a Veeco Scanning Probe Microscopy in tapping mode and scanning over a range of 50 μm by 70 μm at a resolution of 360 × 512 data points.

Benchtop X-ray diffraction

Powder XRD spectra were taken by a Bruker AXS D8 Discover diffractometer in parallel beam geometry with Cu Kα radiation (λ=1.5418 Å). The height alignment accessory was used for accurate strain calculation.

Table 1.S1. Coefficients of thermal expansion of $CsPbBr_3$, Pt, quartz and TiO_2

Materials	**CTE (10^{-6} K^{-1})**
$CsPbBr_3$[1]	37.7
Pt[2]	9.0
Quartz[3]	0.55
TiO_2[4]	2.57

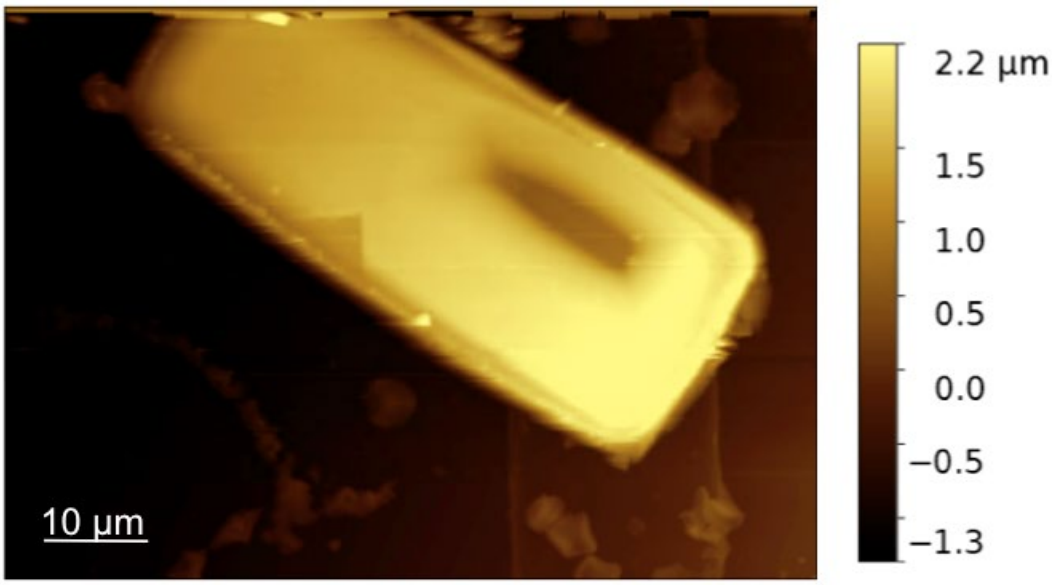

Figure 1.S1. AFM of the $CsPbBr_3$ crystal measured by nanoXRD shows the crystal is 2-µm thick with a flat smooth surface except for one large void on the right of the crystal. The roughness Ra is around 40 nm on the crystal excluding the void.

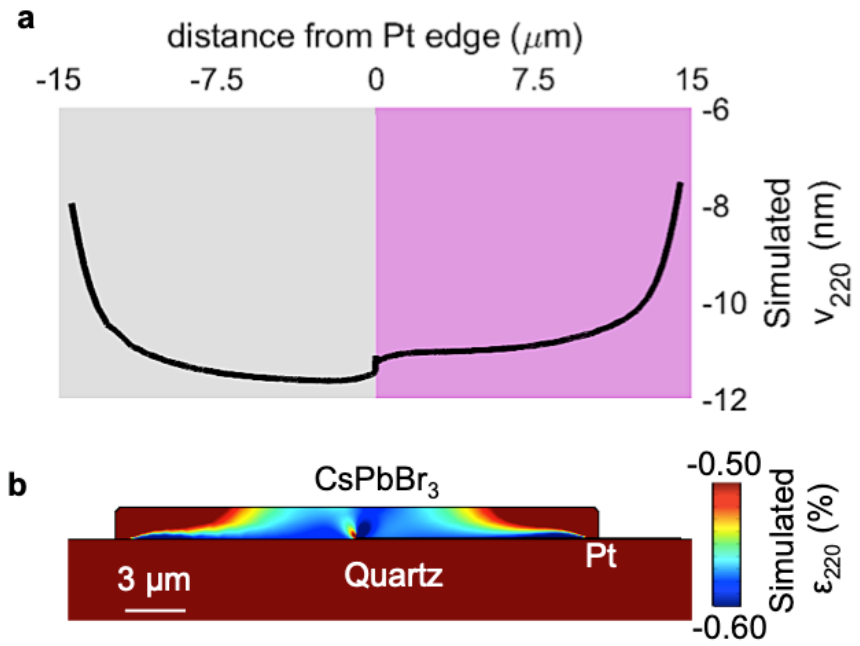

Figure 1.S2. (a) Simulated displacement of a 2-um thick $CsPbBr_3$ crystal on Pt-patterned quartz substrate. (b) COMSOL mechanical simulation of the out-of-plane strain in a the $CsPbBr_3$ crystal on Quartz/Pt substrate.

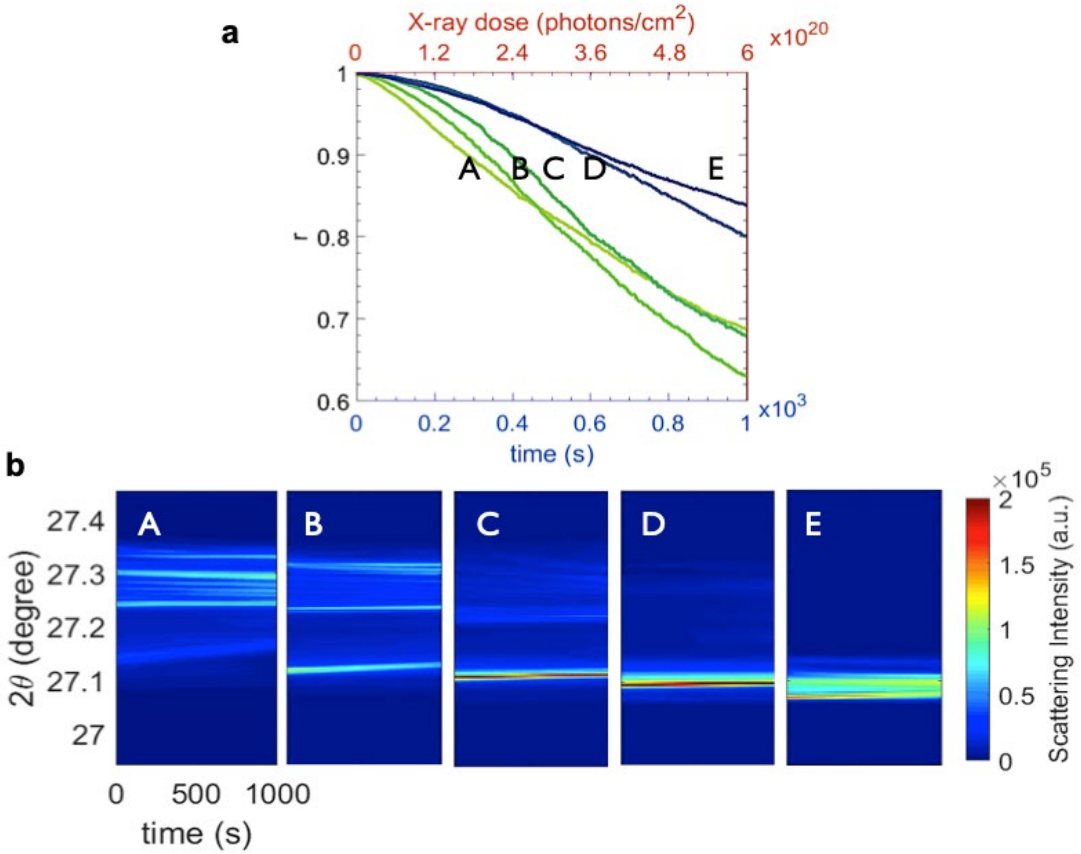

Figure 1.S3. (a) Correlation Coefficient of diffraction images as a function of time under X-ray at five positions on the strained crystal indicated in Figure 2. (b) Waterfall plot of degrading diffraction patterns at positions A, B, C, D and E indicated in Figure 2.

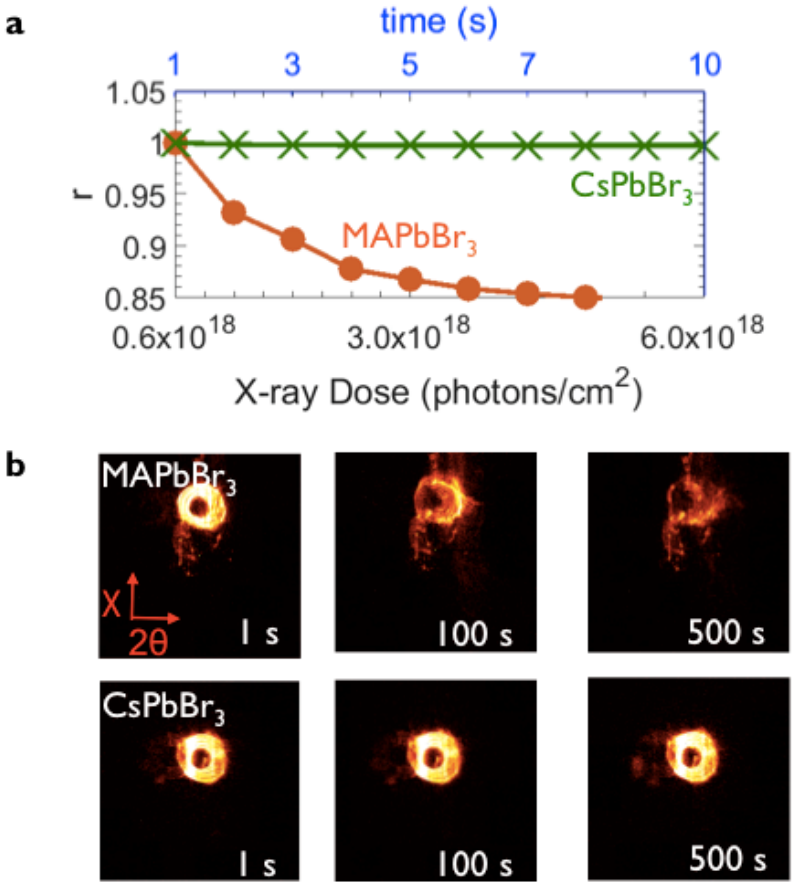

Figure 1.S4. (a) Correlation coefficient r of the diffraction image vs. accumulated X-ray dose shows that $CsPbBr_3$ (green curve) are much more stable than $MAPbBr_3$ (red curve). (b) Diffraction images of $MAPbBr_3$ and $CsPbBr_3$ diffraction at 1, 100 500s showing the relatively stable $CsPbBr_3$ under X-ray irradiation and the loss of long range order in the hybrid perovskite.

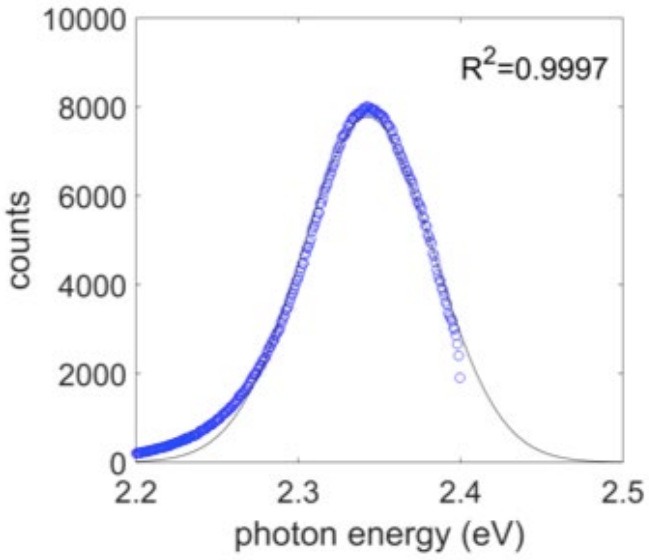

Figure 1.S5. Example of single Gaussian fit of PL spectrum of $CsPbBr_3$ from μ-PL.

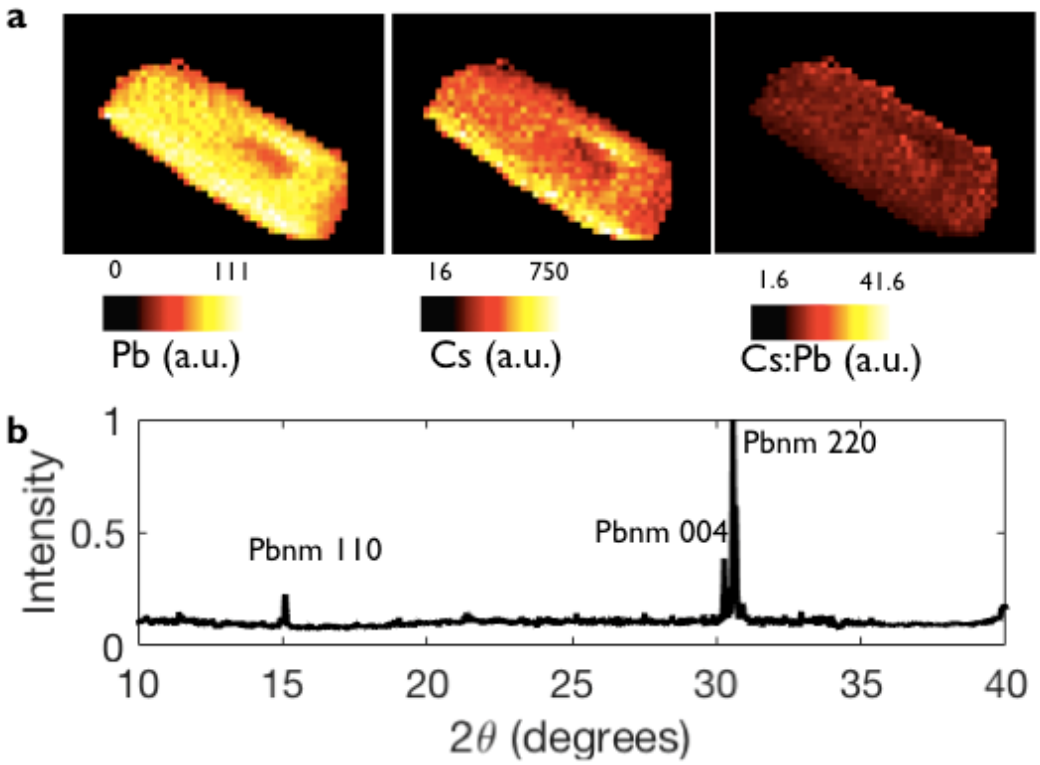

Figure 1.S6. (a) Pb, Cs, Cs/Pb ratio maps in XRF. (b) Powder XRD of the $CsPbBr_3$ sample measured by nanoXRD.

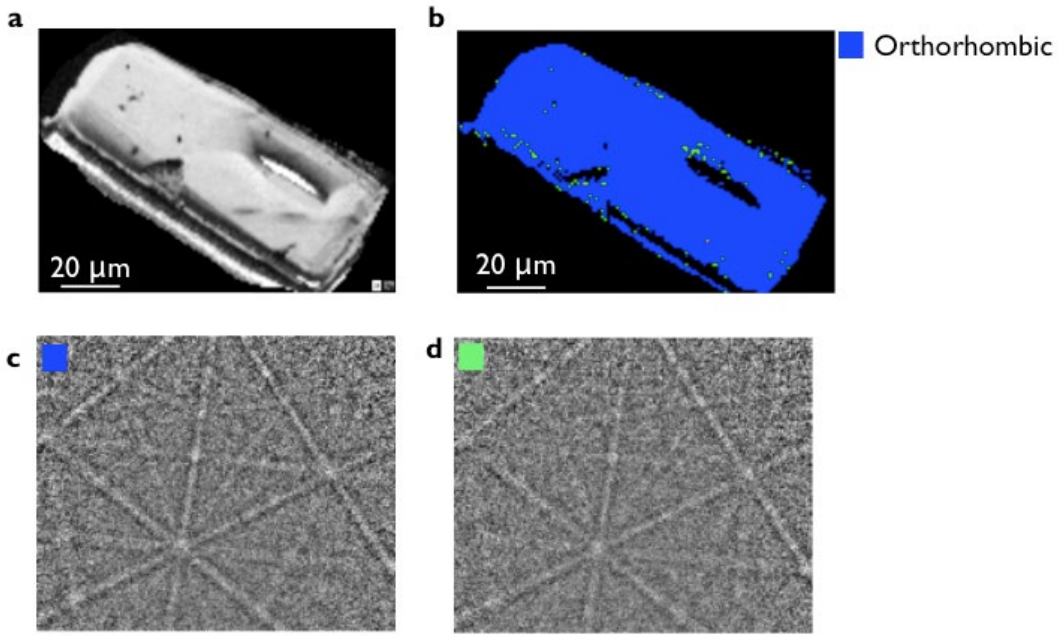

Figure 1.S7. (a) SEM image of the $CsPbBr_3$ crystal measured after nanoXRD. (b) EBSD phase map of the $CsPbBr_3$ crystal shows the crystal is orthorhomic $CsPbBr_3$ with space group Pbnm. The green dots are not automatically identified as orthorhombic phase in the software, due to poorly indexed orthorhombic patterns, as shown by (c) the Kikuchi pattern of a blue point identified as orthorhombic $CsPbBr_3$ and (d) the Kikuchi pattern of a poorly-indexed (green) point identified mistakenly as cubic $CsPbBr_3$. The symmetry and pattern in (d) precisely matches that of (c).

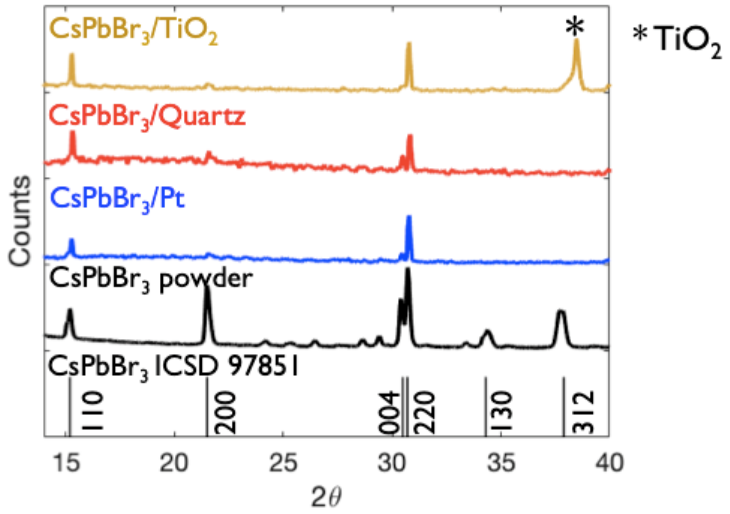

Figure 1.S8. Powder XRD patterns of crystals on TiO2, Quartz, Pt, scraped powder from drop casted crystals on glass slides and major peaks of $CsPbBr_3$ in ICSD 97851.

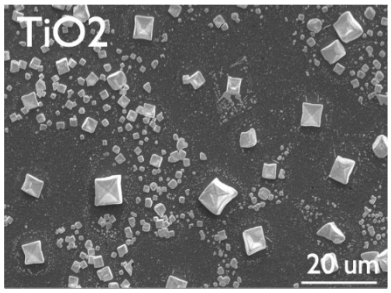

Figure 1.S9. SEM image of $CsPbBr_3$ crystal stamped on TiO_2.

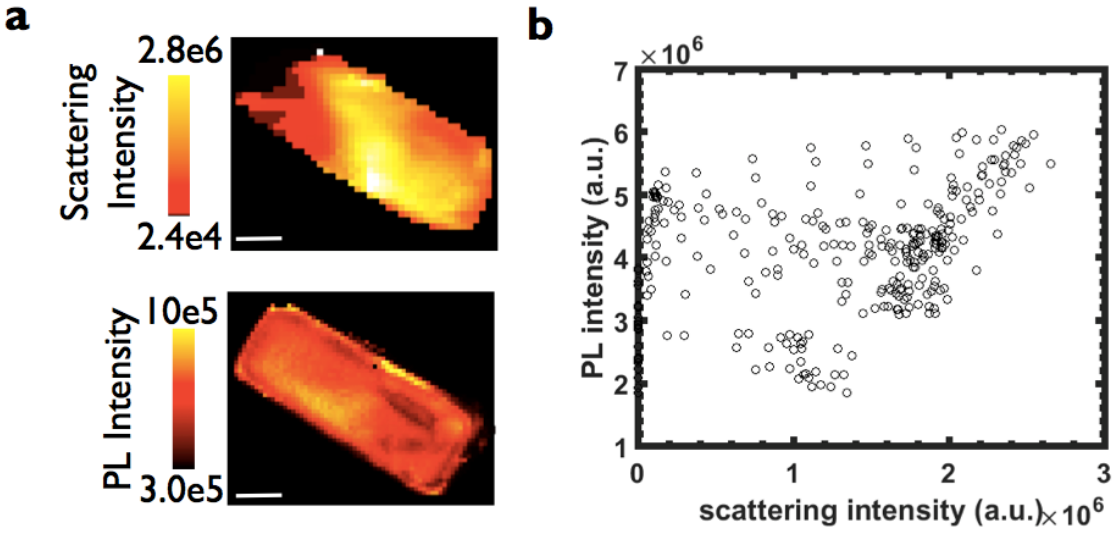

Figure 1.S10. (a) Scattering intensity map from nanoXRD and PL intensity map from microPL on the same $CsPbBr_3$ crystal. (b) Scatter plot of PL intensity versus scattering intensity shows non-association. Scale bar is 10 μm in (a).

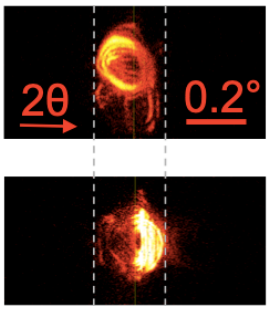

Figure 1.S11. Diffraction patterns of two different spots on the mosaic $CsPbBr_3$ crystal in Figure 5. Gray lines are for eye guidance.

REFERENCES

(1) Lee, M. L.; Fitzgerald, E. A.; Bulsara, M. T.; Currie, M. T.; Lochtefeld, A. Strained Si, SiGe, and Ge Channels for High-Mobility Metal-Oxide-Semiconductor Field-Effect Transistors. *J. Appl. Phys.* **2005**, *97* (1), 011101.

(2) DUNSTAN, D. J. Strain and Strain Relaxation in Semiconductors. *J. Mater. Sci. Mater. Electron.* **1997**, *8* (6), 337–375.

(3) Sun, Y.; Thompson, S. E.; Nishida, T. Physics of Strain Effects in Semiconductors and Metal-Oxide-Semiconductor Field-Effect Transistors. *Cit. J. Appl. Phys.* **2007**, *101*, 104503.

(4) Zubko, P.; Gariglio, S.; Gabay, M.; Ghosez, P.; Triscone, J.-M. Interface Physics in Complex Oxide Heterostructures. *Annu. Rev. Condens. Matter Phys.* **2011**, *2* (1), 141–165.

(5) Lee, M. K.; Nath, T. K.; Eom, C. B.; Smoak, M. C.; Tsui, F. Strain Modification of Epitaxial Perovskite Oxide Thin Films Using Structural Transitions of Ferroelectric BaTiO3 Substrate. *Appl. Phys. Lett.* **2000**, *77* (22), 3547.

(6) Stranks, S. D.; Eperon, G. E.; Grancini, G.; Menelaou, C.; Alcocer, M. J. P.; Leijtens, T.; Herz, L. M.; Petrozza, A.; Snaith, H. J. Electron-Hole Diffusion Lengths Exceeding 1 Micrometer in an Organometal Trihalide Perovskite Absorber. *Science (80-.).* **2013**, *342* (6156), 341–344.

(7) Liu, Y.; Ren, X.; Zhang, J.; Yang, Z.; Yang, D.; Yu, F.; Sun, J.; Zhao, C.; Yao, Z.; Wang, B.; et al. 120 Mm Single-Crystalline Perovskite and Wafers: Towards Viable Applications. *Sci. China Chem.* **2017**, *60* (10), 1367–1376.

(8) Saliba, M.; Matsui, T.; Domanski, K.; Seo, J.-Y.; Ummadisingu, A.; Zakeeruddin, S. M.; Correa-Baena, J.-P. J.-P.; Tress, W. R.; Abate, A.; Hagfeldt, A.; et al. Incorporation of Rubidium Cations into Perovskite Solar Cells Improves Photovoltaic Performance (2016 Science). *Science (80-.).* **2016**, *354* (6309), 206–209.

(9) Tan, Z.-K.; Moghaddam, R. S.; Lai, M. L.; Docampo, P.; Higler, R.; Deschler, F.; Price, M.; Sadhanala, A.; Pazos, L. M.; Credgington, D.; et al. Bright Light-Emitting Diodes Based on Organometal Halide Perovskite. *Nat. Nanotechnol.* **2014**, *9* (9), 687–692.

(10) Xing, G.; Mathews, N.; Lim, S. S.; Yantara, N.; Liu, X.; Sabba, D.; Grätzel, M.; Mhaisalkar, S.; Sum, T. C. Low-Temperature Solution-Processed Wavelength-Tunable Perovskites for Lasing. *Nat. Mater.* **2014**, *13* (5), 476–480.

(11) Song, J.; Xu, L.; Li, J.; Xue, J.; Dong, Y.; Li, X.; Zeng, H. Monolayer and Few-Layer All-Inorganic Perovskites as a New Family of Two-Dimensional Semiconductors for Printable Optoelectronic Devices. *Adv. Mater.* **2016**, 4861–4869.

(12) Zhao, J.; Deng, Y.; Wei, H.; Zheng, X.; Yu, Z.; Shao, Y.; Shield, J. E.; Huang, J. Strained Hybrid Perovskite Thin Films and Their Impact on the Intrinsic Stability of Perovskite Solar Cells. *Sci. Adv.* **2017**, *3* (11), eaao5616.

(13) Zhao, J.; Liu, M.; Fang, L.; Jiang, S.; Zhou, J.; Ding, H.; Huang, H.; Wen, W.; Luo, Z.; Zhang, Q.; et al. Great Disparity in Photoluminesence Quantum Yields of Colloidal CsPbBr3 Nanocrystals with Varied Shape: The Effect of Crystal Lattice Strain. *J. Phys. Chem. Lett.* **2017**, *8* (13), 3115–3121.

(14) Shi, D.; Adinolfi, V.; Comin, R.; Yuan, M.; Alarousu, E.; Buin, A.; Chen, Y.; Hoogland, S.; Rothenberger, A.; Katsiev, K.; et al. Low Trap-State Density and Long Carrier Diffusion in Organolead Trihalide Perovskite Single Crystals. *Science* **2015**, *347* (6221), 519–522.

(15) Nie, W.; Tsai, H.; Blancon, J.-C.; Liu, F.; Stoumpos, C. C.; Traore, B.; Kepenekian, M.; Durand, O.; Katan, C.; Tretiak, S.; et al. Critical Role of Interface and Crystallinity on the Performance and Photostability of Perovskite Solar Cell on Nickel Oxide. *Adv. Mater.* **2018**, *30* (5), 1703879.

(16) Park, B. W.; Philippe, B.; Gustafsson, T.; Sveinbjörnsson, K.; Hagfeldt, A.; Johansson, E. M. J.; Boschloo, G. Enhanced Crystallinity in Organic-Inorganic Lead Halide Perovskites on Mesoporous TiO2 via Disorder-Order Phase Transition. *Chem. Mater.* **2014**, *26* (15), 4466–4471.

(17) Li, C.; Guo, Q.; Zhang, H.; Bai, Y.; Wang, F.; Liu, L.; Hayat, T.; Alsaedi, A.; Tan, Z. Enhancing the Crystallinity of HC(NH2)2PbI3 Film by Incorporating Methylammonium Halide Intermediate for Efficient and Stable Perovskite Solar Cells. *Nano Energy* **2017**, *40*, 248–257.

(18) Almutawah, Z. S.; Watthage, S. C.; Song, Z.; Ahangharnejhad, R. H.; Subedi, K. K.; Shrestha, N.; Phillips, A. B.; Yan, Y.; Ellingson, R. J.; Heben, M. J. Enhanced Grain Size and Crystallinity in CH3NH3PbI3 Perovskite Films by Metal Additives to the Single-Step Solution Fabrication Process. *MRS Adv.* **2018**, 1–6.

(19) Rolston, N.; Bush, K. A.; Printz, A. D.; Gold-Parker, A.; Ding, Y.; Toney, M. F.; McGehee, M. D.; Dauskardt, R. H. Engineering Stress in Perovskite Solar Cells to Improve Stability. *Advanced Energy Materials*. Wiley-Blackwell October 1, 2018, p 1802139.

(20) Stoumpos, C. C.; Malliakas, C. D.; Peters, J. A.; Liu, Z.; Sebastian, M.; Im, J.; Chasapis, T. C.; Wibowo, A. C.; Chung, D. Y.; Freeman, A. J.; et al. Crystal Growth of the Perovskite Semiconductor $CsPbBr_3$: A New Material for High-Energy Radiation Detection. *Cryst. Growth Des.* **2013**, *13* (7), 2722–2727.

(21) Shrestha, S.; Fischer, R.; Matt, G. J.; Feldner, P.; Michel, T.; Osvet, A.; Levchuk, I.; Merle, B.; Golkar, S.; Chen, H.; et al. High-Performance Direct Conversion X-Ray Detectors Based on Sintered Hybrid Lead Triiodide Perovskite Wafers. *Nat. Photonics* **2017**, *11* (7), 436–440.

(22) Chung, D. Y.; Kanatzidis, M. G.; Meng, F.; Malliakas, C. D. Synthesis, Purification, and Characterization of Perovskite Semiconductor CsPbBr3 as a New Candidate for y-Ray Detector. *International Society for Optics and Photonics,* 2016; Vol. 9968, p 996819.

(23) Wei, H.; Fang, Y.; Mulligan, P.; Chuirazzi, W.; Fang, H. H.; Wang, C.; Ecker, B. R.; Gao, Y.; Loi, M. A.; Cao, L.; et al. Sensitive X-Ray Detectors Made of Methylammonium Lead Tribromide Perovskite Single Crystals. *Nat. Photonics* **2016**, *10* (5), 333–339.

(24) Zhang, L.; Geng, W.; Tong, C.; Chen, X.; Cao, T.; Chen, M. Strain Induced Electronic Structure Variation in Methyl-Ammonium Lead Iodide Perovskite. *Sci. Rep.* **2018**, *8* (1), 7760.

(25) Grote, C.; Berger, R. F. Strain Tuning of Tin-Halide and Lead-Halide Perovskites: A First-Principles Atomic and Electronic Structure Study. *J. Phys. Chem. C* **2015**, *119* (40), 22832–22837.

(26) Jiao, Y.; Ma, F.; Wang, H.; Bell, J.; Du, A. Strain Mediated Bandgap Reduction, Light Spectrum Broadening, and Carrier Mobility Enhancement of Methylammonium Lead/Tin Iodide Perovskites. *Part. Part. Syst. Charact.* **2017**, *34* (4), 1600288.

(27) Liu, G.; Kong, L.; Gong, J.; Yang, W.; Mao, H. K.; Hu, Q.; Liu, Z.; Schaller, R. D.; Zhang, D.; Xu, T. Pressure-Induced Bandgap Optimization in Lead-Based Perovskites with Prolonged Carrier Lifetime and Ambient Retainability. *Adv. Funct. Mater.* **2017**, *27* (3).

(28) Kong, L.; Liu, G.; Gong, J.; Hu, Q.; Schaller, R. D.; Dera, P.; Zhang, D.; Liu, Z.; Yang, W.; Zhu, K.; et al. Simultaneous Band-Gap Narrowing and Carrier-Lifetime Prolongation of Organic–Inorganic Trihalide Perovskites. *Proc. Natl. Acad. Sci.* **2016**, *113* (32), 8910–8915.

(29) Jiang, S.; Fang, Y.; Li, R.; Xiao, H.; Crowley, J.; Wang, C.; White, T. J.; Goddard, W. A.; Wang, Z.; Baikie, T.; et al. Pressure-Dependent Polymorphism and Band-Gap Tuning of Methylammonium Lead Iodide Perovskite. *Angew. Chemie Int. Ed.* **2016**, *55* (22), 6540–6544.

(30) Jaffe, A.; Lin, Y.; Beavers, C. M.; Voss, J.; Mao, W. L.; Karunadasa, H. I. High-Pressure Single-Crystal Structures of 3D Lead-Halide Hybrid Perovskites and Pressure Effects on Their Electronic and Optical Properties. *ACS Cent. Sci.* **2016**, *2* (4), 201–209.

(31) Wang, L.; Wang, K.; Xiao, G.; Zeng, Q.; Zou, B. Pressure-Induced Structural Evolution and Band Gap Shifts of Organometal Halide Perovskite-Based Methylammonium Lead Chloride. *J. Phys. Chem. Lett.* **2016**, *7* (24), 5273–5279.

(32) Wang, Y.; Lü, X.; Yang, W.; Wen, T.; Yang, L.; Ren, X.; Wang, L.; Lin, Z.; Zhao, Y. Pressure-Induced Phase Transformation, Reversible Amorphization, and Anomalous Visible Light Response in Organolead Bromide Perovskite. *J. Am. Chem. Soc.* **2015**, *137* (34), 11144–11149.

(33) Liu, G.; Kong, L.; Guo, P.; Stoumpos, C. C.; Hu, Q.; Liu, Z.; Cai, Z.; Gosztola, D. J.; Mao, H. K.; Kanatzidis, M. G.; et al. Two Regimes of Bandgap Red Shift and Partial Ambient Retention in Pressure-Treated Two-Dimensional Perovskites. *ACS Energy Lett.* **2017**, *2* (11), 2518–2524.

(34) Zhang, L.; Zeng, Q.; Wang, K. Pressure-Induced Structural and Optical Properties of Inorganic Halide Perovskite CsPbBr 3. *J. Phys. Chem. Lett.* **2017**, *8* (16), 3752–3758.

(35) Hall, G. N.; Stuckelberger, M.; Nietzold, T.; Hartman, J.; Park, J.-S.; Werner, J.; Niesen, B.; Cummings, M. L.; Rose, V.; Ballif, C.; et al. The Role of Water in the Reversible Optoelectronic Degradation of Hybrid Perovskites at Low Pressure. *J. Phys. Chem. C* **2017**, *121* (46), 25659–25665.

(36) Wang, Y.; Sun, X.; Chen, Z.; Cai, Z.; Zhou, H.; Lu, T. M.; Shi, J. Defect-Engineered Epitaxial VO2±din Strain Engineering of Heterogeneous Soft Crystals. *Sci. Adv.* **2018**, *4* (5).

(37) Khoram, P.; Brittman, S.; Dzik, W. I.; Reek, J. N. H.; Garnett, E. C. Growth and Characterization of PDMS-Stamped Halide Perovskite Single Microcrystals. *J. Phys. Chem. C* **2016**, *120* (12), 6475–6481.

(38) Holt, M.; Harder, R.; Winarski, R.; Rose, V. Nanoscale Hard X-Ray Microscopy Methods for Materials Studies. *Annu. Rev. Mater. Res.* **2013**, *43* (1), 183–211.

(39) Ying, A.; Osting, B.; Noyan, I. C.; Murray, C. E.; Holt, M.; Maser, J. Modeling of Kinematic Diffraction from a Thin Silicon Film Illuminated by a Coherent, Focused X-Ray Nanobeam. *J. Appl. Crystallogr.* **2010**, *43* (3), 587–595.

(40) M. Stuckelberger, T. Nietzold, G. Hall, B. West, X. Meng, J. Werner, B. Niesen, B. Lai, J. Maser, V. Rose, 4, C. Ballif, and M. I. B. X-Ray Beam Induced Degradation of Perovskite Solar Cells: Low Enough for Synchrotron Experiments. *Mater. Reseach Soc. Conf.* **2016**.

(41) Luo, Y.; Aharon, S.; Stuckelberger, M.; Magaña, E.; Lai, B.; Bertoni, M. I.; Etgar, L.; Fenning, D. P. The Relationship between Chemical Flexibility and Nanoscale Charge Collection in Hybrid Halide Perovskites. *Advanced Functional Materials*. May 2018, p 1706995.

(42) Rakita, Y.; Cohen, S. R.; Kedem, N. K.; Hodes, G.; Cahen, D. Mechanical Properties of APbX 3 (A = Cs or CH3NH3; X = I or Br) Perovskite Single Crystals. *MRS Commun.* **2015**, *5* (04), 623–629.

(43) Nagabhushana, G. P.; Shivaramaiah, R.; Navrotsky, A. Direct Calorimetric Verification of Thermodynamic Instability of Lead Halide Hybrid Perovskites. *Proc. Natl. Acad. Sci. U. S. A.* **2016**, *113* (28), 7717–7721.

(44) Jana, A.; Mittal, M.; Singla, A.; Sapra, S. Solvent-Free, Mechanochemical Syntheses of Bulk Trihalide Perovskites and Their Nanoparticles † For the First Time, We Have

Synthesized APbBr 3 (A = Cs + /MA + /FA + , Where MA + = CH 3 NH 3 + and FA + = CH(NH 2) 2 +. *Chem. Commun* **2017**, *3046*, 3046.

(45) Jones, T. W.; Osherov, A.; Alsari, M.; Sponseller, M.; Duck, B. C.; Jung, Y.-K.; Settens, C.; Niroui, F.; Brenes, R.; Stan, C.; et al. Lattice Strain Causes Non-Radiative Losses in Halide Perovskites. *Energy Environ. Sci.* **2019**.

(46) Chen, J.; Morrow, D. J.; Fu, Y.; Zheng, W.; Zhao, Y.; Dang, L.; Stolt, M. J.; Kohler, D. D.; Wang, X.; Czech, K. J.; et al. Single-Crystal Thin Films of Cesium Lead Bromide Perovskite Epitaxially Grown on Metal Oxide Perovskite (SrTiO3). *J. Am. Chem. Soc.* **2017**, *139* (38), 13525–13532.

(47) Yan, Y.; Yin, W.-J.; Shi, T.; Meng, W.; Feng, C. Defect Physics of CH3NH3PbX3 (X = I, Br, Cl) Perovskites. In *Organic-Inorganic Halide Perovskite Photovoltaics*; Springer International Publishing: Cham, 2016; pp 79–105.

(48) Brenes, R.; Guo, D.; Osherov, A.; Noel, N. K.; Eames, C.; Hutter, E. M.; Pathak, S. K.; Niroui, F.; Friend, R. H.; Islam, M. S.; et al. Metal Halide Perovskite Polycrystalline Films Exhibiting Properties of Single Crystals. *Joule* **2017**, *1* (1), 155–167.

(49) Adhyaksa, G. W. P.; Sarah Brittman, Haralds Āboliņš, Andries Lof, Xueying Li, Y.; Luo, Teodor Duevski, David P. Fenning, E. C. G. Understanding Detrimental and Beneficial Grain Boundary Effects in Halide Perovskites. *Adv. Mater.* **2018**, 1804792.

(50) Brenner, T. M.; Rakita, Y.; Orr, Y.; Klein, E.; Feldman, I.; Elbaum, M.; Cahen, D.; Hodes, G. Conversion of Single Crystalline PbI $_2$ to CH $_3$ NH $_3$ PbI $_3$: Structural Relations and Transformation Dynamics. *Chem. Mater.* **2016**, *28* (18), 6501–6510.

(51) Eperon, G. E.; Habisreutinger, S. N.; Leijtens, T.; Bruijnaers, B. J.; Van Franeker, J. J.; Dequilettes, D. W.; Pathak, S.; Sutton, R. J.; Grancini, G.; Ginger, D. S.; et al. The Importance of Moisture in Hybrid Lead Halide Perovskite Thin Film Fabrication. *ACS Nano* **2015**, *9* (9), 9380–9393.

(52) Tsai, H.; Asadpour, R.; Blancon, J.-C.; Stoumpos, C. C.; Durand, O.; Strzalka, J. W.; Chen, B.; Verduzco, R.; Ajayan, P. M.; Tretiak, S.; et al. Light-Induced Lattice Expansion Leads to High-Efficiency Perovskite Solar Cells. *Science* **2018**, *360* (6384), 67–70.

CHAPTER 2

Introduction

Halide perovskites are an emergent class of materials potentially suitable for most optoelectronic applications. Their intrinsic properties are commensurate with optoelectronic figures of merit, as they exhibit large absorption coefficients with sharp onsets, high photoluminescent yields, tunable bandgaps, long carrier lifetimes, and low intrinsic trap densities.[1–5] This, in conjunction with their facile, solution-based fabrication methods and wide-ranging flexibility in chemical composition, has made perovskites attractive candidates in the development of light-emitting diodes, lasers, phosphors, detectors, and indoor and outdoor photovoltaic cells.[6–17]

Halide perovskite materials possess the ABX_3 structure, where the chemical species on each of the A-, B-, and X- sites can be varied and mixed (within the bounds of structural formability guided by the Goldschmidt tolerance factor and related heuristics) to modulate the material's properties.[18–20] The composition of each site has been under investigation, but typically consists of either an organic (methylammonium or formamidinium) or inorganic (Cs) A-site, a divalent B-site (most often Pb), and a halide at the X-site (Br, Cl, I). Inorganic halide perovskites, most commonly of composition $CsPbX_3$, have been of particular interest for their thermal stability. [21] Variation of the X-site from chlorine to bromine to iodine adjusts the bandgap across the visible spectrum while preserving high photoluminescence quantum yields and narrow emission line widths.[22] The addition of lanthanide ions to $CsPbX_3$ perovskites improves the photoluminescent yields even further, extends the possible emission range into the

near-infrared, and in some cases enables new physics within the material as a divalent $2^+/3^+$ or aliovalent 3^+ dopant at the B-site.[23–26]

Of the lanthanide additives, europium has shown especially promising improvements to performance of both organic and inorganic perovskites. Europium-containing inorganic perovskite quantum dots display blue, green, and red emission with photoluminescent yields up to 90%, the red emission arising from quantum cutting between the host lattice and Eu^{3+}.[27,28] Strong excitonic binding in these quantum dots makes their PL yield less sensitive to particle size and morphology, allowing bright particles to be formed even within glass melts. [10] Solar cells fabricated with europium additives to the hybrid $MAPbI_3$ and inorganic $CsPbI_3$ and $CsPbI_2Br$ perovskite absorbers displayed increased power conversion efficiency and stability under conditions ranging from exposure to ambient atmosphere to prolonged one-sun illumination.[25,29–31] The improvement in stability has been ascribed to strain-induced stabilization of the kinetically-trapped photoactive perovskite phase and the suppression of ionic defects via "redox shuttling" between Eu^{2+} and Eu^{3+} ions. Existing literature has established both the benefits of europium to perovskites, as well as proposed the mechanisms by which some of these benefits are conferred. Incorporation of Eu onto the lattice in place of lead, its mitigation of deleterious redox reactions, and its influence on microstrain have been attributed to improving thethe optoelectronic and stability properties of perovskite devices.[25,29] Our work leverages high-resolution mapping techniques to evaluate these hypothesized mechanisms at the nanoscale.

In this study, we use synchrotron nanoprobe X-Ray Diffraction (nXRD) and Fluorescence (nXRF) mapping to investigate the nanoscale stoichiometry and microstructure of $CsPbBr_3$ crystal films with nominal 5% Eu^{2+} addition. Using micro-photoluminescence, we correlate the photoluminescence (PL) to local elemental composition and strain distribution. We

find that Eu addition clearly improves PL yield and line width with a minor blue-shift to the bandgap. This improved PL is ascribed to a reduction in microstrain seen by nXRD, which along with heterogeneity in europium content seen by nXRF indicates that the presence of europium changes the crystallization process. Finally, the stability of $CsPbBr_3$ under sustained hard x-ray dosage is greatly improved with the addition of europium. Our work sheds light on the local influence of europium on the structural and optoelectronic properties of perovskites, further supporting this class of materials as an encouraging prospect for use in applications ranging from light emission to high-energy photon detection.

Results and Discussion

We fabricated $CsPbBr_3$ crystals with and without 5% $EuBr_2$ (mol fraction with respect to the B-site) added to the precursor solution on quartz substrates, using a previously-established PDMS stamping method during annealing.[32] This fabrication approach results in isolated thin-film crystals typically 1 -2 μm thick and 20-30 μm wide (Figure S1). Inductively-Coupled Plasma Mass Spectrometry (ICP-MS) found the average Eu mol fraction in the Eu:$CsPbBr_3$ samples to be 4.8%, near the nominal 5% (Table S1).

Benchtop XRD confirms that both crystals with 5% mol $EuBr_2$ added (Eu:$CsPbBr_3$) and pristine $CsPbBr_3$ crystals form in the room-temperature orthorhombic phase (Pnma, ICSD #97851) **(Figure 1a)**. The Eu:$CsPbBr_3$ crystals show less texture than the $CsPbBr_3$, as the benchtop diffraction pattern clearly shows the Eu:$CsPbBr_3$ microcrystals exhibit a wider range of orientations. We do not observe a shift in the diffraction peaks upon addition of 5 mol% Eu^{2+}. This is not unexpected, as the ionic radii for octahedrally-coordinated Eu^{2+} and Pb^{2+} cations are similar at 117 and 119 pm, respectively.[33] Previous reports have shown europium to have

varying effects on the lattice parameter of perovskites, though there is consensus that europium can be incorporated into the perovskite crystal structure at moderate loadings with little to no effect on the lattice parameter.[25,29,34] For example, Wang *et al.* showed that, in methylammonium lead iodide, increasing europium loading does not affect the diffraction peak positions until 4.8 mol%, at which point they observe a peak shift indicating an increased lattice parameter.

Nano-Diffraction Shows Reduced Structural Disorder

To better understand the crystals' microstructure, synchrotron-based scanning nano-X-Ray Diffraction (nXRD) measurements were carried out on select individual crystals from each sample type. This technique rasters a 60-nm full-width half-maximum (FWHM) monochromatic X-ray probe across the sample and uses a 2D panel detector to collect the scattering produced at each point, generating a rich, nanoscale map of the structural properties.[35] nXRD is highly sensitive both in terms of detection limit and spatial resolving power. Minority crystal orientations and phases barely present or undetectable in benchtop XRD data can often be seen clearly in nXRD, although the total area sampled is limited currently to several 100s μm^2. Coupled with supporting characterization, from nXRD we obtain unique insights into the microstructural behavior of europium in $CsPbBr_3$.

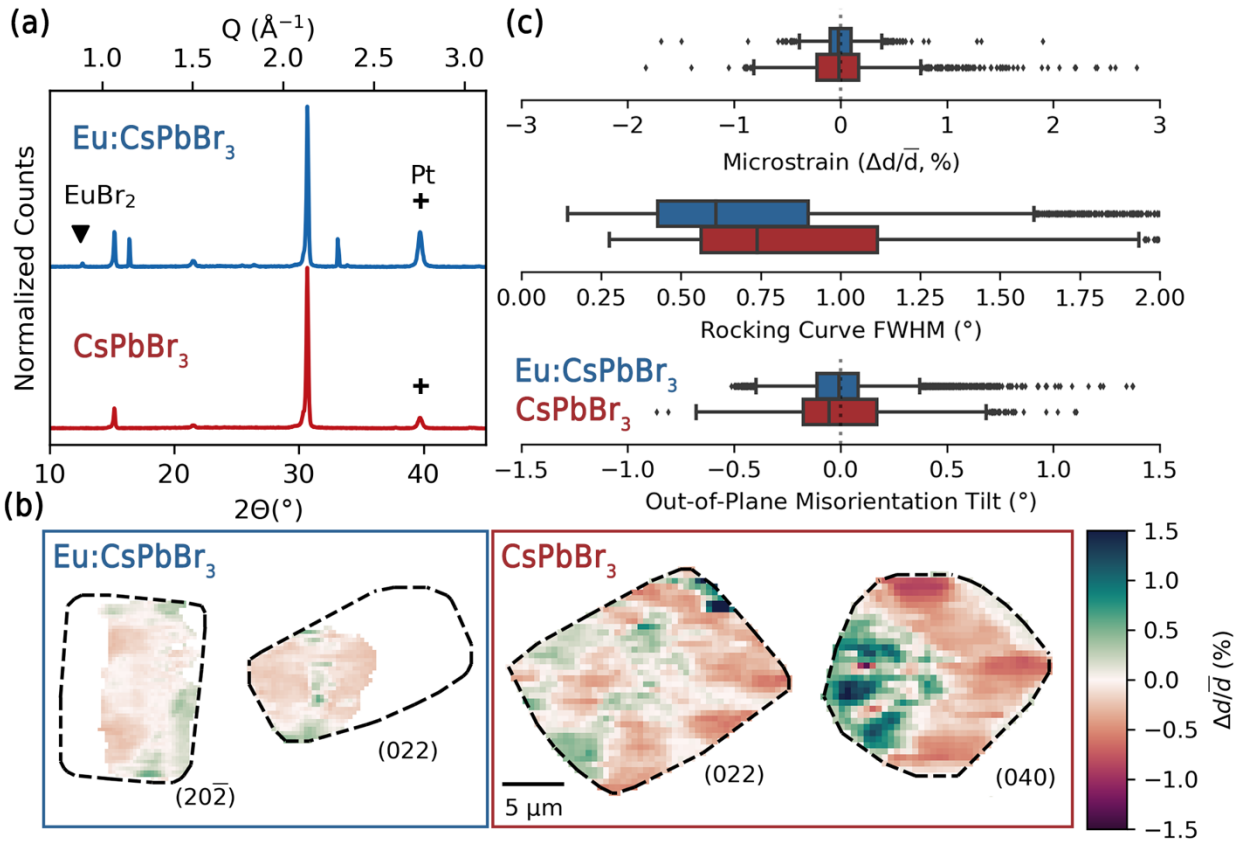

Figure 2.1. (a) Benchtop XRD patterns of $CsPbBr_3$ and Eu:$CsPbBr_3$ samples. All peaks other than that of the platinum (fiducial marks present on the sample substrate) and $EuBr_2$ are attributed to the orthorhombic perovskite. (b) Spatial distribution of relative *d*-spacing in two crystals of each sample type obtained by synchrotron nano-XRD. (c) Overall distributions of strain, diffraction peak width, and out-of-plane lattice tilt in the $CsPbBr_3$ and Eu:$CsPbBr_3$ samples, including all measured data (additional data shown in the SI).

The nXRD reveals that, unlike the $CsPbBr_3$, the individual Eu:$CsPbBr_3$ "crystals" are, in fact, multicrystalline, with crystallites diffracting from multiple orientations present across the crystal area. Fig 1(b) shows a nanoscale map of microstrain in two exemplary crystals of each type, showing the variation in *d*-spacing relative to the average value within the crystallite. Only a fraction of the geometric area of the Eu:$CsPbBr_3$ crystals diffract to a particular Bragg angle. The Eu:$CsPbBr_3$ remain fully crystalline, but other orientations account for the diffraction from

areas of the crystal in white in Fig 1 (b). The full set of orientations and their corresponding microstrain is shown in **Figure S2**. In the case of the pristine samples, one orientation is dominant and expressed across the entire crystal area (Figure 1b). This suggests that the addition of europium to $CsPbBr_3$ precursors alters the crystallization process and promotes the formation of smaller crystalline domains.

As can be seen from the scanning nano-diffraction, the strain state varies substantially within individual domains, with much higher levels of microstrain in the pristine $CsPbBr_3$. The intensity of color in Fig. 1b indicates the local deviation in *d*-spacing relative to the average *d*-spacing observed across the crystal area. These deviations contribute on aggregate to the microstrain seen in a benchtop measurement. The Eu:$CsPbBr_3$ sample exhibits less microstrain than the $CsPbBr_3$ sample. Furthermore, the gradient of *d*-spacing (how fast the color changes in Fig. 1b) across the Eu:$CsPbBr_3$ crystals is lower in magnitude than in $CsPbBr_3$, meaning that the strain state is more homogenous across these samples with smaller absolute values. This finding is summarized in the boxplots at the top of Fig. 1c, where the distribution of *d*-spacing variation is narrower for Eu:$CsPbBr_3$. Note that while we can confidently observe microstrain, we have not reported the absolute strain value. For the polycrystals, reporting an absolute strain by just one orientation may give an incomplete picture. However, we see a clear reduction in the overall microstrain of crystals containing europium.

The Eu:$CsPbBr_3$ crystals also display a lower degree of mosaicity, *i.e.,* less tilting of the lattice across each crystalline domain, and reduced rocking curve full-width half-maximum (Figure 1c). The reduced rocking curve FWHM indicates reduced structural disorder within the nanoscopic X-ray probe interaction volume. Peak broadening can signal multiple structural phenomenon, such as lattice defects (dislocations, interstitials, etc.), mosaicity, varying strain

state, or small diffracting domains.[36] We do not expect much domain-size broadening here as the planar area of our diffracting domains are tens of microns across, and the thicknesses associated with domain-size broadening (<100 nm) would imply unlikely domains with extremely high aspect ratios. This leaves us to conclude that the broadening we observe consists of lattice defects and the already identified mosaicity and strain variation in our sample. On the whole, the nXRD paints an interesting picture of europium's impact on the $CsPbBr_3$ microstructure: we find evident polycrystallinity and decrease in texture, indicating a reduction in crystallographic order at long length scales (microns), but also improvement of short- to medium-range structural order, including reduced structural defect density and mosaicity.

Only small amounts of second phases, which we attribute to unreacted precursors, can be seen via nXRD and are primarily located around the perimeter of the crystals (**Figure S3**). We identify these as $EuBr_2$ and $PbBr_2$, though the proximity of reflections from these phases in reciprocal space makes assignment in nXRD difficult. In the Eu:$CsPbBr_3$ samples, the benchtop XRD (taken before the nXRD) clearly shows $EuBr_2$, implying that this $EuBr_2$ is unreacted precursor rather than a degradation product. In the case of the europium-free $CsPbBr_3$ samples we can confidently assign the precursor diffraction to $PbBr_2$.

Composition and Surface Chemistry of Eu:$CsPbBr_3$ Crystals

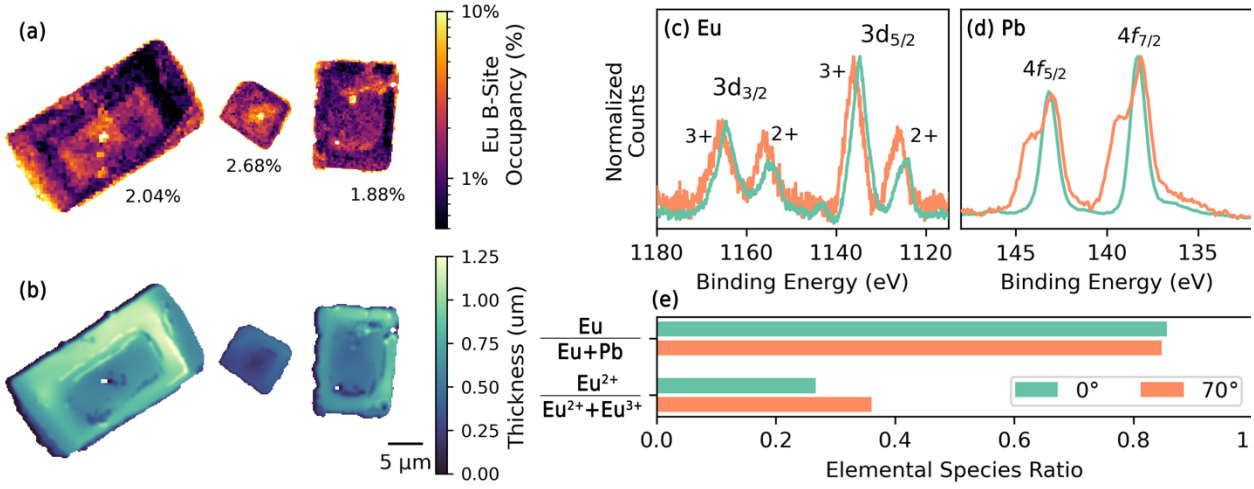

Figure 2.2. (a) Implied europium B-site occupancy as measured by synchrotron nano-XRF microscopy. The average is indicated below each crystal. (b) Thickness images corresponding to the crystals above. Scale bar is shared between (a) and (b). (c) Eu 3d and (d) Pb 4f XPS spectra, taken at normal (green) and grazing angles of incidence (orange). (e) The ratios between Eu oxidation states, and between Eu and Pb content, from the above XPS spectra.

Europium is Heterogeneously Incorporated

Nano-X-Ray Fluorescence (nXRF) microscopy reveals that the local B-site stoichiometry varies spatially across all Eu:$CsPbBr_3$ samples, from trace amounts up to local concentrations of 10% Eu (Figure 2a). With detection of only minor amounts of $EuBr_2$ in these samples and no clear evidence of other impurity phases from benchtop or nXRD, we evaluate B-site stoichiometry in terms of the implied Eu B-site occupancy $M_{Eu}/(M_{Eu} + M_{Pb})$, where M is the areal molar concentration (mol/cm^2) of the chemical species (shown for all crystals in Figure S4), and all europium and lead ions are assumed to be incorporated into the perovskite lattice. Note that these values are in areal concentration – nXRF provides compositional quantification integrated along the beam path, in this case integrating through the vertical dimension of the film. Eu-occupancy peaks as high as 10% at the crystal center, then decays to trace levels

towards the crystal edges **(Figure 2a)**. The average content is about 2-2.5%, somewhat lower than the ICP-MS value of 4.8%. Unlike nXRF, ICP-MS averages over the total contents of the substrate, implying that either our nXRF sample size is too small to capture the true average Eu-occupancy, or that residual Eu species are present on the substrate outside of the perovskite after fabrication. The latter seems to be true in our case given that we observe unreacted $EuBr_2$ around the crystals by both benchtop XRD and nXRD. This 2.5% measured Eu occupancy is consistent with our lack of any observed diffraction peak shifts, as seen at similar concentrations in Eu:$MAPbI_3$. [25] The Eu:$CsPbBr_3$ crystals are thinner in the center, as measured by white-light interferometry (Figure 2b), with larger concentrations of europium being present in these thinner regions. The $CsPbBr_3$ crystals do not have this thin-center morphology and are generally thicker than their europium-containing counterparts **(Figure S5)**.

The Crystal Surfaces are Rich in Europium

To better understand the chemistry and distribution of Eu in the crystals, we conducted angle-dependent XPS measurements. The spectra were collected at 0° and 70° angles of incidence to probe depth-dependent variations in chemical composition and oxidation state within the first few nanometers of the crystal surface. The Eu 3d and Pb 4f spectra are shown in Figure 2c-d (corresponding fits to the data are shown in Figure S6). Focusing on the Eu 3d spectra, we see doublets corresponding to both Eu^{2+} and Eu^{3+}.[37] Notably, we introduce only Eu(II), whereas most previous reports introduce the more common Eu(III). The chemistry in the thin film crystals is in the end similar to previous reports, where we find a coexistence of Eu^{2+}/Eu^{3+} oxidation states within the sample.[25,34] The population of Eu^{2+} may be slightly higher at the surface (Figure 2e) based upon the increase seen when moving from normal to grazing incidence. We note that these peak ratios qualitatively rather than quantitatively reflect the

relative population of the species, given the unknown depth distribution and the heterogeneity evident in the sample. The Pb 4f spectra in Figure 2d reveal the appearance of a high-binding energy peak in the surface-sensitive 70° spectrum, consistent with the native oxide of lead.[38]

Figure 2e also shows that the implied Eu B-site fraction at the surface is Eu-rich, reaching 80%, as derived from the XPS after accounting for the spectral relative sensitivity factors (RSF). This evident surface enrichment, in conjunction with the nXRD identification of unreacted $EuBr_2$ precursor primarily around the edge of the crystal, suggests that at least a portion of the europium added during synthesis segregates to the outer crystal surfaces. Even so, the numbers point to a significant degree of europium incorporation within the bulk crystal. If the first 5 nanometers of the micron-thick crystals have 80% Eu-occupancy as measured by XPS, the bulk crystal would still need to have an average 1.6% Eu-occupancy to yield the thickness-integrated 2% value detected by nXRF. This presents just a ~25% error in the bulk europium loading determined by nXRF and maintains the observation that the bulk of the Eu:$CsPbBr_3$ crystals are rich in europium while maintaining the perovskite phase.

Photoluminescence Intensity Increases with Europium Addition

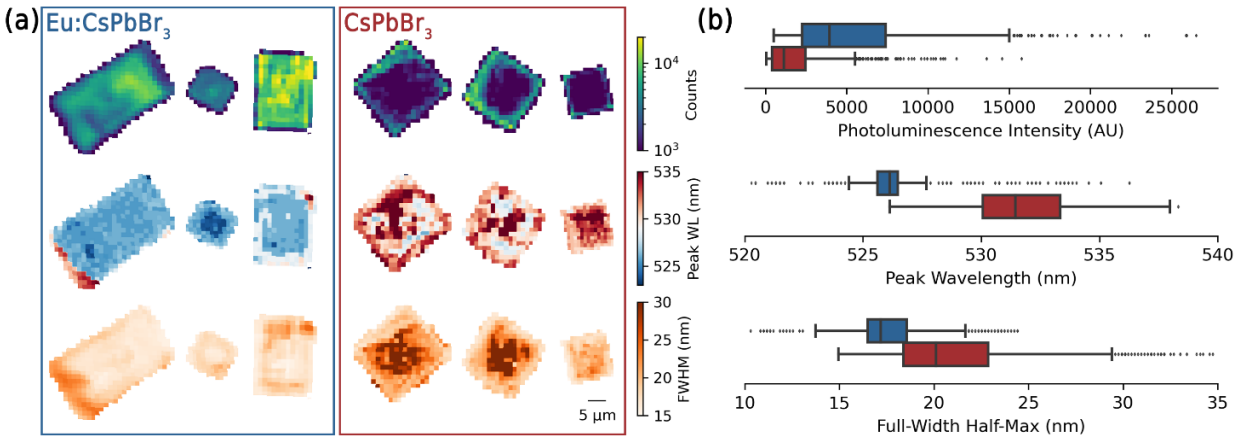

Figure 2.3. Photoluminescence behavior. a) Maps of photoluminescence intensity, peak emission wavelength, and emission full-width half-max for representative Eu:$CsPbBr_3$ crystals (left) and $CsPbBr_3$ (right). b) Overall distributions of the fitted photoluminescence parameters from (a).

Eu:$CsPbBr_3$ crystals display superior photoluminescence properties with respect to their pristine counterparts. **Figure 3a** shows micro-photoluminescence maps of the intensity (top row), peak wavelength of emission (middle row), and FWHM (bottom row) for the Eu:$CsPbBr_3$ (left) and $CsPbBr_3$ crystals (right). The Eu:$CsPbBr_3$ crystals show brighter photoluminescence (PL) on average, with roughly 2x higher intensity as seen in the summary box plot of Fig. 3b. The Eu:$CsPbBr_3$ crystals show strong luminescence from much of the crystal area, while the $CsPbBr_3$ crystals show strong edge-to-center variation with the edges being substantially brighter than the central regions of the crystal. The emission spectra of Eu:$CsPbBr_3$ are blue-shifted by about 5 nm on average and have lower FWHM relative to $CsPbBr_3$. These changes suggest that Eu incorporation improves the optoelectronic quality of in the perovskite by reducing shallow trap states that would serve to broaden the emission spectrum and reduce band-to-band recombination. Where the Eu:$CsPbBr_3$ crystals show relatively uniform emission spectrum across the area of the crystal, the $CsPbBr_3$ crystals show a chaotic distribution of red- and blue-

shifted regions. This varying distribution of emission point-to-point (~4.6 nm standard deviation) echoes the substantial variations in strain seen in the pristine crystals (Figure 1b). This is consistent with our previously reported finding that local strain leads directly to luminescence peaks shifts in $CsPbBr_3$.[39] Both crystal chemistries display an edge-to-center variation in emission wavelength, though the direction of these trends are reversed – the edges are redshifted in $Eu:CsPbBr_3$, but blue-shifted in $CsPbBr_3$. The redshift towards the edges in europium containing samples is further evidence that europium incorporation lowers the emission wavelength, given that nXRF shows Eu-occupancy to decrease from center to edge.

Stability Under X-Rays

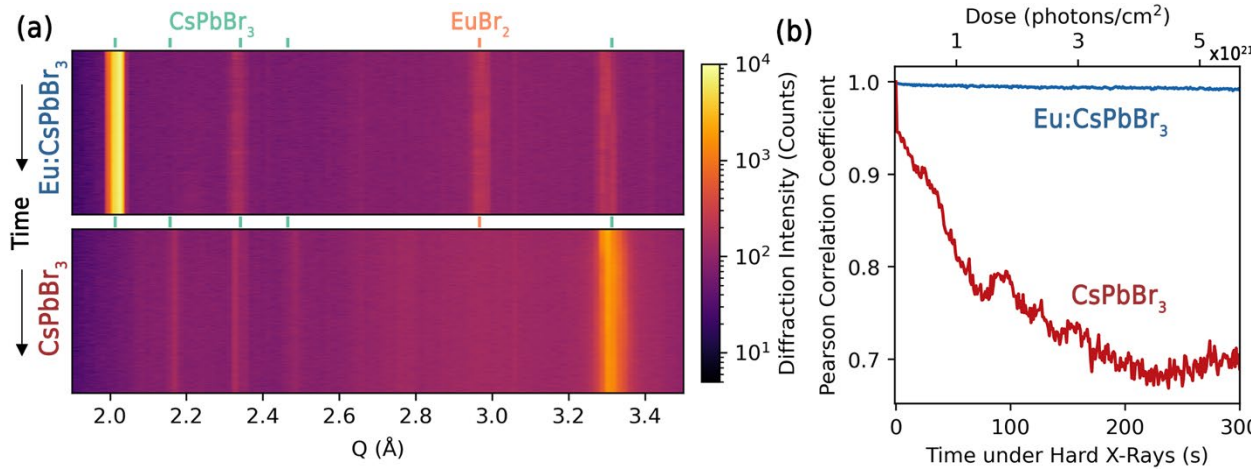

Figure 2.4. Structural stability. (a) Waterfall plots of diffraction patterns of $Eu:CsPbBr_3$ and $CsPbBr_3$ crystals exposed to sustained focused hard x-rays for 5 minutes. Diffracting phases are indexed by tick marks above the plots. (b) Statistical correlation over time between the images of the diffraction patterns collected by the area detector, corresponding to the waterfall plots in (a).

The incorporation of Eu dramatically improves the radiation hardness of the crystal, a key criterion for application in high-energy particle detection or in extreme environments. The structural stability of Eu:$CsPbBr_3$ and $CsPbBr_3$ crystals was examined under continuous 10 keV hard x-ray exposure at ~1.9 x 10^{21} photons/cm^2 /s. Waterfall plots of the time-resolved diffraction during X-ray exposure are shown in **Figure 4a** for Eu:$CsPbBr_3$ (top) and $CsPbBr_3$ (bottom). The $CsPbBr_3$ shows significant structural degradation. The strongest diffraction peak at 3.3$Å^{-1}$ in the $CsPbBr_3$ sample shifts to higher diffraction angles during the beam exposure, a "lattice collapse" mode of structural integrity loss we commonly observe when exposing sensitive perovskites to high doses of focused hard x-rays.[39] Loss of crystallographic structure can manifest in peak shifts, as severed atomic bonds cause *d*-spacings to change, and in peak intensity loss, as portions of the diffracting domain become disordered. Pearson correlation of the time-resolved area diffraction images to the initial image takes both of these degradation signatures into account and shows that europium imparts much greater structural stability and radiation hardness to the crystal (Figure 4b). Some minor instability remains even in the Eu:$CsPbBr_3$ – we note that a peak splitting of the 3.3$Å^{-1}$ peak persists after ~100s exposure (Figure 4a). Despite its multicrystallinity, the reduced microscopic structural disorder in Eu:$CsPbBr_3$ dominates overall to improve x-ray hardness.

Discussion

Our results make clear that europium addition has a pronounced effect on the nucleation and growth of $CsPbBr_3$ crystals. Based on the heightened europium content at the crystal centers it seems as though europium clustering may act as a seed for nucleation and encourage polycrystallinity. Additionally, XPS shows that europium is enriched at the surface. It is possible that europium-rich surface layers are acting as a passivation layer for the perovskite crystals.

In looking towards device applications requiring charge extraction, such as photovoltaics or optical sensors, the increased polycrystallinity concomitant with europium addition may reduce device performance by hindering long range charge transport. If columnar grain structures can be maintained, such devices may still produce enhanced performance. Various literature reports, including successful solar cell fabrication with Eu:$CsPbBr_3$, suggest that the growth kinetics of europium in perovskites can be overcome to yield performant optoelectronic devices.[25,30,34] As in our findings, europium-containing perovskite solar cells are consistently reported to have reduced grain sizes and improved stability against illumination or environmental stresses. Further work investigating the role of europium in perovskite synthesis kinetics is needed to establish methods for increasing crystalline domain size while preserving improved optoelectronic and microstructural quality.

Finally, though we have investigated the local role of europium in an inorganic perovskite, a wide range of halide perovskites incorporating lanthanides in quantum dots and thin films have been shown.[23,26,27] The bulk behavior of devices under study is generally of greatest interest and the figure of merit, but may overlook key aspects of local interactions between the ionic species of the additive and the host lattice, whether from elemental segregation, microstrain, or simply deviation between nominal and actual loadings of additives in strongly performing samples. Microscopic understanding of the compositions and structure must be established to understand their true tradeoffs and implications, especially for long-term device stability.

Conclusion

We investigate the microstructural underpinnings of the enhancements brought by europium addition to perovskite optoelectronics. The electronic quality of Eu:$CsPbBr_3$ is improved to yield an increased fraction of band-to-band recombination and fewer shallow traps, as evidenced by the increase in photoluminescence intensity and decrease in emission bandwidth. We use scanning X-ray nano-diffraction to show that these improved emission characteristics appear correlated to a reduction in microstrain at the nanoscale. Despite having a multicrystalline microstructure, the europium-added samples have less microstrain and exhibit less mosaicity than pristine $CsPbBr_3$. The reduced nanoscopic structural disorder corresponds with greatly improved radiation hardness of Eu:$CsPbBr_3$. The improved luminescence yield and increased stability make Eu addition a promising strategy for the engineering reliable photodetectors across the electromagnetic spectrum, including X-ray and gamma-ray detectors - an application for which inorganic perovskites have shown significant promise.[40]

Experimental Section/Methods

Sample Synthesis*:* Substrates were cleaned via a series of sonication and rinse steps as follows: sonication in 2 vol% Hellmanex in DI water for 15 min, rinse with DI water, sonication in DI water for 15 minutes, rinse with DI water, sonication in IPA for 15 min, sonication in acetone for 15 min, rinse with IPA, then dried. 0.33 M precursor solution (molar ratios of 1:1 CsBr:$PbBr_2$ for $CsPbBr_3$, and 1:0.95:0.05 CsBr:$PbBr_2$:$EuBr_2$ for Eu:$CsPbBr_3$ samples) was made in DMSO inside a nitrogen glovebox. The solution was heated to 120˚C and mixed by vortexing until all solids dissolved. The clean substrates were plasma-treated for 10 mins, in air at 200 mbar. The PDMS stamps were preheated on a hotplate at 150˚C. 40uL of precursor solution was dropped on the substrate. The substrate was spun for 10 seconds at 500 rpm (accelerated at 500

rpm/s), then put upside down on the PDMS and pressed with tweezer for 5 minutes. Then the substrate was removed from the PDMS, flipped over and heated for another 2 minutes at 150°C.

Inductively-Coupled Plasma Mass Spectrometry*:* The relative molar ratios of Eu, Pb and Cs were measured using a Thermo Scientific iCAP RQ ICP-MS. The as-grown crystals were scraped off the substrates and dissolved in 2% analytical grade nitric acid in preparation for the measurement.

Benchtop X-Ray Diffraction: The XRD of the samples was acquired on a Rigaku Smartlab with 0.02 degrees per step from 10˚ to 50˚ with 2mm slit in parallel beam mode. Samples were measured on directly on the substrate they were synthesized on.

Synchrotron X-Ray Fluorescence and X-Ray Diffraction*:* Nano-XRF and nano-XRD were both acquired at the 26-ID-C beamline at the Center for Nanoscale Materials and the Advanced Photon Source at Argonne National Laboratory, using a focused 10 keV x-ray beam. *d*-spacing was determined precisely by performing a spatially-resolved rocking curve, where the incident and detector angles were held constant while the sample theta was rotated. The 2D scattering detector was calibrated by measurement of a powder silicon reference sample. This procedure enables complete reconstruction of the 3D scattering vector at each point, which allows us to know not only the magnitude of the scattering (*d*-spacing), but the direction of scattering (relative lattice tilt). Additionally, the peak width of overall scattering intensity vs sample theta is fit to provide a measure of local structural disorder. XRF readings were corrected for attenuation of both the incident and fluoresced x-rays, using the nominal stoichiometry (5% Eu:$CsPbBr_3$ or pristine $CsPbBr_3$) and a density of 4.42 g/cm^3 to approximate the X-ray attenuation coefficient of the sample. In addition to the attenuation coefficient, the optical path

length of both the incident and fluoresced photons was approximated using a ray-tracing approach, where the incident beam and detector orientations are known from the measurement geometry, and the 3-d sample morphology is approximated using the white-light interferometry thickness map under the assumption that no voids exist within the sample. This treatment, along with a detector calibration using NIST XRF standards (NBS1832, NBS1833) normalizes the measured fluorescence to remove hardware and sample attenuation effects and enable quantitative analysis.

Thickness Measurement*:* The topography of the crystals was measured with a Filmetrics Profilm3D in White Light Interferometry mode with 50X magnification.

X-Ray Photoelectron Spectroscopy (XPS*):* XPS spectra were acquired using a Kratos Analytical AXIS Supra equipped with a monochromatic Al K-alpha x-ray source at the UC Irvine Materials Research Institute. Measurements were taken at 0˚ and 70˚ angles of incidence, acquired with a 20 eV pass energy at 0.1 eV steps with 100 ms dwell time. Spectra were background corrected using a Shirley background, aligned in energy using adventitious carbon, corrected by the instrument and element specific sensitivity factors (2.467 for Eu 3d, 8.329 for Pb 4f), and peaks were fit by Voigt line shapes to find peak areas.

Micro-Photoluminescence*:* Photoluminescence maps were taken using a Renishaw Raman/microPL tool with a 514nm excitation laser, 600 mm grating, 0.5s dwell time and 0.05% power. The photoluminescence peak position, intensity, and FWHM were extracted by a single-Gaussian fitting of the raw data.

Acknowledgements

Chapter 2, in full, is a reprint of the material as it appears in Europium Addition Reduces Local Structural Disorder and Enhances Photoluminescent Yield in Perovskite CsPbBr3 in Advanced Optical Materials 2021. Quinn, Xueying L.; Kumar Rishi E.; Kodur, Moses; Cakan, Deniz N.; Holt, Martin V.; Cai, Zhonghou; Zhou, Tao; Fenning, David P. The dissertation author was the primary author of this paper.

Xueying L. Quinn and Rishi E. Kumar contributed equally to this work. This work was supported in part by the National Science Foundation under Grant No. DMR-1848371. Use of the Center for Nanoscale Materials and the Advanced Photon Source, both Office of Science user facilities, was supported by the U.S. Department of Energy, Office of Science, Office of Basic Energy Sciences, under contract no. DE-AC02-06CH11357. This work was performed in part at the San Diego Nanotechnology Infrastructure (SDNI) of UCSD, a member of the National Nanotechnology Coordinated Infrastructure, which is supported by the National Science Foundation (grant ECCS-1542148).

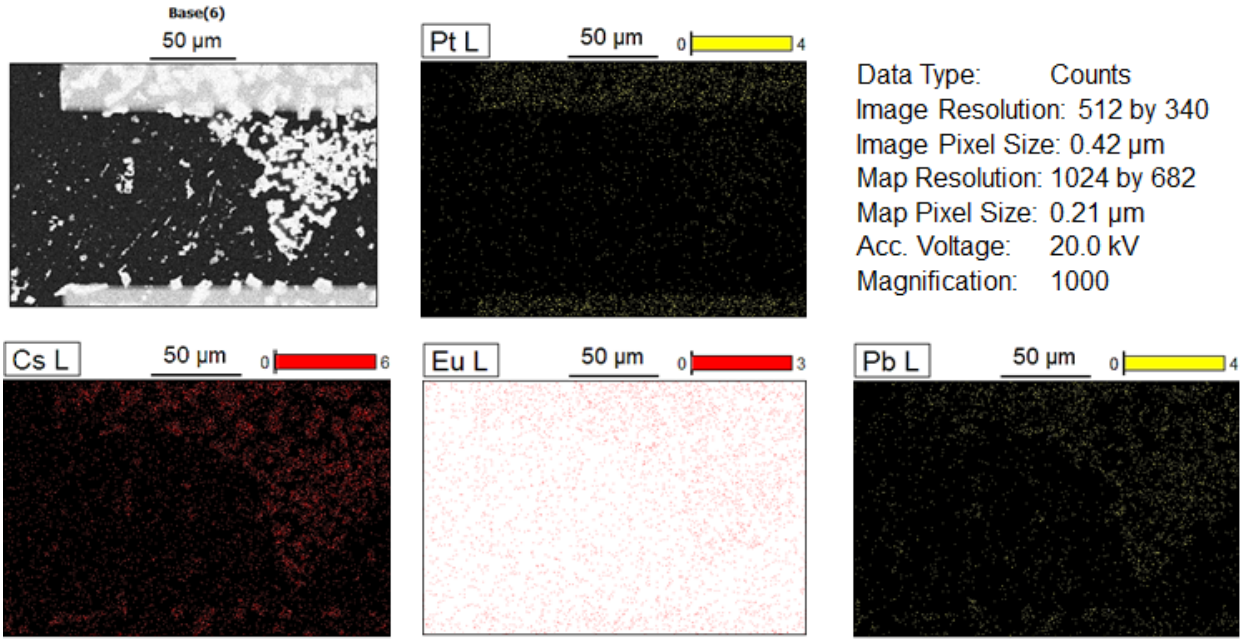

Figure 2.S1. SEM EDS maps of the Eu:$CsPbBr_3$ crystals on a quartz substrate with platinum fingers (horizontal at top and bottom of image) used as fiducial markers for sample location during measurements.

Table 2.S1. ICP-MS quantification results for $CsPbBr_3$ (top) and Eu:$CsPbBr_3$ (bottom) samples scraped off of the quartz/platinum finger substrate. The rightmost column represents the molar fraction $\frac{mol_{Eu}}{mol_{Eu}+mol_{Pb}}$

Nominal Eu/(Eu+Pb) (mol)	**Pb (ppb)**	**Eu (ppb)**	**Cs (ppb)**	**Pb (molarity)**	**Eu (molarity)**	**Cs (molarity)**	**Measured Eu/(Eu+Pb) (mol)**
0	65.579	0.006	30.030	0.317	0.000	0.226	0.000
0.05	249.237	8.936	161.03	1.204	0.059	1.211	0.047

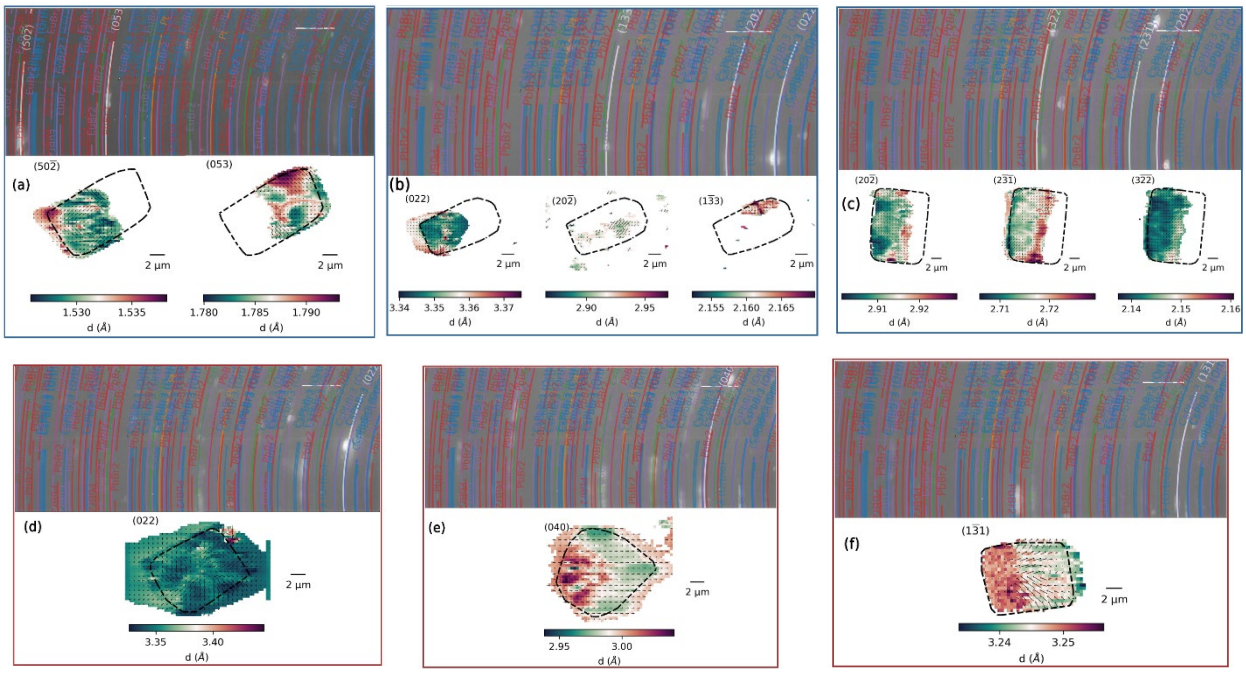

Figure 2.S2. The full collection of nano X-Ray Diffraction (nXRD) rocking curve maps, along with the integrated area-detector diffraction signal acquired across all sample orientations and spatial coordinates included in the map. The rings imposed on the detector image indicate expected reflections for chemical compounds potentially present in our system. Rings are colored by compound, with the exception of the white rings, which all correspond to *pnma* $CsPbBr_3$ and are resolved to yield *d*-spacings in the maps below the detector image. The Eu:$CsPbBr_3$ samples (a-c, blue boxes) each have multiple maps shown, as there were more than one diffracting orientations that were resolved per rocking curve across the sample area. $CsPbBr_3$ crystals are in red boxes (d-f). The *d*-spacing maps are segmented to only display areas above a threshold diffraction intensity. The dashed lines on the maps indicate the edges of the particle as seen by the cesium XRF signal – the diffraction signal outside this region is a product of beam spreading in the x-direction, as the beam is projected due to the Bragg orientation of the crystal at ~15° to the sample surface.

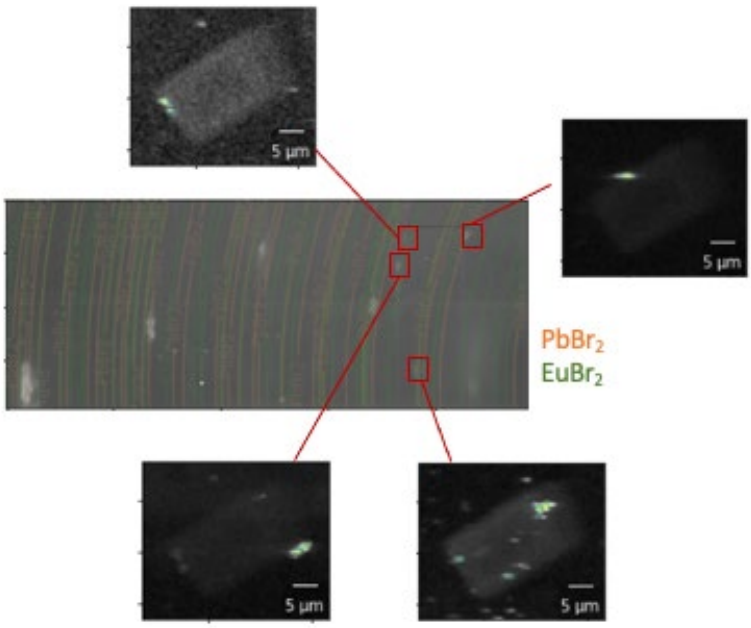

Figure 2.S3. Diffracting areas corresponding to either $EuBr_2$ or $PbBr_2$ in Eu:$CsPbBr_3$ sample "B" from the Figure S2. The same integrated area detector image from Figure S2 is shown here, with only phase lines corresponding to $EuBr_2$ and $PbBr_2$ shown. The red boxes indicate the region of the detector (*i.e.,* reciprocal space) considered for each of the four perimeter images, which show the integrated counts from that region (strongest diffracting portions of the map are highlighted). The majority of the precursor phases are detected at the edge of the crystal area.

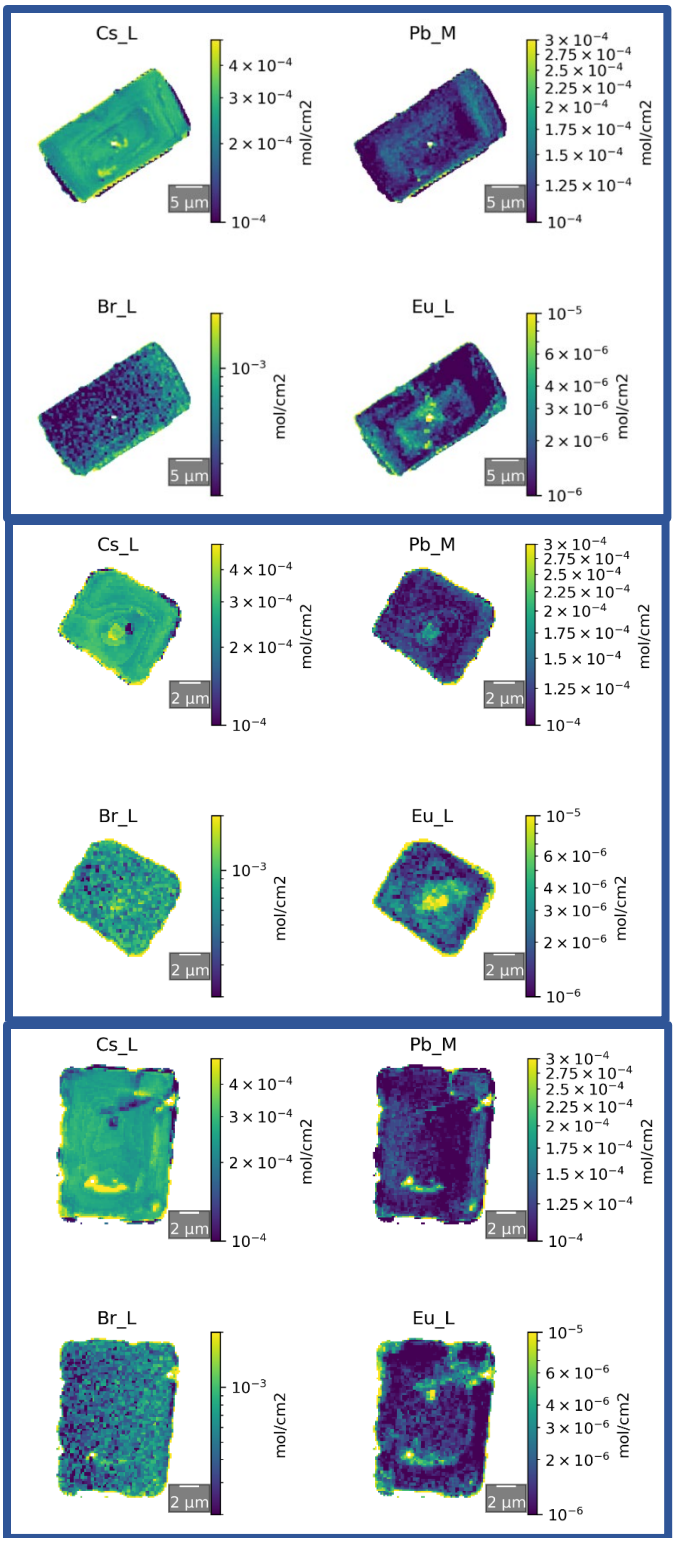

Figure 2.S4. Nano XRF maps of Eu:$CsPbBr_3$ samples show the areal molar concentration of each element (mol/cm2).

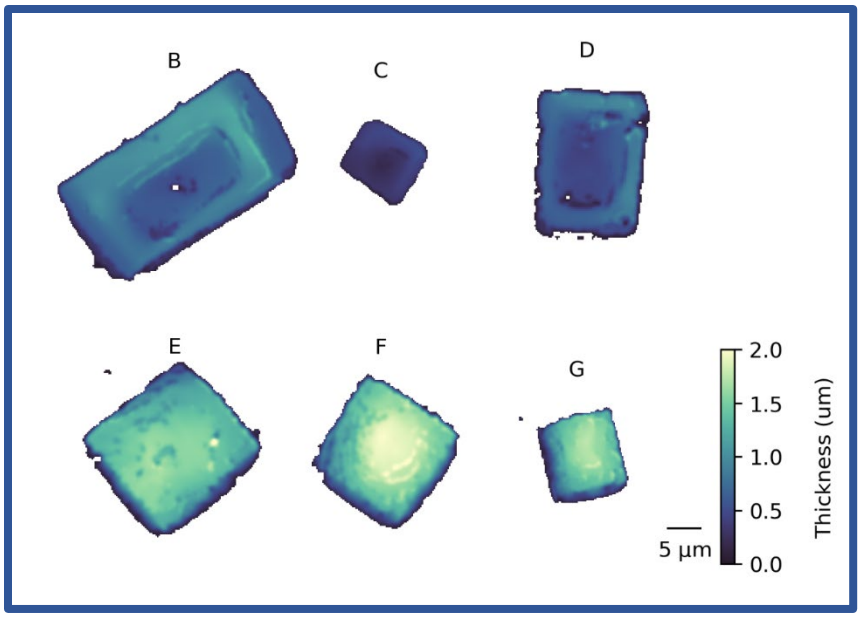

Figure 2.S5. Thickness maps of three Eu:$CsPbBr_3$ (top, B-D) and three $CsPbBr_3$ (bottom, E-G) samples.

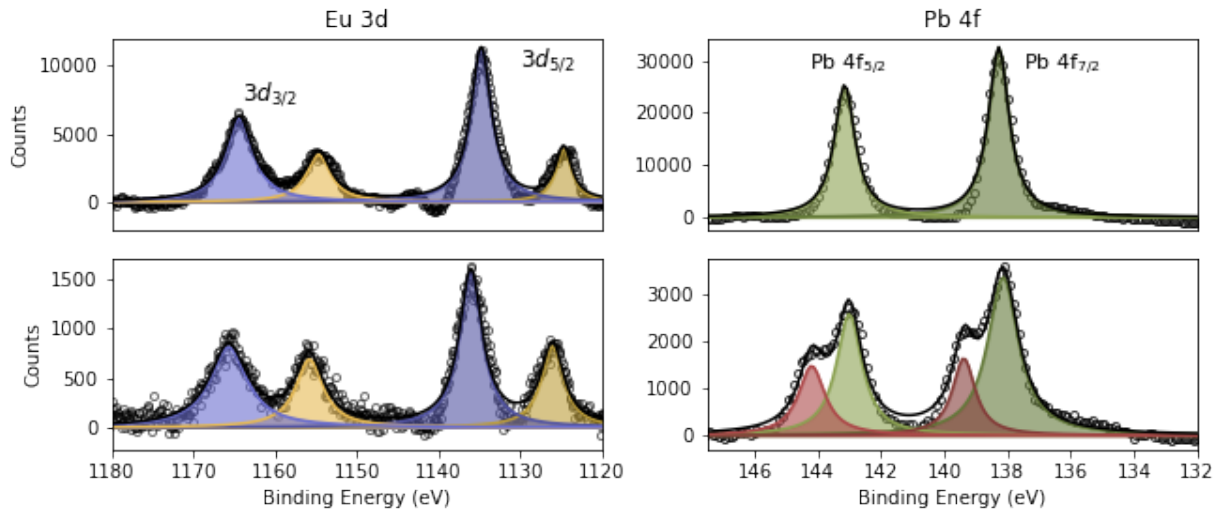

Figure 2.S6. XPS Spectra and Voigt fits for Eu:$CsPbBr_3$ samples. The upper two plots are taken at 0˚ angle of incidence, while the bottom two are taken at 70˚.

REFERENCES

[1] B. R. Sutherland, E. H. Sargent, *Nat. Photonics* **2016**, *10*, 295.

[2] S. De Wolf, J. Holovsky, S. J. Moon, P. Löper, B. Niesen, M. Ledinsky, F. J. Haug, J. H. Yum, C. Ballif, *J. Phys. Chem. Lett.* **2014**, *5*, 1035.

[3] S. D. Stranks, V. M. Burlakov, T. Leijtens, J. M. Ball, A. Goriely, H. J. Snaith, *Phys. Rev. Appl.* **2014**, *2*, 034007.

[4] H. J. Snaith, A. Abate, J. M. Ball, G. E. Eperon, T. Leijtens, N. K. Noel, S. D. Stranks, J. T.-W. W. Wang, K. Wojciechowski, W. Zhang, *J. Phys. Chem. Lett.* **2014**, *5*, 1511.

[5] S. D. Stranks, G. E. Eperon, G. Grancini, C. Menelaou, M. J. P. Alcocer, T. Leijtens, L. M. Herz, A. Petrozza, H. J. Snaith, *Science (80-.).* **2013**, *342*, 341.

[6] C. Sun, Y. Zhang, C. Ruan, C. Yin, X. Wang, Y. Wang, W. W. Yu, *Adv. Mater.* **2016**, *28*, 10088.

[7] L. Zhang, X. Yang, Q. Jiang, P. Wang, Z. Yin, X. Zhang, H. Tan, Y. M. Yang, M. Wei, B. R. Sutherland, E. H. Sargent, J. You, *Nat. Commun.* **2017**, *8*, DOI: 10.1038/ncomms15640.

[8] J. Liang, C. Wang, Y. Wang, Z. Xu, Z. Lu, Y. Ma, H. Zhu, Y. Hu, C. Xiao, X. Yi, G. Zhu, H. Lv, L. Ma, T. Chen, Z. Tie, Z. Jin, J. Liu, *J. Am. Chem. Soc.* **2016**, *138*, 15829.

[9] C. Liu, W. Li, C. Zhang, Y. Ma, J. Fan, Y. Mai, *J. Am. Chem. Soc.* **2018**, *140*, 3825.

[10] A. Swarnkar, R. Chulliyil, V. K. Ravi, M. Irfanullah, A. Chowdhury, A. Nag, *Angew. Chemie - Int. Ed.* **2015**, *54*, 15424.

[11] M. Saliba, S. M. Wood, J. B. Patel, P. K. Nayak, J. Huang, J. A. Alexander-Webber, B. Wenger, S. D. Stranks, M. T. Hörantner, J. T. W. Wang, R. J. Nicholas, L. M. Herz, M. B. Johnston, S. M. Morris, H. J. Snaith, M. K. Riede, *Adv. Mater.* **2016**, *28*, 923.

[12] Q. Zhang, S. T. Ha, X. Liu, T. C. Sum, Q. Xiong, *Nano Lett.* **2014**, *14*, 5995.

[13] H. Zhu, Y. Fu, F. Meng, X. Wu, Z. Gong, Q. Ding, M. V. Gustafsson, M. T. Trinh, S. Jin, X. Y. Zhu, *Nat. Mater.* **2015**, *14*, 636.

[14] C. C. Stoumpos, C. D. Malliakas, J. A. Peters, Z. Liu, M. Sebastian, J. Im, T. C. Chasapis, A. C. Wibowo, D. Y. Chung, A. J. Freeman, B. W. Wessels, M. G. Kanatzidis, *Cryst. Growth Des.* **2013**, *13*, 2722.

[15] Y. He, M. Petryk, Z. Liu, D. G. Chica, I. Hadar, C. Leak, W. Ke, I. Spanopoulos, W. Lin, D. Y. Chung, B. W. Wessels, Z. He, M. G. Kanatzidis, *Nat. Photonics* **2020**, DOI: 10.1038/s41566-020-00727-1.

[16] G. E. Eperon, G. M. Paternò, R. J. Sutton, A. Zampetti, A. A. Haghighirad, F. Cacialli, H. J. Snaith, *J. Mater. Chem. A* **2015**, *3*, 19688.

[17] J. Duan, Y. Zhao, B. He, Q. Tang, *Angew. Chemie - Int. Ed.* **2018**, *57*, 3787.

[18] C. Li, X. Lu, W. Ding, L. Feng, Y. Gao, Z. Guo, *Acta Crystallogr. Sect. B Struct. Sci.* **2008**, *64*, 702.

[19] G. Kieslich, S. Sun, A. K. Cheetham, *Chem. Sci.* **2015**, *6*, 3430.

[20] C. J. Bartel, C. Sutton, B. R. Goldsmith, R. Ouyang, C. B. Musgrave, L. M. Ghiringhelli, M. Scheffler, *arXiv* **2018**, 1.

[21] W. Xiang, W. Tress, *Adv. Mater.* **2019**, *31*, DOI: 10.1002/adma.201902851.

[22] L. Protesescu, S. Yakunin, M. I. Bodnarchuk, F. Krieg, R. Caputo, C. H. Hendon, R. X. Yang, A. Walsh, M. V. Kovalenko, *Nano Lett.* **2015**, *15*, 3692.

[23] G. Pan, X. Bai, D. Yang, X. Chen, P. Jing, S. Qu, L. Zhang, D. Zhou, J. Zhu, W. Xu, B. Dong, H. Song, *Nano Lett.* **2017**, *17*, 8005.

[24] G. Xiong, L. Yuan, Y. Jin, H. Wu, Z. Li, B. Qu, G. Ju, L. Chen, S. Yang, Y. Hu, *Adv. Opt. Mater.* **2020**, *8*, 2000779.

[25] L. Wang, H. Zhou, J. Hu, B. Huang, M. Sun, B. Dong, G. Zheng, Y. Huang, Y. Chen, L. Li, Z. Xu, N. Li, Z. Liu, Q. Chen, L. D. Sun, C. H. Yan, *Science (80-.).* **2019**, *363*, 265.

[26] P. N. Rudd, J. Huang, *Trends Chem.* **2019**, *1*, 394.

[27] N. Ding, D. Zhou, G. Pan, W. Xu, X. Chen, D. Li, X. Zhang, J. Zhu, Y. Ji, H. Song, *ACS Sustain. Chem. Eng.* **2019**, *7*, 8397.

[28] P. Li, Y. Duan, Y. Lu, A. Xiao, Z. Zeng, S. Xu, J. Zhang, *Nanoscale* **2020**, *12*, 6630.

[29] W. Xiang, Z. Wang, D. J. Kubicki, W. Tress, J. Luo, D. Prochowicz, S. Akin, L. Emsley, J. Zhou, G. Dietler, M. Grätzel, A. Hagfeldt, *Joule* **2019**, *3*, 205.

[30] S. Yang, H. Zhao, Y. Han, C. Duan, Z. Liu, S. (Frank) Liu, *Small* **2019**, *15*, 1904387.

[31] X. Wu, H. Li, K. Wang, X. Sun, L. Wang, *RSC Adv.* **2018**, *8*, 11095.

[32] P. Khoram, S. Brittman, W. I. Dzik, J. N. H. Reek, E. C. Garnett, *J. Phys. Chem. C* **2016**, *120*, 6475.

[33] B. Y. R. D. Shannon, M. H, N. H. Baur, O. H. Gibbs, M. Eu, V. Cu, **1976**.

[34] A. K. Jena, A. Kulkarni, Y. Sanehira, M. Ikegami, T. Miyasaka, *Chem. Mater.* **2018**, *30*, 6668.

[35] M. Kodur, R. E. Kumar, Y. Luo, D. N. Cakan, X. Li, M. Stuckelberger, D. P. Fenning, *Adv. Energy Mater.* **2020**, *10*, 1.

[36] T. Ungár, *Scr. Mater.* **2004**, *51*, 777.

[37] D. Kim, Y. H. Jin, K. W. Jeon, S. J. S. Kim, S. J. S. Kim, O. H. Han, D. K. Seo, J. C. Park, *RSC Adv.* **2015**, *5*, 74790.

[38] K. S. Kim, T. J. O'Leary, N. Winograd, *Anal. Chem.* **1973**, *45*, 2214.

[39] X. Li, Y. Luo, M. V. Holt, Z. Cai, D. P. Fenning, *Chem. Mater.* **2019**, *31*, 2778.

[40] Q. Ye, Y. Zhao, S. Mu, F. Ma, F. Gao, Z. Chu, Z. Yin, P. Gao, X. Zhang, J. You, *Adv. Mater.* **2019**, *31*, 1905143.

CHAPTER 3

INTRODUCTION

The rapid growth of the 5th generation mobile network, the internet of things (IoT), and wearable electronics have greatly promoted the demand for storage technologies featuring safety and high energy and power density.[1] Zinc-based battery chemistries are safe, have low environmental impacts and high energy densities, thus are considered one of the most ideal choices for powering wearable and IoT devices.[2] While safe primary Zn chemistries (e.g., zinc-air, zinc- silver oxide) have been commonly used in intimate wearable devices that require extreme caution(e.g. hearing aids),[3] the growing demand for advanced functionality now calls for batteries featuring rechargeability as well as higher energy and power density. A promising cathode chemistry using high-oxidation-state silver (I, III) oxide (AgO) was presented, featuring almost 2 times the specific capacity (432 mAh/g) compared to the traditional Ag_2O (231 mAh/g) cathode.[4] Utilizing this advanced cathode chemistry, printable, flexible Zn-AgO batteries have been recently reported, exhibiting low impedance (<1 Ω) for high-power discharge, high areal capacity (>50 mAh/cm^2), and good rechargeability (>500 cycles), presenting a highly attractive and practical energy storage solution for wearable and IoT devices.[4,5]

However, limitation still exists in the AgO-Zn chemistry that prevents its wide application in wearable and IoT devices. Namely, as a result of anode degradation and spontaneous cathode reduction and dissolution in alkaline electrolytes, the AgO-Zn chemistry suffers from fast self-discharge (3-15% per month) for primary cells and limited cycle life (~500 cycles at C/3) for secondary cells.[5] While the electrodes chemical and electrochemical stability can be improved by selecting compatible current collectors[5] and using additives,[6–9] the cathode

dissolution is still a remaining factor for optimizing the shelf life and cycle life of AgO-Zn batteries.

Compared to Ag_2O, the high-oxidation-state AgO contains both lower oxidation-state Ag(I) and higher oxidation state Ag(III) due to disproportionation, the latter of which is less chemically stable and prone to autonomous reduction and dissolution in its typical alkaline electrolyte environment.[10–12] While autonomous reduction can be largely mitigated by the use of additives (e.g., Pb, In, Ga, B)[13] and electrochemically stable current collectors (Au-coated Ni),[5] the dissolution of AgO leads to the permanent loss of cathode material was yet to be studied.[5] During discharge, the AgO cathode undergoes a two-step reaction where the AgO is firstly hydrolyzed by the electrolyte (**Reaction 1**) to form the intermediate $Ag(OH)_2$, followed by its electrochemical reduction into lower oxidation state Ag_2O (**Reaction 2**). However, the hydrolyzed $Ag(OH)_2$ intermediate further forms silver hydroxide complexes and lead to the undesirable loss of Ag into the electrolyte (**Reaction 3**).[12] The dissolved silver species are not recoverable once lost contact with cathode. The competition between reduction and complexation affects the rate of silver dissolution.

Hydrolysis: $$AgO\ (s) + H_2O \leftrightarrow Ag(OH)_2\ (aq) \quad (1)$$

Reduction: $$2Ag(OH)_2(aq)\ + 2e^- \leftrightarrow Ag_2O(s)\ +\ H_2O + 2OH^- \quad (2)$$

Complexation: $$Ag(OH)_2(aq) +\ xOH^- \leftrightarrow [Ag(OH)_{2+x}]^{-x}\ (aq) \quad (3)$$

Among them, the complexation takes place spontaneously both during storage and cycling, leading to the permanent loss of cathode material and negatively impacting the shelf-life of primary cells and cycle-life of secondary cells. In addition, the dissolved silver species can crossover to the anode and cause unwarranted anode degradation. As a common strategy to prevent the silver crossover, sacrificial reductive separators such as cellophane were used to

capture the dissolved silver ions.[11,14,15] However, this strategy does not mitigate silver dissolution but leads to the constant removal of dissolved Ag in the electrolyte before reaching saturation, allowing further silver dissolution from the cathode until the cellulosic material is fully oxidized. The silver dissolution, concurring with the autonomous silver reduction,[10,12] gradually discharges the battery during storage and results in irreversible capacity loss, which limits the use of the AgO-Zn battery for many applications that require extended operations.[14,16,17] Therefore it is of great importance to understand, quantify, and potentially mitigate this irreversible silver dissolution to further advance the practicality of the AgO-Zn chemistry.

In this work, we systematically studied the distribution of silver dissolution in both primary and secondary AgO-Zn cells with inductively coupled plasma mass spectroscopy (ICP-MS), identifying key factors affecting silver dissolution. To understand the fundamental mechanism of silver dissolution, the chemical states of dissolved silver species in separators and cathode surfaces were characterized with Raman spectroscopy, X-ray photoelectron spectroscopy (XPS) and X-ray absorption spectroscopy (XAS). We found that in primary cells the dissolved silver species is $[Ag(OH)_{2+x}]^{-x}$ and that the amount is influenced by the selection of electrolyte and cell configuration. Interestingly, for secondary cells, our results show that the silver dissolution is reduced at a higher cycling rate (C rate). With observations of morphological and chemical change as well as diffusion kinetics change at different C rates, the C-rate effect on silver dissolution provided a deep understanding of the silver dissolution mechanism. We believe that shifting the balance of the two-step reaction away from the undesired complexation is key to minimize the silver dissolution. Strategies in choosing proper electrolytic species/electrolyte type and coarsening cathode surface will greatly improve the shelf-life and cycle-life, and enhance the

practicality and versatility of the AgO-Zn for powering the next generation of wearable and IoT devices.

Experimental

Chemicals: Bi_2O_3, KOH (pellets, R85%), NaOH (pellet, R97%), LiOH, acetone, cellophane (gel drying frames), Poly(ethylene oxide)(PEO) (M.W. ~400 kDa) for cell fabrication, Poly(ethylene oxide) (PEO) (M_N=6,000) for XAS experiments, polyacrylamide, N,N′-Methylenebisacrylamide (MBAA), and potassium persulfate were purchased from SigmaAldrich (St. Louis, MO, USA). Zn (Grillo-WerkeAG, Germany), AgO (AmesGoldsmith, SouthGlens Falls, NY, USA), the flexbile alkaline separator (FAS), and polyethylene (PE, Solupor, Lydall Inc., Manchester, CT, USA) separator were obtained from Riot Energy LLC (Agoura Hills, CA 91301, USA). The electrode binder fluorocopolymer (GBR-6005, poly(vinylfluoride-co-2,3,3,3-tetrafluoropropylene)) was obtained from Daikin US Corporation (New York, NY, USA). tyrene-ethyl-butylene-styrene, (SEBS or G1645) was obtained from Kraton (Houston, TX, USA). Graphite powder was purchased from Acros Organics (USA). All reagents were used without further purification.

Electrode preparation: The fabrication of the Zn and AgO electrodes was adapted from previous work with minor modifications.[4] Firstly, a binder resin was prepared by dissolving 1 g fluorine rubber in 2.75 g acetone. The anode slurry was prepared by mixing 1 g Zn powder and 0.1 g Bi_2O_3 powder with 0.275 g binder resin in a planetary mixer (Flaktak SpeedmixerTM DAC 150.1 FV) at 1800 rotations per minute (rpm) for 5 min. The cathode slurry was prepared by mixing 1 g AgO powder with 0.5 g binder resin in a planetary mixer at 2250 rpm for 10 min. The

slurries were cast using film casters graduated at 1000 μm, cured at 60 °C for 30 min, and trimmed into 2 × 2 cm^2 squares for subsequent use.

Gel preparation: The synthesis of the polyacrylamide-polyethylene oxide (PAM-PEO) hydrogel was prepared by firstly dissolving 1 g of acrylamide, 0.25 g PEO (M.W. ~400 kDa), 10 mg N,N'-methylene bisacrylamide (MBAA) crosslinker, and 25 mg potassium persulfate initiator in 5 ml of deionized water as the gel precursor. The precursor was then placed into a covered glass Petri dish and heated at 90 °C for 10 min for crosslinking. The cross-linked gel was soaked in the corresponding hydroxide solution (10 M KOH or NaOH + 0.5 M LiOH) overnight and trimmed into 2× 2 cm^2 squares for subsequent use.

Cell fabrication: Primary cells were fabricated by stacking and sealing components in the following configuration: nylon, SEBS, Cu current collector (CC), Zn anode, cellophane, PAM-PEO gel, cellophane, polyethylene (PE) separator, AgO cathode, Au/Ni CC, SEBS, nylon. For each cell, both current collectors were cut into 2 × 2 cm^2 squares with 0.75 × 3 cm^2 protruding tabs allowing for electrical contact. The current collectors were then attached to the SEBS substrate by applying epoxy to the tab region. Cellophane sheets were trimmed into appropriate size and soaked in the liquid electrolyte (10M NaOH, 0.5M LiOH) along with 450 mg of Zn anode. For the anode stack, soaked Zn electrode with a layer of cellophane and 650 mg of PAM-PEO gel was added to the Cu CC atop. For the cathode stack, 0.6 g of AgO electrode was first prepared with both sides wetted by liquid electrolyte. Then, the AgO cathode was set onto the Au/Ni CC with a layer of PE and two layers of cellophane sheets stacked orderly on top of the electrode. The anode and the cathode stack were joined together as the aforementioned configuration. Next, the assembled cell was heat sealed and vacuum sealed along the CC edges.

Finally, a 2 × 2 cm^2 nylon strip was prepared and sealed onto the SEBS to complete the primary cell.

Secondary cells were fabricated based on previous work[5] by stacking and sealing components in the following configuration: Nylon, SEBS, Cu current collector (CC), Zn anode, gel electrolyte, FAS, cellophane, gel electrolyte, cellophane, polyethylene (PE) separator, AgO cathode, Au/Ni CC, SEBs Nylon. Both CC were cut into a 2 × 2 cm square with a 0.75 × 5 cm^2 protruding strip and then pasted on to a 4 × 4 cm^2 SEBS with epoxy. 0.324 g AgO cathode was placed on top of the Au/Ni CC + SEBS, and then 25 μL electrolyte was dropped at the center of the AgO sheets. PE separator, gel electrolyte and cellophane were stacked in order on top of the AgO sheets. 0.715 g Zn anode was placed on top of the Cu + SEB CC. Then gel electrolyte was placed on top of the anode strips and 10 μL electrolyte was dropped on top of the gel. Afterward, a 3 × 3 cm^2 FAS was placed on top of the gel electrolyte and vacuum sealed onto the SEBS. Once both anode and cathode components were fabricated, both parts were vacuumed sealed along the CC edges to form the secondary cell. Finally, 5 × 5 cm^2 nylon strips were sealed onto the SEBS to finish the secondary cell.

Cell cycling: The primary cells were discharged at 2 mA using Landt Instrument CT2001A. The secondary cells were charged with constant current at desired currents with voltage limit at 2 V and discharged with desired currents and voltage limit at 1.35 V using Neware battery cycling system.

Galvanostatic electrochemical impedance spectroscopy (GEIS): The GEIS was carried out in a three-electrode setup on secondary cells with additional Zn reference electrodes inserted between the anode and. The EIS was performed at galvanostatic mode with the desired background direct current (DC) bias (2, 5, 10, 25 mA) and 1 mA alternating current (AC)

perturbation, from 1 MHz to 0.1 Hz with 10 points per decade cathode using a Metrohm Autolab PGSTAT128N potentiostat. The obtained data was fitted using MATLAB zfit function. [18]

Inductively coupled plasma mass spectroscopy (ICP-MS): All the layers from the cells were soaked in concentrated 67% nitric acid overnight. The solutions obtained from soaking were diluted with water by 1000 times with 2% nitric acid for ICP-MS. The ICP-MS was conducted with a Thermo Fisher iCAP RQ. Three samples were collected for each condition.

Scanning electron microscope (SEM): The SEM was taken with a FEI Apreo with 10 KeV and 0.5 nA. The samples were rinsed with DI water and air dried before SEM.

Raman spectroscopy: Raman spectra were taken using a Renishaw Raman/microPL tool with a 532 nm excitation laser, 1200 mm grating, 10 s dwell time and 100% power.

UV-Vis spectroscopy: UV-Vis spectra were taken using Shimadzu UV 2450. Samples with silver oxide were taken against corresponding blank electrolyte as baseline.

X-ray absorption spectroscopy (XAS): XAS was carried out at APS 9-BM. Precipitants were scraped off separators from cells and diluted with polyethylene oxide powder (M_N=6000). The solids were ground with mortar and pestle and mixed using Thinky mixer at 2000 rpm for 5 min. Then solids were pressed into pellets using a hydraulic press. The energy was calibrated such that the maximum of the first derivative of the L2-edge absorption spectrum from a Pd-foil was set to 3330 eV. A Si (111) double crystal monochromator was used for the experiment. The beam was focused by a Pt/alumina coated toroidal mirror and harmonics were rejected by a flat silicon mirror. Fluorescence was collected with a four-element silicon drift detector. Three scans for each sample were taken and averaged out. Each scan was 20 minutes.

X-ray photoelectron spectroscopy (XPS): XPS samples were taken using Kratos Supra. Samples of cathodes were rinsed with DI water and dried. Separators from cells were dried

before XPS measurements. An Al anode source at 15 kV with a 10^{-8} Torr vacuum level was applied for measurement. The step size for Survey scans was 1.0 eV, followed by high-resolution scans with a step size of 0.1 eV. C 1s peak at 284.6 eV was used for calibration.

Results and Discussion

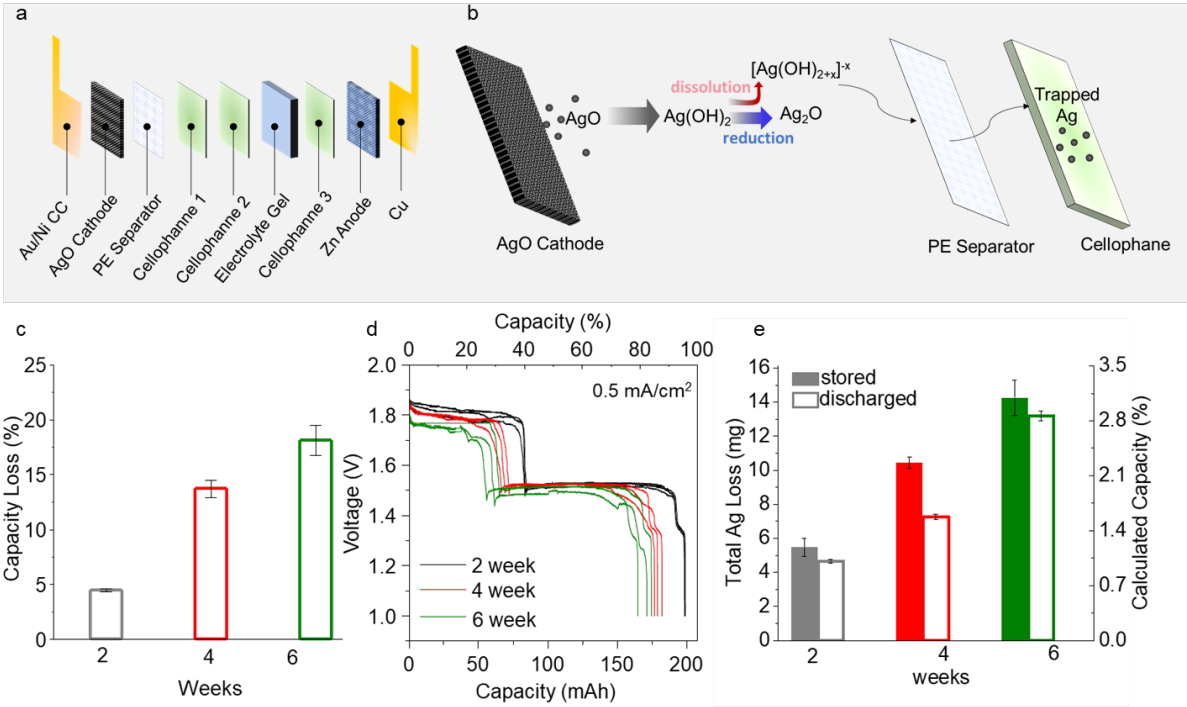

Figure 3.1. (a) Schematic of primary Zn-AgO cell. (b) Silver dissolution mechanism. (c) Capacity loss of primary cells after 2, 4 and 6 weeks at room temperature. (d) Discharge curves of cells at 2, 4 and 6 weeks. (e) Total amounts of dissolved silver in all the layers between two electrodes dissected from the primary cells stored and discharged for 2, 4 and 6 weeks. The stored cells were stored in room temperature until ICP-MS measurement, while the discharged were discharged at 0.5 mA/cm^2 before ICP-MS measurement. The right axis is the calculated capacity percentage corresponding to the amount of silver.

To block the crossover of dissolved silver species in the AgO-Zn primary cell, PE and cellophane separators were positioned between AgO cathode and Zn anode as shown in the schematic in **Figure 1a**. The PE separator is a microporous film that blocks the diffusion of large particles, and the cellophane reduces silver species to silver metal and traps them inside the films.[14] It is to be noted that even though the PE separator and cellophane block the crossover of active material, they cannot stop the reaction of the cathode with electrolyte. As illustrated in **Figure 1b**, the reaction between cathode and electrolyte during self-discharge is a two-step reaction, where the high-oxidation-state AgO reacts with water to form $Ag(OH)_2$, and then

reduce to Ag_2O or reacts with OH^- to form $[Ag(OH)_{2+x}]^{-x}$ which dissolves into electrolyte and gets lost.[11,12]

Due to the spontaneous reaction between cathode and electrolyte, the self-discharge caused a significant capacity loss. For 3 cells each stored for 2, 4, and 6 weeks at room temperature, the average capacity loss measured from discharging the cells was 4.8%, 14.8%, and 18.5% respectively as shown in **Figure 1c**. The corresponding discharge curves in **Figure 1d** showed similar shapes except for more capacity loss for cells stored for more weeks. To quantify the dissolved silver, we measured the silver amount within the separators between two electrodes in the cell using ICP-MS. We stored two sets of cells with and without discharge at the end of storage for 2, 4, and 6 weeks. The discharged cells were discharged for five days before the end of storage time. **Figure 1e** shows that the amount of dissolved silver and corresponding capacity percentage increase for both stored cells and discharged cells at 2, 4, and 6 weeks. The more silver dissolution in stored cells could be attributed to the facts that they stayed longer at higher oxidation state or that the complexation was reversed on the cathode surface in the discharged cells. The calculated percentages of capacity loss based on amounts of dissolved silver are shown on the right axis in **Figure 1e**. Comparing the capacity percentages calculated from the amount of dissolved silver against the ones from discharge curves, silver dissolution took a non-negligible part in self-discharge and increased over 6 weeks. With loss of 2.2% of cathode active material per month, even though the rest of the self-discharge caused by self-discharge can be recovered,[5,19] the cell would lose an unrecoverable 26.4% capacity in a year solely from silver dissolution. This percentage of capacity loss weakens the competitiveness of AgO-Zn batteries against common primary cells at 1% self-discharge per year.[20] Thus, silver dissolution is a major issue to be investigated and mitigated for a longer shelf life of primary cells.

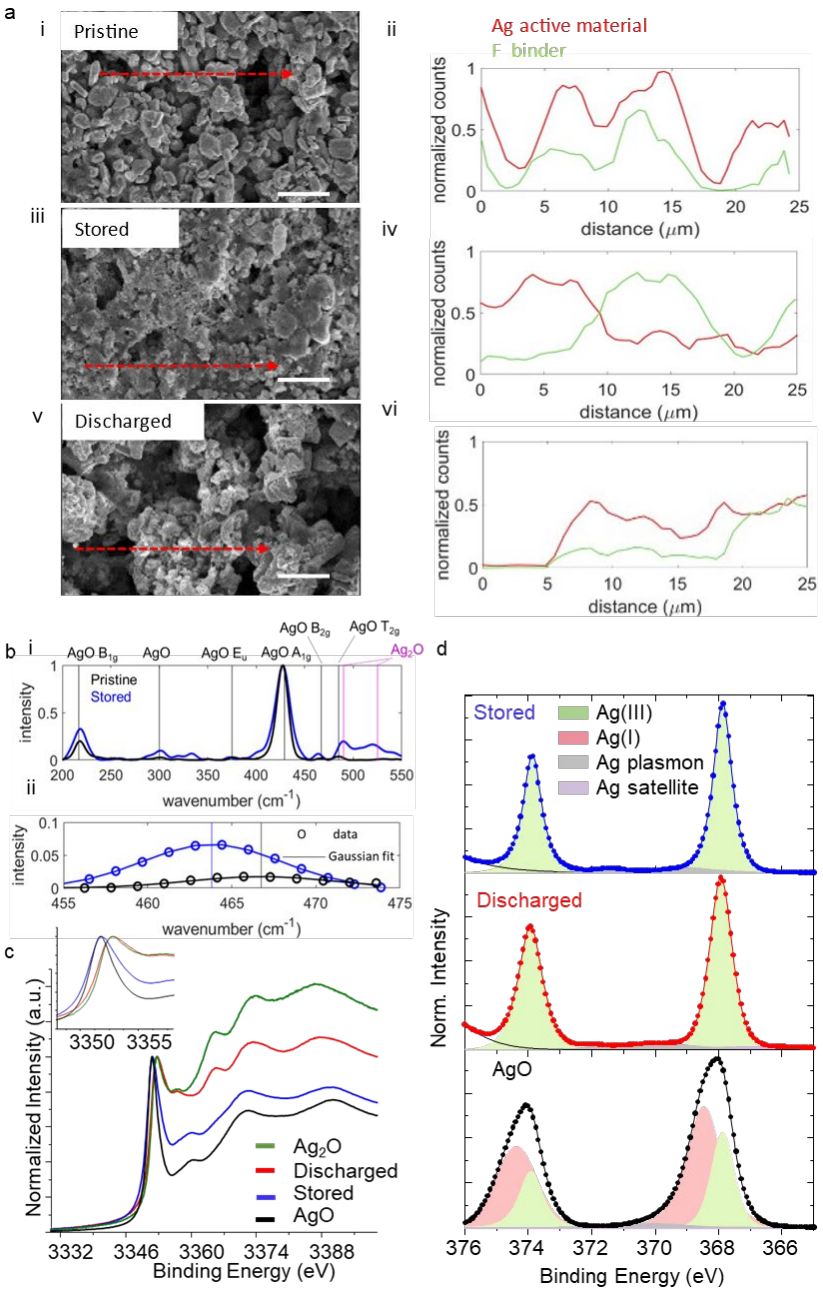

Figure 3.2. (a) SEM images of cathode surface in pristine state (i), stored for 2 weeks (iii) and discharged after 12 days of storage at room temperature (v); EDS line profiles of Ag and F signals across the pristine (ii), stored (iv) and discharged (vi) cathode as shown by the red-dot line in the SEM images. Scale bar, 5μm. (b) (i) Raman spectra of pristine cathode and cathode from a primary cell that stored at full capacity for 2 weeks at room temperature. (ii) Gaussian fit of peaks around 467 cm^{-1}. (c) XAS spectra of PE separators from cells that were discharged to first plateau after storing for 2 weeks and stored for 2 weeks at full capacity, powder of Ag_2O and AgO. Inset figure is zoomed-in view around the pre-edge peaks. (d) XPS spectra of AgO powder (black), PE separator of Zn-AgO cells stored for 2 weeks (blue) and discharged after 12 days of storage at room temperature. The dots are raw data, and the solid lines are fitted results. The areas under the curves are fitting components of Ag(I), Ag(III), Ag plasmon and Ag satellite.

The silver dissolution mechanism was revealed by observing morphological change and chemical environment after storage and discharge. As shown in pictures of dissembled layers in **Figure S1**, the PE separator and first two layers of the cellophane turned black after storage because silver dissolved into the electrolyte and was trapped in the PE separator and cellophane. The cathode surface also went through morphological changes after reacting with the electrolyte. As shown in scanning electron microscopy (SEM) in **Figure 2a(i, iii and v)**, the surface of the pristine cathode was composed of smooth, uniform particles whereas the cathode from stored and discharged cells showed roughened surfaces. The elemental distribution acquired from energy dispersive spectroscopy (EDS) in **Figure 2a** uncovers the change: the pristine cathode has AgO particles bond with fluorine-containing GBR binder in **Figure 2a(ii)**; in the stored cell (**Figure 2a(iii and iv)**), the surface of the cathode is coarsened, and the Ag-containing active material is separated from the fluorine-containing binder; in the discharged cell as shown in **Figure 2a (v and vi)**, the surface is predominant with bigger sizes of pores while the signal of Ag and F do not trace with each other completely. The surface coarsening and separation between active material and binder are caused by the dissolution of AgO.

From the perspective of the chemical environment, the cathode undergoes a series of changes during storage or discharge. In **Figure 2b(i),** the Raman spectra show that the profile of the pristine surface completely matches that of AgO while the stored cathode surface matches that of the reduced Ag_2O.[21] The peak around 467 cm^{-1} of the stored cathode in **Figure 2b(ii),** corresponding to the B_{2g} mode of AgO, shifted to a lower wavenumber than the pristine cathode, suggesting the formation of $[Ag(OH)_{2+x}]^{-x}$ complexes since OH^- ligands with shielding effect shortens the bonds in B_{2g} mode. Together, the observation of color change in different layers,

and cathode morphological and chemical change are evidence of the mechanism proposed in **Figure 1b**.

After leaving the cathode surface, the dissolved silver species from the cathodes will also travel through the PE separators and be reduced to Ag in cellophane.[14] Since the PE separator acts as a microporous layer with no reactions with active materials, analyzing the silver species on the PE separators can help identify the dissolved silver species, which further reveals the silver dissolution mechanism. The X-ray Absorption Spectroscopy (XAS) in **Figure 2c** compares the oxidation state of the PE separator in a cell stored for two weeks versus a cell partially discharged to lower voltage matching Ag_2O as shown in **Figure S2**. Reference standards of AgO and Ag_2O were also measured for comparison. The XAS spectra of the separator from a stored cell showed that dissolved silver species after two-week storage still have the same oxidation state as AgO with an absorption edge close to 3365 eV.[22,23] However, the pre-edge of the separator is broader than the reference standard AgO, and the relative intensity of the features of the separator in the range of 3350-3400 eV is different from AgO as well. Both differences suggest the formation of a ligand bond to the Ag atom.[24] Combining the oxidation state extracted from XAS and chemical environment change observed in Raman spectra, the complex is $[Ag(OH)_{2+x}]^{-x}$.[21] For the separator from the partially-discharged cell, the oxidation state is the same as Ag_2O, which is possibly $[Ag_3O(OH)_2]^-$ according to literatures.[11,25] XPS was also used to examine the chemical state of the surface of separators as shown in **Figure 2d**. The side of the PE separator facing the cellophane was measured to make sure only the dissolved silver species were detected. The references standard AgO powder has two peaks of Ag 3d 3/2 at 374.5 eV and 3d 5/2 at 368.0 eV, which each compose of Ag(I) and Ag(III) peaks.[26–28] Since XPS measured the silver species on the surface of the PE separator on the side touching the cellophane, only

Ag(III) was detected for separators from both stored and discharged cells in XPS since Ag(I) is more easily reduced to Ag metal than Ag(III).[29] The chemical analysis of XAS, Raman and XPS together confirms the formation of $[Ag(OH)_{2+x}]^{-x}$ during cathode dissolution.

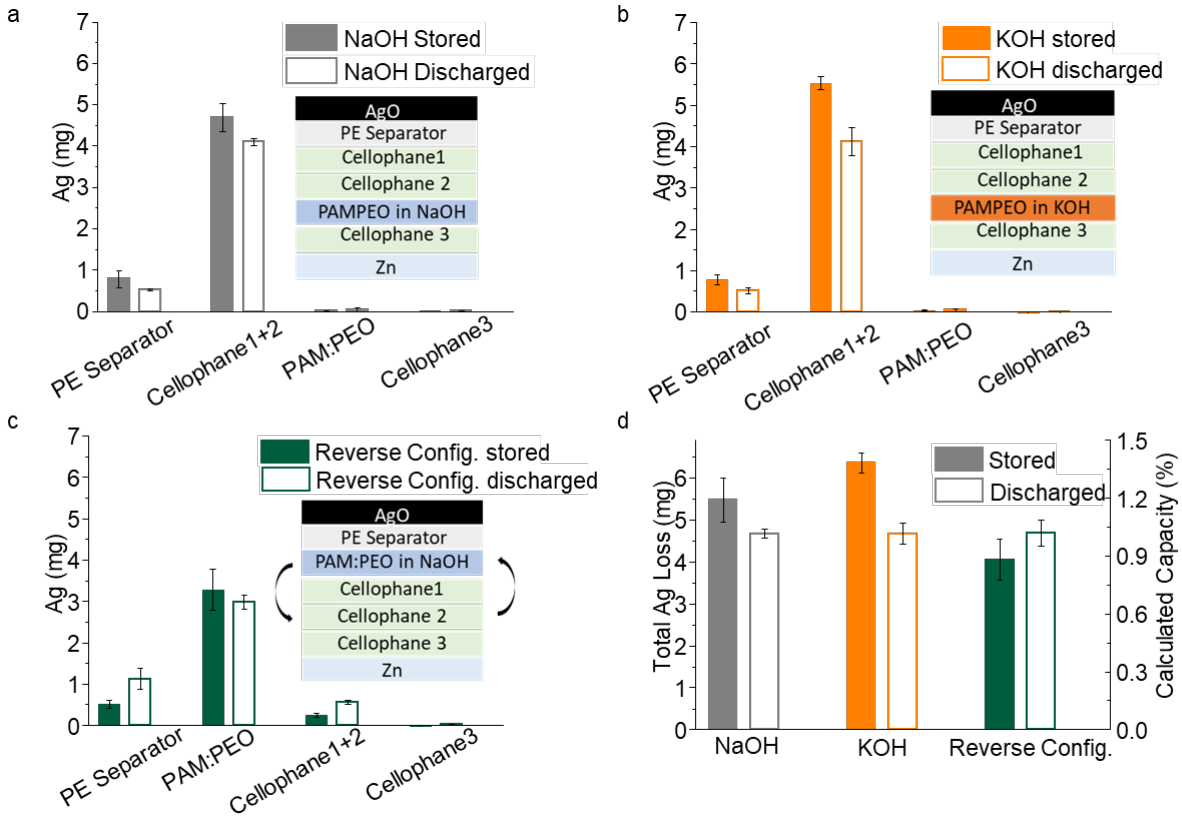

Figure 3.3. (a) Ag amount in each layer from NaOH primary cells stored and discharged in two weeks at room temperature. The schematic details the primary cell configuration (b) Ag amounts in KOH primary cells. (c) Ag amounts in reverse configuration in which the PAM:PEO moves closer to the cathode. (d) Total amounts of Ag in the all layers in each case in (a, b and c).

Besides understanding the mechanism of silver dissolution in primary AgO-Zn cells, we observed the distribution of dissolved silver in each layer of the cell regarding different electrolytes and cell configurations. For regular configuration as shown in **Figure 3a**, the stored cells have more dissolution than discharged cells because the cathodes in stored cells were at higher oxidation state AgO ($Ag_2(I, III)O_2$) over 14 days, which is more prone to silver dissolution. To compare KOH against NaOH, the amount of silver in each individual layer was

quantified by ICP-MS, which showed that most dissolved silver was trapped in the PE separator and the first two layers of cellophane (**Figure 3a-b)**. Compared with NaOH cells, KOH caused more silver dissolution, given that KOH is a stronger base to facilitate the complexation of $Ag(OH)_2$ to $[Ag(OH)_{2+x}]^{-x}$.[30] The other possible factor is the restricted water accessibility: the K^+, compared with Na^+, is associated with fewer water molecules due to the shielding effect and allows better water accessibility for the silver species. The water accessibility effect was further tested with soaking cathodes in different concentrations and combination of KOH and NaOH (**Figure S3**). The peak around 280 nm in UV-Vis spectra is reported to be Ag nanoparticles as shown in **Figure S3a**, which is used as an indicator of silver dissolution.[31] We found that the silver dissolution increases with the electrolyte concentration until 8 M, and then decreases at higher concentrations. At each concentration, KOH has the highest amount of silver dissolution while NaOH has the lowest, which confirmed the ICP-MS results. The self-discharge of cells in different electrolyte were consistent with the trend as shown in **Figure S4 and S5**. Compared with 8 M electrolytes, 10 M electrolyte has less silver dissolution and self-discharge due to the limited water accessibility at high concentration. This observation suggests either using weaker bases as electrolytes or limiting the water accessibility to reduce silver dissolution. It is worth noting that when selecting lower electrolyte concentrations or weaker bases, the stability of the Zn anode can be negatively affected.[9] When choosing electrolyte and deciding electrolyte concentration, we need to consider the tradeoff among electrolyte conductivity, reactivity with cathode and self-discharge.[4]

Apart from electrolyte, the cell configuration also affects the silver dissolution. By moving the cellophane away from and PAM:PEO gel closer to the cathode, most of dissolved silver was found in PAM:PEO instead of cellophanes (**Figure 3c**). Since there is abundant

electrolyte in the PAM:PEO gel, the proximity to the PAM:PEO gel was able to facilitate the reduction of $Ag(OH)_2$ to Ag_2O and thus hinder the complexation of $Ag(OH)_2$, resulting in more self-discharge in this cell configuration as shown in **Figure S5** and less silver dissolution in **Figure 3d**. Thus, to reduce cathode dissolution and reduction simultaneously for long-term storage of primary cells, the key is to limit the generation of $Ag(OH)_2$ intermediates, which could be addressed with strategies such as limiting the free water accessibility by optimizing polymer composition or additives within the gel, which is similar to restrict water accessibility for Zn anodes.[9]

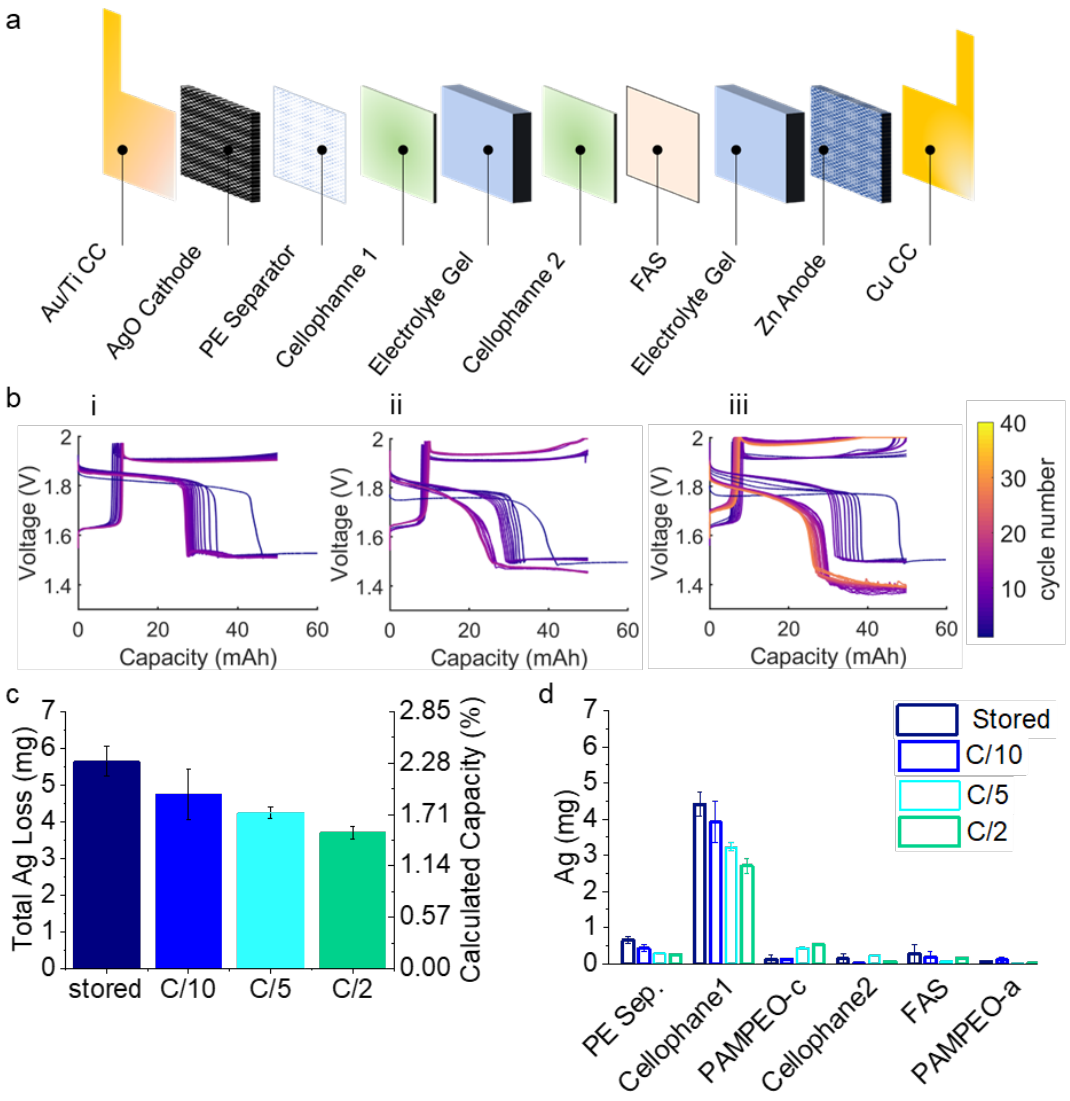

Figure 3.4. (a) schematic of secondary Zn-AgO cell. (b) Capacity-voltage curves of PAM:PEO cells cycled at C/10, C/5 and C/2 for two weeks. (c) total amount of dissolved Ag and corresponding capacity loss of secondary PAM:PEO cells stored, stored, cycled at C/10, C/5 and C/2 for two weeks. (d) Ag amounts in each layer in PAM:PEO cells.

Similarly, silver dissolution is of great concern for secondary cells due to the irreversible loss of cathode material which eventually reduces the cell stability and capacity retention. Here we test the secondary cells with the same PAM:PEO gel and different cell configuration as shown in **Figure 4a**. The cell geometry of secondary is different from primary with the use of KOH as electrolyte as well as the addition of FAS to further stop the traveling of Zn and Ag across to the other electrode. The effect of C rate on silver dissolution was examined by cycling

the cells at different rates over 14 days. The typical capacity-voltage curves of each rate (n = 3) are shown in **Figure 4b**. For rates higher than C/10, the cells were cycled at C/10 for 10 cycles to complete the formation of cells first and then cycled at the desired rates. The cycling for all the cells was stopped right after the charging cycle to restore the cells to the charged state for comparison. The stored secondary cells have the highest amount of silver dissolution due to that the cathodes stayed at the high oxidation state of AgO throughout the 14 days, which is consistent with the observation of primary cells. The cells cycled at a higher C rate show less silver dissolution as shown in **Figure 4c**. Looking at the distribution of dissolved silver, we see that the dissolved silver is mainly in PE separator, cellophane and gel, blocked by FAS to travel further into the anode side as shown in **Figure 4d**.

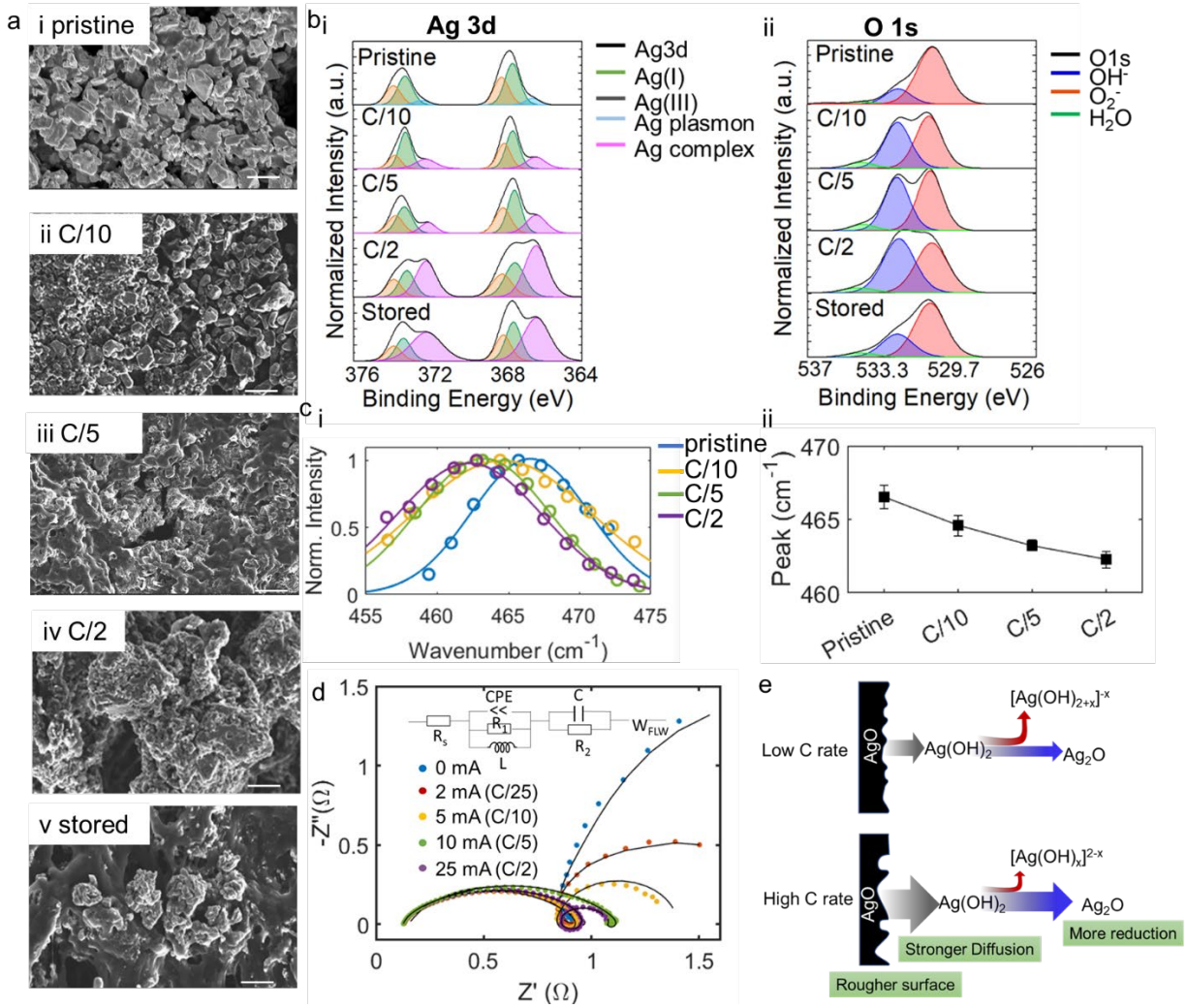

Figure 3.5. (a) SEM images if cathode from secondary Zn-AgO cells that are pristine(i), cycled at C/10 (ii), C/5 (iii), C/2 (iv) and stored over two weeks. Scale bar, 5µm. (v). (b) Ag3d (i) and O1s (ii) spectra of cathodes from pristine, cycled at C/10, C/5, C/2 and stored cells. (c) (i) Raman spectra of AgO B_{2g} peak around 467 cm^{-1} of pristine cathode and cathodes cycled at C/10, C/5 and C/2. Dots are raw data, and lines are Gaussian fit. (ii) Fitted peaks and their confidence intervals at 95% of cathodes. (d) (i) GEIS of three-electrode Zn-AgO cell at 0, -2, -5, -10 and -25 mA with AgO cathode as working electrode, Zn anode as counter electrode and Zn strip as a reference electrode to observe the cathode. The inlet is the circuit (e) Schematic of C-rate effect on silver dissolution.

By closely examining the cathode-electrolyte interface, the C-rate effect on silver dissolution can be understood from perspectives of morphology, surface chemistry and diffusion kinetics, which are inherently determined by the two-step reaction. Cathodes were taken out from cells for characterization after charged Morphologically, the cathode surface became

coarser with higher C rate. The granular shapes of AgO in the pristine cathode became rougher, and large pores around 10 μm appeared in the cell cycled at C/2 as shown in **Figure 5a**, which was caused by higher current density changing the cathode surface more drastically. At high C rate, this coarse surface exposed more surface area, where the $Ag(OH)_2$ reduces to Ag_2O more easily. As for the stored cell, the silver dissolution slowly etched away the cathode material from the electrode, exposing more binders to the surface.

XPS was applied to pristine, cycled and stored cathodes. In Ag 3d spectra as shown in **Figure 5b(i)**, with the Ag(I), Ag(III) and Ag plasmon peak in the pristine cathodes. The cycled and stored cathodes all have a different peak at 372.4 eV, which confirms the formation of Ag complex on the cathode surface due to the silver dissolution.[32] The intensity of the Ag complex peak increases with C rate as shown by ratios of peak areas between Ag(I, III) and Ag complex in **Figure S6a**, indicating more complex formation on the surface at higher C rate. In O 1s spectra (**Figure 5b(ii)**), the peaks are ascribed to OH^-, O_2^- and H_2O.[28] At higher C rates, more OH^- peak around 532.5 eV was detected (**Figure S6b**) suggesting more formation of silver hydroxide complex. Similarly, in Raman spectra in **Figure 5c**, given that the peak shift of AgO B_{2g} peak at 467 cm^{-1} is due to the formation of $[Ag(OH)_{2+x}]^{-x}$, the further shift to lower wavenumber at higher C rates demonstrates longer bonds formation, suggesting more formation of $[Ag(OH)_{2+x}]^{-x}$. The full spectra can be found in **Figure S7**. Even though there is more formation of $[Ag(OH)_{2+x}]^{-x}$ on the cathode surface at higher C rate, the amounts of dissolved silver in other layers of the cell measured by ICP-MS (**Figure 4c**) showed that there is less silver dissolution, which could be understood from diffusion kinetics.

Diffusion kinetics measured through EIS confirms the two-step reaction and explains the C-rate effect during discharge. A phenomenon that can be observed in the two-step reaction is

that the voltage increases initially and then drop when applied with a constant current,[33] which was observed in the Zn-AgO three-electrode cell. **Figure S8** shows the chronoamperometry of a pouch cell in a three-electrode setup to observe the electrochemical reaction on the cathode. Under higher C-rate or higher discharging currents, the voltage response has an initial increase and then decrease before becoming stable, which supports the two-step reaction for reduction of AgO to Ag_2O. In galvanostatic electrochemical impedance spectroscopy (GEIS), the three-electrode cell were measured at different DC current of 0, -2, -5, -10 and -25 mA, which corresponding to 0, C/25, C/10, C/5 and C/2. The curves of cathode vs. reference electrode appear to be a semicircle at high frequency, followed by a negative inductive loop before the low-frequency diffusion tail. The negative loop is associated with the two-step reaction,[33] which composes of negative R_2 and C as shown in the **Figure 5d**. The increased series resistance is consistent (**Figure S9**) with the observation of rougher surface under SEM. As the discharging current increases, the negative loop shrinks in size, suggesting the fast consumption of the intermediate species. The diffusion time constant τ_{FLW} of finite length Warburg decreases with higher current as shown in **Figure S9**. The stronger diffusion at a higher current will favor the reduction of the intermediate phase $Ag(OH)_2$ to Ag_2O.[17] As shown in **Figure 5e,** at higher cycling rate, the cathode surface is rougher which results in more generation of the intermediate phase. The rougher surface and stronger diffusion together quickly consumes intermediate $Ag(OH)_2$, slowing down the competing complexation reaction. In the meantime, at higher C rate, the generated silver hydroxide complex is more localized at cathode surface because of the rougher surface and limited diffusion,[17] resulting in less silver dissolution into other layers of the cells. This observation suggests that future remedies such as modifying the cathode surface such

as coarsening the AgO particles may help enhance the reduction and hinder the dissolution in secondary cells.

Conclusion

In this study, we investigated the mechanism of silver dissolution in AgO-Zn battery and the factors that affect it. With evidence from chemical analysis on the cathode surfaces and dissolved silver species, the mechanism of silver dissolution is shown to follow a two-step reaction with intermediate phase $Ag(OH)_2$ as a product of AgO reacting with water, which either dissolves into electrolyte as $[Ag(OH)_{2+x}]^{-x}$ or reduces to Ag_2O. To mitigate silver dissolution, the key is to reduce the formation of intermediate $Ag(OH)_2$ and quickly consume the intermediate to avoid its further complexation. To reduce self-discharge and prolong shelf life of primary cells, strategies of using weaker bases as electrolytes or restricting water accessibility should be adopted. Optimization of concentration of alkaline in the electrolytes should be conducted with consideration of tradeoffs including conductivity of the electrolytes.[4] To promote the reduction of AgO to Ag_2O against silver dissolution, the cathode surface can be coarsened. Further studies on optimizing the cathode surface and searching for ideal electrolytes should be explored.

Acknowledgements

Chapter 3, in part is currently being prepared for submission for publication of the material. Quinn, Xueying; Yin, Lu; Li, Weikang; Li, Mingqian; Wicker, Connor; Liu, Ruixiao; Dang, Bryant; Ortega, Jeff; Wang, Joseph; Meng, Ying Shirley. The dissertation author was the primary researcher and author of this material.

The authors thank Dr. Neal Arakawa for calibrating ICP-MS, Dr. George Sterbinsky for discussing sample preparation and measuring samples for XAS, Dr. Long Nguyen and Dr. Kun Qian for discussing XAS analysis. This research was supported by Riot Energy and Qualcomm.

This research used resources of the Advanced Photon Source, a U.S. Department of Energy (DOE) Office of Science user facility operated for the DOE Office of Science by Argonne National Laboratory under Contract No. DE-AC02-06CH11357. The authors acknowledge the use of facilities and instrumentation at the UC Irvine Materials Research Institute (IMRI), which is supported in part by the National Science Foundation through the UC Irvine Materials Research Science and Engineering Center (DMR-2011967), Specifically, the XPS work was performed using instrumentation funded in part by the National Science Foundation Major Research Instrumentation Program under grant No. CHE-1338173.

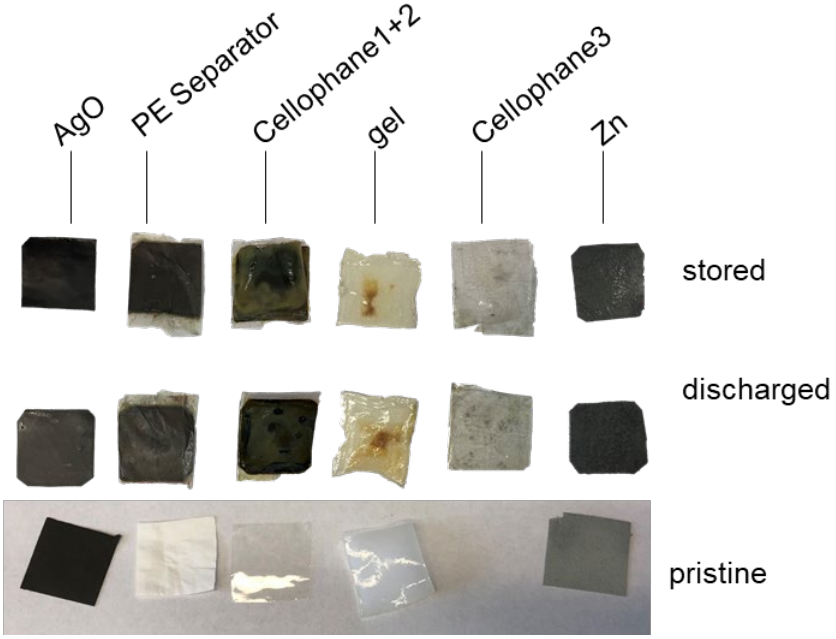

Figure 3.S1. pictures of each layer in pristine state, stored and discharged primary cells. (b) (i) Raman spectra of pristine cathode and cathode from a primary cell that stored at full capacity for 2 weeks.

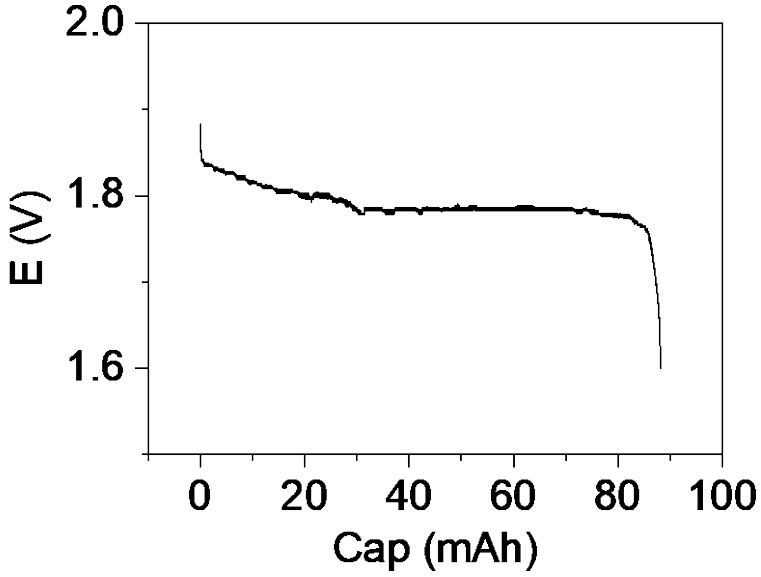

Figure 3.S2. Discharge curve of a cell discharged to lower plateau for XAS.

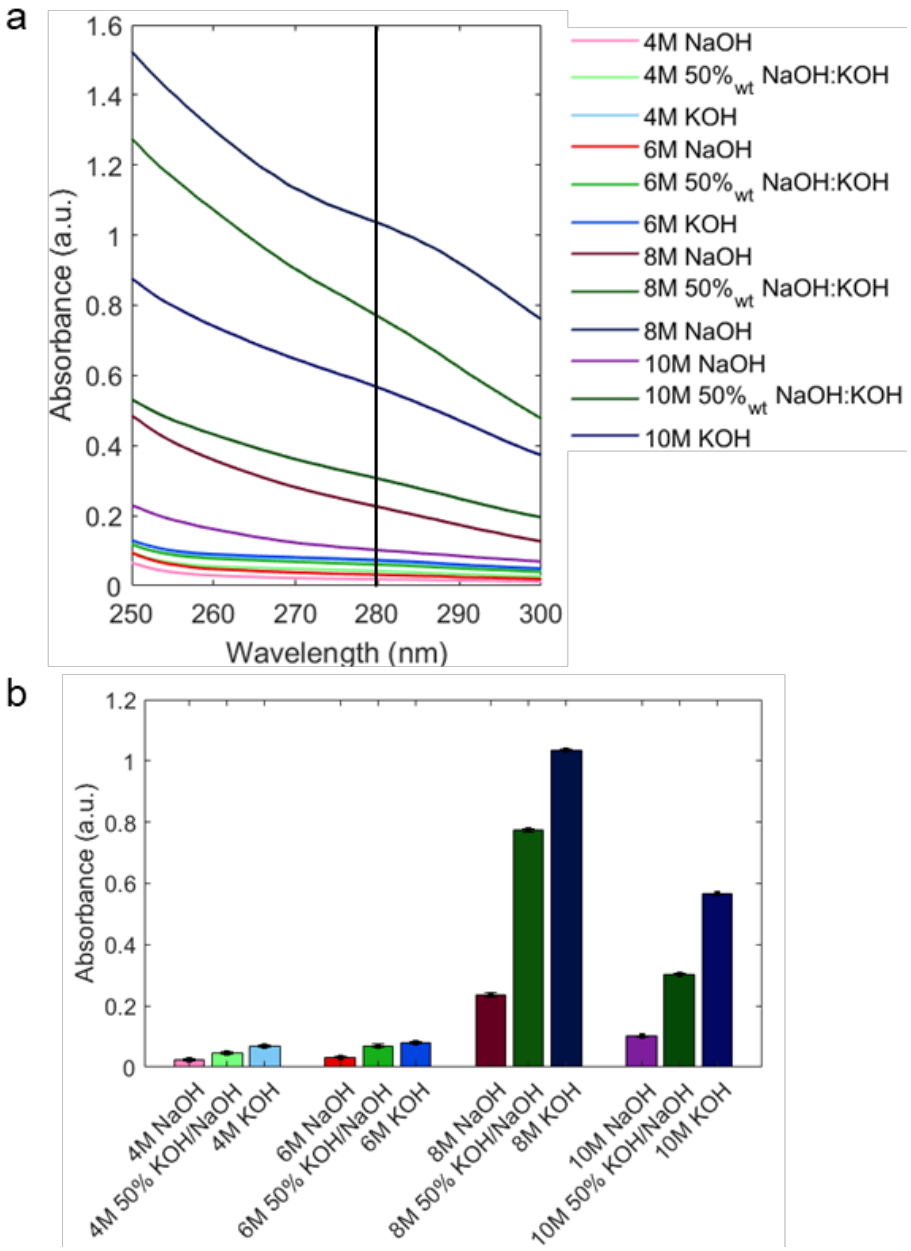

Figure 3.S3. (a) UV-Vis spectra of electrolytes after soaking with AgO cathodes for one week. Vertical line around 280 nm. (b) Average absorption at 280 nm of each electrolyte, corresponding to the wavelength at which Ag NPs are detected.

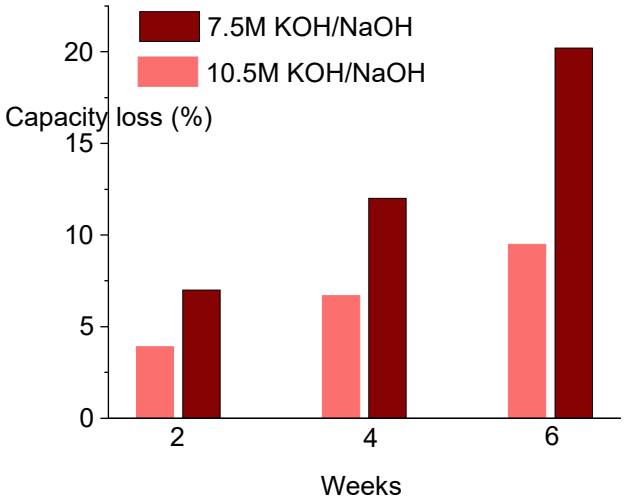

Figure 3.S4. Capacity loss of primary cells with different concentrations of 50%wt KOH/NaOH electrolytes in 2, 4 and 6 weeks.

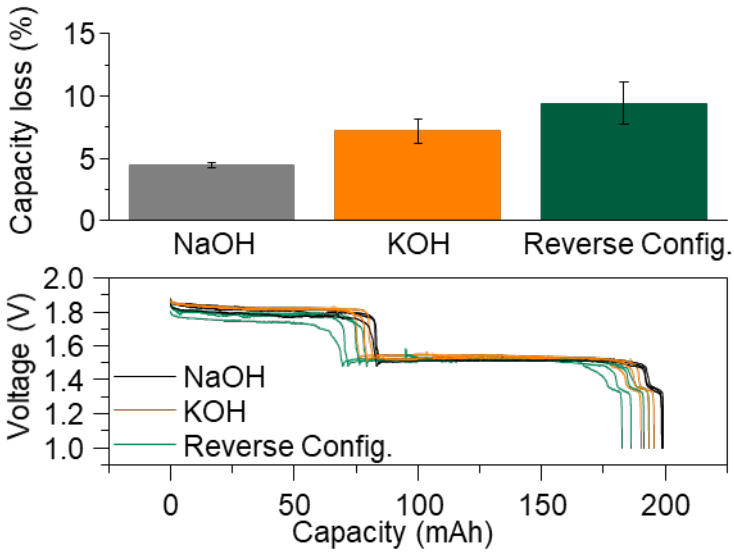

Figure 3.S5. Capacity loss and discharge curves of cells in figure 3.

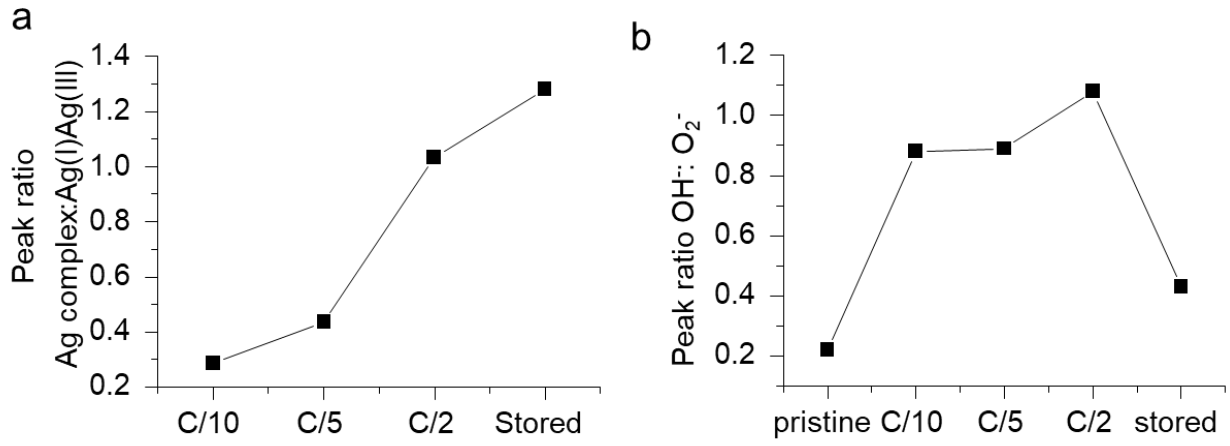

Figure 3.S6. (a) Ratios of peak areas between Ag complex and sum of Ag(I) and Ag(III) in cathodes from cells that were cycled and stored. (b) Ratios of peak areas between OH^- and O_2^- in cathodes from cells that were cycled and stored.

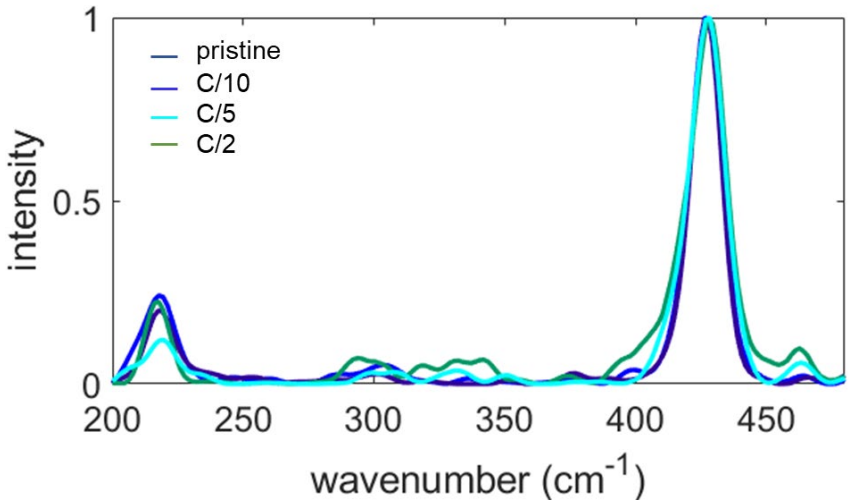

Figure 3.S7. Full spectra of pristine cathode and cycled cathodes at C/10, C/5 and C/2.

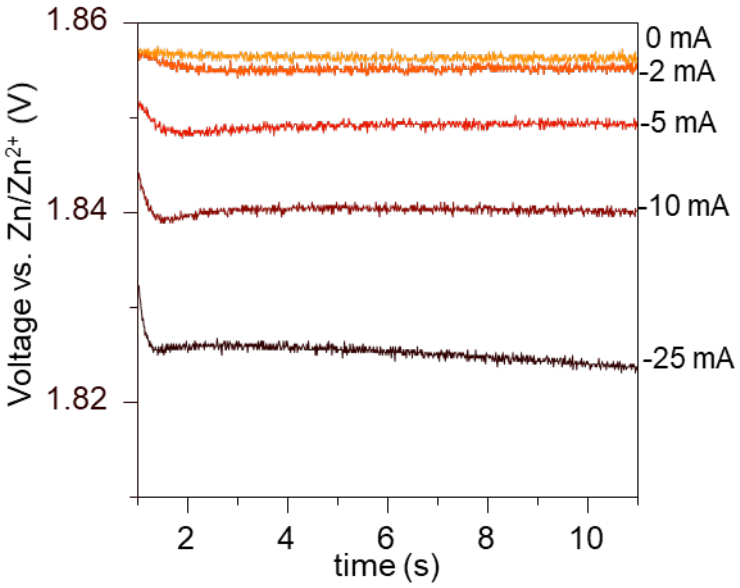

Figure 3.S8. Voltages as a function of time at constant currents of a three-electrode cell with AgO cathode as working electrode, Zn anode as counter electrode, and Zn metal as counter in 10 M KOH and 0.5M LiOH.

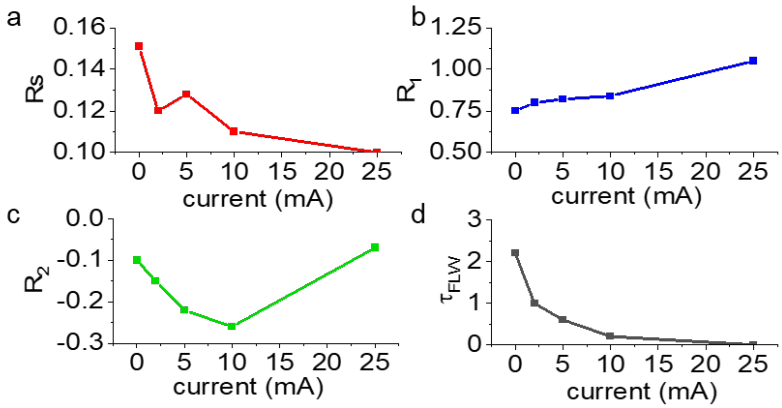

Figure 3.S9. The fitted parameters of different currents are shown in (a) R_s, (b) R_1, (c) R_2, and (d) τ_{FLW}.

REFERENCES

(1) *Wearable Technology Market Size Analysis Report 2028*. https://www.grandviewresearch.com/industry-analysis/wearable-technology-market (accessed 2022-01-23).

(2) Song, W.-J.; Lee, S.; Song, G.; Park, S. Stretchable Aqueous Batteries: Progress and Prospects. *ACS Energy Lett.* **2019**, *4* (1), 177–186. https://doi.org/10.1021/acsenergylett.8b02053.

(3) Root, M. J. Medical Device Batteries. In *Batteries for Sustainability: Selected Entries from the Encyclopedia of Sustainability Science and Technology*; Brodd, R. J., Ed.; Springer: New York, NY, 2013; pp 359–392. https://doi.org/10.1007/978-1-4614-5791-6_11.

(4) Yin, L.; Scharf, J.; Ma, J.; Doux, J.-M.; Redquest, C.; Le, V. L.; Yin, Y.; Ortega, J.; Wei, X.; Wang, J.; Meng, Y. S. High Performance Printed AgO-Zn Rechargeable Battery for Flexible Electronics. *Joule* **2021**, *5* (1), 228–248. https://doi.org/10.1016/j.joule.2020.11.008.

(5) Scharf, J.; Yin, L.; Redquest, C.; Liu, R.; Quinn, X. L.; Ortega, J.; Wei, X.; Wang, J.; Doux, J.-M.; Meng, Y. S. Investigating Degradation Modes in Zn-AgO Aqueous Batteries with In Situ X-Ray Micro Computed Tomography. *Advanced Energy Materials* **2021**, *11* (33), 2101327. https://doi.org/10.1002/aenm.202101327.

(6) Shin, J.; You, J.-M.; Lee, J. Z.; Kumar, R.; Yin, L.; Wang, J.; Shirley Meng, Y. Deposition of ZnO on Bismuth Species towards a Rechargeable Zn-Based Aqueous Battery. *Phys. Chem. Chem. Phys.* **2016**, *18* (38), 26376–26382. https://doi.org/10.1039/C6CP04566A.

(7) Mitha, A.; Yazdi, A. Z.; Ahmed, M.; Chen, P. Surface Adsorption of Polyethylene Glycol to Suppress Dendrite Formation on Zinc Anodes in Rechargeable Aqueous Batteries. *ChemElectroChem* **2018**, *5* (17), 2409–2418. https://doi.org/10.1002/celc.201800572.

(8) Yadav, G. G.; CHO, J.; Wei, X.; Nyce, M.; Banerjee, S. Zinc Electrodes with High Capacity Utilizations. US20200411846A1, December 31, 2020.

(9) Mainar, A. R.; Leonet, O.; Bengoechea, M.; Boyano, I.; Meatza, I. de; Kvasha, A.; Guerfi, A.; Blázquez, J. A. Alkaline Aqueous Electrolytes for Secondary Zinc–Air Batteries: An Overview. *International Journal of Energy Research* **2016**, *40* (8), 1032–1049. https://doi.org/10.1002/er.3499.

(10) Tudela, D. Silver(II) Oxide or Silver(I,III) Oxide? *J. Chem. Educ.* **2008**, *85* (6), 863. https://doi.org/10.1021/ed085p863.

(11) Amlie, R. F.; Rüetschi, P. Solubility and Stability of Silver Oxides in Alkaline Electrolytes. *J. Electrochem. Soc.* **1961**, *108* (9), 813. https://doi.org/10.1149/1.2428228.

(12) Dirkse, T. P.; Wiers, B. The Stability and Solubility of AgO in Alkaline Solutions. *J. Electrochem. Soc.* **1959**, *106* (4), 284. https://doi.org/10.1149/1.2427331.

(13) Adamson, G. W.; Zhou, H. Cathode. US9209454B2, December 8, 2015.

(14) *Zinc-Silver Oxide Batteries*; Fleischer, A., Lander, J. J., Electrochemical Society, Air Force Aero Propulsion Laboratory, Eds.; The Electrochemical Society series; J. Wiley: New York, 1971.

(15) Andre, H. G. Zinc-Silver Accumulator. US2594710A, April 29, 1952.

(16) Zamarayeva, A. M.; Gaikwad, A. M.; Deckman, I.; Wang, M.; Khau, B.; Steingart, D. A.; Arias, A. C. Fabrication of a High-Performance Flexible Silver–Zinc Wire Battery. *Advanced Electronic Materials* **2016**, *2* (5), 1500296. https://doi.org/10.1002/aelm.201500296.

(17) Randin, J.-P. Determination of State-of-Discharge of Zinc-Silver Oxide Button Cells. III. In Situ Impedance Measurements of Each Electrode. *Journal of Applied Electrochemistry* **1985**, *15* (4), 591–601. https://doi.org/10.1007/bf01059301.

(18) Dellis, J.-L. *Zfit*. MATLAB Central File Exchange. https://www.mathworks.com/matlabcentral/fileexchange/19460-zfit (accessed 2022-01-31).

(19) Fu, J.; Cano, Z. P.; Park, M. G.; Yu, A.; Fowler, M.; Chen, Z. Electrically Rechargeable Zinc–Air Batteries: Progress, Challenges, and Perspectives. *Advanced Materials* **2017**, *29* (7), 1604685. https://doi.org/10.1002/adma.201604685.

(20) *Renata SA: Home*. https://www.renata.com/ (accessed 2021-06-27).

(21) Waterhouse, G. I. N.; Bowmaker, G. A.; Metson, J. B. The Thermal Decomposition of Silver (I, III) Oxide: A Combined XRD, FT-IR and Raman Spectroscopic Study. *Phys. Chem. Chem. Phys.* **2001**, *3* (17), 3838–3845. https://doi.org/10.1039/b103226g.

(22) Behrens, P.; Aßmann, S.; Bilow, U.; Linke, C.; Jansen, M. Electronic Structure of Silver Oxides Investigated by AgL XANES Spectroscopy. *Zeitschrift für anorganische und allgemeine Chemie* **1999**, *625* (1), 111–116. https://doi.org/10.1002/(SICI)1521-3749(199901)625:1<111::AID-ZAAC111>3.0.CO;2-7.

(23) Kolobov, A. V.; Rogalev, A.; Wilhelm, F.; Jaouen, N.; Shima, T.; Tominaga, J. Thermal Decomposition of a Thin AgOx Layer Generating Optical Near-Field. *Appl. Phys. Lett.* **2004**, *84* (10), 1641–1643. https://doi.org/10.1063/1.1667003.

(24) Kirshenbaum, K.; Bock, D. C.; Lee, C.-Y.; Zhong, Z.; Takeuchi, K. J.; Marschilok, A. C.; Takeuchi, E. S. In Situ Visualization of Li/Ag2VP2O8 Batteries Revealing Rate-Dependent Discharge Mechanism. *Science* **2015**, *347* (6218), 149–154. https://doi.org/10.1126/science.1257289.

(25) Miller, B. Rotating Ring-Disk Study of the Silver Electrode in Alkaline Solution. *J. Electrochem. Soc.* **1970**, *117* (4), 491. https://doi.org/10.1149/1.2407548.

(26) Kaspar, T. C.; Droubay, T.; Chambers, S. A.; Bagus, P. S. Spectroscopic Evidence for Ag(III) in Highly Oxidized Silver Films by X-Ray Photoelectron Spectroscopy. *J. Phys. Chem. C* **2010**, *114* (49), 21562–21571. https://doi.org/10.1021/jp107914e.

(27) Hoflund, G. B.; Hazos, Z. F.; Salaita, G. N. Surface Characterization Study of Ag, AgO, and Ag 2 O Using x-Ray Photoelectron Spectroscopy and Electron Energy-Loss Spectroscopy. *Phys. Rev. B* **2000**, *62* (16), 11126–11133. https://doi.org/10.1103/PhysRevB.62.11126.

(28) Lützenkirchen-Hecht, D. Anodic Silver Oxide (AgO) Layers by XPS. *Surf. Sci. Spectra* **2011**, *18* (1), 102–109. https://doi.org/10.1116/11.20061003.

(29) Lützenkirchen-Hecht, D.; Strehblow, H.-H. Anodic Silver (II) Oxides Investigated by Combined Electrochemistry, Ex Situ XPS and in Situ X-Ray Absorption Spectroscopy. *Surface and Interface Analysis* **2009**, *41* (10), 820–829. https://doi.org/10.1002/sia.3106.

(30) Popov, K.; Lajunen, L. H. J.; Popov, A.; Rönkkömäki, H.; Hannu-Kuure, M.; Vendilo, A. Li, Na , K and Cs NMR Comparative Equilibrium Study of Alkali Metal Cation Hydroxide Complexes in Aqueous Solutions. First Numerical Value for CsOH Formation. *Inorganic Chemistry Communications* **2002**, *5* (3), 223–225. https://doi.org/10.1016/S1387-7003(02)00335-0.

(31) Ergashovich, Y. K.; Abdukhalilovich, arymsakov A.; Sharaphovna, R. S. Bactericidal Hydrogel Based on Sodium-Carboxymethylcellulose Contained Silver Nanoparticles: Obtaining and Properties. *OJPChem* **2018**, *08* (04), 57–69. https://doi.org/10.4236/ojpchem.2018.84006.

(32) Xue, Gi.; Dai, Quinpin.; Jiang, Shuangen. Chemical Reactions of Imidazole with Metallic Silver Studied by the Use of SERS and XPS Techniques. *J. Am. Chem. Soc.* **1988**, *110* (8), 2393–2395. https://doi.org/10.1021/ja00216a009.

(33) Klotz, D. Negative Capacitance or Inductive Loop? – A General Assessment of a Common Low Frequency Impedance Feature. *Electrochemistry Communications* **2019**, *98*, 58–62. https://doi.org/10.1016/j.elecom.2018.11.017.